

MASTER THESIS

# AERODYNAMIC INTERACTION BETWEEN OVERLAPPING PROPELLERS

A NUMERICAL AND EXPERIMENTAL STUDY

MASTER'S DEGREE IN AEROSPACE ENGINEERING



INTERNAL SUPERVISOR:

PROF. LAROCCA, FRANCESCO

*DIMEAS, Politecnico di Torino*

CANDIDATE:

USAI DANIELE

*Politecnico di Torino*

EXTERNAL SUPERVISORS:

PROF. DR. IR. L.L.M. VELDHUIS

*FPP, Technische Universiteit Delft*

---

17 JULY 2019



# ACKNOWLEDGEMENTS

This is it. I am now writing my final contribute to this thesis work, and as I am doing it I could not feel more grateful to everyone who made this possible.

Foremost, I want to truly thank my supervisor Prof. Larocca, who has placed his trust in me and made it possible to reach this goal.

The six months spent at TU Delft have been one of the best periods in my entire academic career. From the long hours spent in the Open Jet Facility to the laughs shared in the faculty canteen, it has been a wonderful journey and experience. I feel I have to express my gratitude and appreciation to several people who helped me during my work there.

First of all, I would like to thank my supervisor at TU Delft, Prof. Leo. I will ever be truly grateful for this opportunity. Your guidance and impressive experience shaped the foundation of this work and thanks to your fundamental supervision I have been able to solve any doubts or uncertainties about the correct path to follow.

A special thanks goes to Tom. I am grateful for the amount of time you have dedicated to help me, as you were always ready to give me insightful advices. From you I learned how to focus on the important aspects of a scientific quest, how to see things from different perspectives and how to react professionally whenever something goes wrong.

I would like to thank Tomas for his fundamental presence and help during the experimental campaign, as well as for all the insights about the numerical approach. Also, I owe a big thank to Nando for his helpful contribution during the experiments.

A special thanks to all the guys from room 6.01, you made me feel at home and your company really helped me overcome any difficulties during my stay.

My warmest thanks goes to my family; your never ending love, trust, kind words and support have always been the real motivation behind everything I have achieved.

To all my friends from my beloved island, to all the people whom I shared my path with, to everyone who enlightened me with their words and actions, to a person who changed my life, my heartfelt thanks.

Ride the spiral.

*Daniele Usai  
Turin, July 2019*



# SUMMARY

The demand of a new sustainable on-demand urban air transportation system is pushing the aerospace industry towards new groundbreaking concepts of electrical VTOL vehicles. Various challenges are related to such type of vehicle, from avionic and flight controls to the determination of efficient propulsive systems and their integration in the airframe. In particular, in many of these concepts a large number of propellers is present in configurations where interactions within each other might represent a cause of concerns. This thesis work aims to understand the fundamental effects of the interaction between propellers in overlapping configuration, which is when the two propellers are placed one after another. In particular, the main focus is directed towards the effects of the front propeller slipstream on the rear propeller performance.

For this purpose, a numerical model was developed, based upon an existing blade element theory code, properly modified with a slipstream model and a method through which the blade response to the non uniform inflow. An experimental campaign took place in Delft University of Technology's Open Jet Facility, using scale models of the F29 Fokker propeller. Measurements of the isolated propeller, of the front propeller slipstream total pressure distribution and of the rear propeller's performance were taken and compared with the results obtained through the numerical evaluation. A sensitivity study of the interaction was performed with respect to several different parameters, such as lateral separation, axial distance between the propellers and their rotational speeds.

Several conclusions can be drawn from the results of this work. Since a broad range of configurations were studied, it was possible to understand how each parameter influenced the interaction. It was found that a propeller working in a non uniform inflow, when ingesting the wake of another propeller, can lose up to 80% of its thrust when fully overlapped. The main factor that influences the magnitude of the experienced losses is the lateral separation, since it determines the area of overlap. The interaction has a strong impact on the behaviour of the propeller, and the fundamental reason behind this is that, due to the increased axial velocity of the slipstream, the part of the blade affected by it develops less thrust and torque components. Once established that the propeller experiences losses due to the interaction, a desired requirement would be to know how much power is necessary to keep the same thrust as it was before the interaction. It was found that, for a high rate of overlap, it is necessary to provide an increase in power equal to 25% of the corresponding power from the isolated configuration. The comparison between numerical and experimental results shown a good agreement, and it was possible to predict the effect on thrust and power of the wake impingement on the rear propeller. It should be noted that the code is both fast and adaptable, therefore every tested configuration has a correspondent solution performed inside the program.

All of these results allow us to conclude that, when designing such vehicles, the integration of propellers is an aspect that must be studied in depth, focusing the attention especially on considering the decreased performance of a propeller reached by another propeller's wake. A proper flight control system for these vehicles should be able to handle the effects of the interaction, since a decrease in the thrust of one of the propellers could cause static instabilities of the vehicle itself or to higher energy consumption. We can consider this work as an early step towards the understanding of interaction between propellers in such configurations. More advanced computational approaches, possibly matched by measurements that involves flow visualization or noise measurements, should be the focus of follow-up researches on the study of aerodynamic interaction between propellers.



# SOMMARIO

La richiesta di un nuovo e sostenibile sistema di trasporto aereo urbano on-demand ha mosso l'industria aerospaziale verso nuovi e innovativi prototipi di velivoli elettrici VTOL. Diverse sono le sfide relative a queste tipologie di velivolo, dall'avionica e il controllo di volo fino alla definizione di sistemi di propulsione efficienti e la loro integrazione nel corpo del velivolo. In particolare, in molti di questi concepts è presente un alto numero di eliche in configurazioni dove l'interazione aerodinamica, tra le eliche stesse, è necessario che venga trattata con attenzione. Questo lavoro di tesi è rivolto alla conoscenza degli effetti fondamentali dell'interazione tra eliche in configurazioni overlap, cioè quando le due eliche sono poste una dietro l'altra ad una certa distanza. In particolare, l'attenzione è principalmente rivolta agli effetti che la scia dovuta alla elica anteriore ha sull'elica posteriore.

A questo proposito, un modello numerico è stato sviluppato, partendo da un esistente codice basato sulla blade element theory, opportunamente modificato con l'aggiunta di un modello di scia e un metodo tale da permettere lo studio della risposta della pala a causa del flusso non uniforme. Una campagna sperimentale è stata condotta nel Delft University of Technology's Open Jet Facility, utilizzando modelli basati sull'elica F29 della Fokker. Sono state effettuate misure dell'elica in condizione isolata, misure della pressione totale presente nella scia dell'elica anteriore e delle prestazioni dell'elica posteriore, poi confrontate con i risultati ottenuti tramite la procedura numerica. È stato portato avanti uno studio sulla sensibilità dell'interazione rispetto a diversi parametri, quali la separazione fra le eliche, la loro distanza assiale e la loro velocità di rotazione.

Diverse conclusioni possono essere tratte dai risultati di questo lavoro. Poiché è stata studiata un'ampia gamma di configurazioni, è stato possibile capire come ogni parametro preso in considerazione influenzasse l'interazione. È emerso che un'elica operante in un flusso non uniforme, nel caso di ingestione di scia di un'altra elica, può arrivare a perdere fino all'80% della spinta, quando totalmente sovrapposte. Il principale fattore che influenza la gravità delle perdite sopportate è la separazione laterale fra le eliche, in quanto determina l'area di sovrapposizione. L'interazione ha un forte impatto nel funzionamento dell'elica, e la spiegazione fondamentale dietro ciò è che, a causa della componente di velocità assiale presente nella scia, la parte dell'elica interessata sviluppa componenti di spinta e coppia minori. Una volta stabilita l'entità delle perdite prestazionali dell'elica a causa dell'interazione, un requisito desiderato è la conoscenza della potenza necessaria a sopprimere alle perdite e mantenere invariata la spinta. Per un alto grado di sovrapposizione, si è trovato che è necessario fornire incrementi di potenza pari a circa il 25% della potenza corrispondente al caso isolato. I risultati numerici si sono dimostrati essere molto simili a quelli ottenuti tramite le misurazioni sperimentali, e grazie alla velocità e adattabilità del codice utilizzato, è stato possibile avere una soluzione numerica corrispondente ad ogni configurazione testata.

La totalità dei risultati ottenuti ci permette di concludere che, al momento di progettare tali velivoli, è necessario concentrare l'attenzione particolarmente sulle configurazioni, che merita uno studio approfondito, prestando soprattutto attenzioni alla diminuzione delle prestazioni di un'elica raggiunta dalla scia di un'altra elica. Il sistema di controllo del volo per questi velivoli deve essere progettato di modo tale da gestire gli effetti dell'interazione, in quanto la perdita di spinta di una delle eliche può portare ad instabilità statiche dell'intero velivolo o a più alti consumi energetici. Tale lavoro può essere considerato come un passo preliminare verso la comprensione dell'interazione tra eliche in tali configurazioni. Ulteriori approcci computazionali più avanzati, accompagnati da misurazioni riguardanti la visualizzazione del flusso in prossimità della zona di interazione o misurazioni del rumore, sono da considerarsi i principali obiettivi di ulteriori ricerche riguardanti lo studio della interazione aerodinamica fra eliche.



# TABLE OF CONTENTS

<b>Acknowledgements</b>	<b>iii</b>
<b>Summary</b>	<b>v</b>
<b>Sommario</b>	<b>vii</b>
<b>Nomenclature</b>	<b>xiii</b>
<b>I Background</b>	<b>1</b>
<b>1 Introduction</b>	<b>3</b>
1.1 Demands of electronic VTOL vehicles. . . . .	3
1.2 Rotor-Rotor Interference Challenges in eVTOL Vehicles. . . . .	5
1.3 Research Objectives. . . . .	6
1.4 Thesis Outline . . . . .	7
<b>2 Theoretical background on propellers</b>	<b>9</b>
2.1 Isolated propeller theory . . . . .	9
2.1.1 Momentum theory. . . . .	9
2.1.2 Blade Element Momentum Theory (BEMT) . . . . .	10
2.2 Propeller Slipstream properties . . . . .	11
2.2.1 Induced velocity profile . . . . .	11
2.2.2 Total and static pressure distribution . . . . .	12
2.2.3 Contraction . . . . .	13
2.3 Propeller in non-uniform inflow . . . . .	13
2.3.1 Propeller in angle of attack. . . . .	13
2.3.2 Rotor - Rotor interference . . . . .	14
<b>II Methodology</b>	<b>17</b>
<b>3 Numerical Setup</b>	<b>19</b>
3.1 Isolated propeller setup . . . . .	20
3.1.1 2D aerodynamic analysis . . . . .	20
3.1.2 Evaluation of sectional angle of attack . . . . .	22
3.1.3 Evaluation of sectional thrust and torque . . . . .	23
3.1.4 Evaluation of induced velocities . . . . .	23
3.1.5 Evaluation of total forces and performance of the propeller . . . . .	25
3.1.6 Validation of the program . . . . .	25
3.2 Slipstream model . . . . .	28
3.2.1 Input from the front propeller solution . . . . .	28
3.2.2 Evaluation of the Axial Induced Velocity . . . . .	29
3.2.3 Evaluation of the Tangential Induced Velocity . . . . .	30
3.2.4 Defining the input for the rear propeller . . . . .	30
3.3 Rear propeller setup . . . . .	32
3.3.1 Quasi steady Analysis . . . . .	32
3.3.2 Unsteady analysis . . . . .	33
<b>4 Experimental Setup</b>	<b>37</b>
4.1 Test Campaign Overview . . . . .	37
4.2 Wind Tunnel Facility . . . . .	38
4.3 Wind Tunnel Models . . . . .	38
4.4 Measurement techniques . . . . .	41
4.4.1 Propeller Performance Measurements . . . . .	41
4.4.2 Total Pressure Measurements . . . . .	41

4.5	Test Conditions and Parameters. . . . .	42
<b>III</b>	<b>Results</b>	<b>45</b>
<b>5</b>	<b>Numerical Results</b>	<b>47</b>
5.1	Analysis Overview. . . . .	47
5.2	Isolated Propeller Performance . . . . .	47
5.3	Slipstream model results . . . . .	49
5.4	Rear Propeller Performance: Interaction Effects. . . . .	50
5.4.1	Propeller inflow . . . . .	50
5.4.2	Comparison between Quasi Steady and Unsteady Results . . . . .	53
5.4.3	Effects of the interaction on the performances. . . . .	55
5.4.4	Effect of the Interaction on the Rear Propeller Thrust . . . . .	57
5.4.5	Increased power requirement to recover the loss of thrust . . . . .	58
<b>6</b>	<b>Experimental results</b>	<b>61</b>
6.1	Measurement Overview. . . . .	61
6.2	Isolated Propeller Performance . . . . .	61
6.3	Front Propeller Slipstream Measurements . . . . .	63
6.4	Rear Propeller Performance: Interaction Effects. . . . .	66
6.4.1	Effects of the interaction on the performance . . . . .	66
6.4.2	Effect of the Interaction on the Rear Propeller Thrust . . . . .	68
6.4.3	Increased power requirement to recover the loss of thrust . . . . .	69
<b>7</b>	<b>Comparison and Discussion of Numerical and Experimental Results</b>	<b>71</b>
7.1	Isolated Propeller Performance . . . . .	71
7.2	Front Propeller Slipstream . . . . .	72
7.3	Rear Propeller Performance: Interaction Effects. . . . .	73
7.3.1	Effect of the Interaction on the Rear Propeller Thrust . . . . .	73
7.3.2	Increased Power Requirement to Recover the Loss of Thrust. . . . .	77
<b>8</b>	<b>Conclusions and Recommendations</b>	<b>79</b>
8.1	Conclusions. . . . .	79
8.2	Recommendations for future works. . . . .	81
<b>IV</b>	<b>Appendices</b>	<b>83</b>
<b>A</b>	<b>Influence of the critical amplification factor</b>	<b>85</b>
<b>B</b>	<b>Sensor Calibration Matrix</b>	<b>87</b>
<b>C</b>	<b>Additional Numerical Results</b>	<b>89</b>
	<b>Bibliography</b>	<b>91</b>

# NOMENCLATURE

## LIST OF SYMBOLS - LATIN

Symbol	Description	Unit
$a$	Adimensional axial induced factor, $a = v_a / V_\infty$	-
	Speed of sound	m/s
$A$	Propeller area	m <sup>2</sup>
$a_{cor}$	Coriolis acceleration	m/s <sup>2</sup>
$a_{cen}$	Centrifugal acceleration	m/s <sup>2</sup>
$a_t$	Non-dimensional tangential induced factor, $a_t = v_t / \Omega r$	-
$a'_t$	Non-dimensional tangential induced factor, $a'_t = v_t / V_\infty$	-
$B$	Number of blades	-
$c$	Blade section chord	m
$c_d$	Drag coefficient	-
$c_l$	Lift coefficient	-
$C_p$	Pressure coefficient	-
$C_P$	Power coefficient, $C_P = P / \rho n^3 D^5$	-
$C_T$	Thrust coefficient, $C_T = T / \rho n^2 D^4$	-
$\Delta C_T$	Thrust coefficient difference due to the interaction	-
$D$	Drag force	N
	Propeller diameter	m
$d_y$	Adimensional lateral separation position	-
$d_x$	Adimensional axial separation position	-
$f$	Prandtl loss factor exponent	-
	Frequency	Hz
$F$	Prandtl loss factor	-
$f_0$	Non-dimensional freestream velocity	-
$J$	Advance ratio, $J = V_\infty / nD$	-
$J_n$	$n^{th}$ order Bessel function of the first kind	-
$k$	Harmonic order	-
	Index	-
$K_n$	$n^{th}$ order Bessel function of the second kind	-
$L$	Lift force	N
$M_\infty$	Mach number	-
$n$	Rotational velocity	rev/s
$N$	Critical amplification factor	-
$p$	Pressure	m
$P$	Power	W

Continued on next page

Continued from previous page

Symbol	Description	Unit
$\Delta P$	Power requirement to keep equal thrust after the interaction	-
$P_{ind}$	Induced power, $P_{ind} = v \cdot T$	W
$p_t$	Total pressure	Pa
$q$	Dynamic pressure, $q = \frac{1}{2}\rho V^2$	Pa
$Q$	Torque	Nm
$r$	Radial coordinate	m
$R$	Propeller radius	m
$Re$	Reynolds number	-
$rps$	Propeller rps	rev/sec
$S$	Sears function	-
$T$	Thrust	N
$T_C$	Thrust Coefficient, $T_C = T/\rho V_\infty^2 D^2$	-
$v$	Induced velocity component	m/s
$V$	Velocity	m/s
$W$	Effective velocity on the blade section	m/s
$x$	x-coordinate	m
$y$	y-coordinate	m
$z$	z-coordinate	m

## LIST OF SYMBOLS - GREEK

Symbol	Description	Unit
$\alpha$	Angle of attack	deg
$\beta$	Blade pitch angle	deg
$\gamma$	Vorticity, $\gamma = d\Gamma_B/dy$	1/s
$\Gamma_B$	Bound circulation distribution	m <sup>2</sup> /s
$\zeta$	Non-dimensional axial coordinate	-
$\eta$	Non-dimensional radial coordinate	-
	Propeller efficiency, $\eta = VT/P$	-
$\Theta_{sw}$	Swirl angle	deg
$\kappa_{ov}$	Overlapping factor	-
$\mu$	Dynamic viscosity	Pl
$\rho$	Density	kg/dm <sup>3</sup>
$\sigma$	Reduced frequency, $\sigma = k\Omega c/2W$	-
$\phi$	Local incidence angle	deg
$\Psi$	Polar angle	deg
$\Omega$	Rotational velocity, $\Omega = 2\pi n$	rad/s

## ABBREVIATION

Symbol	Description
<i>BEMT</i>	Blade Element Momentum Theory
<i>CFD</i>	Computational Fluid Dynamics
<i>ECN</i>	Energy Research Center of Netherlands
<i>NLR</i>	Netherland Aerospace Center
<i>PIV</i>	Particle Image Velocimetry
<i>rps</i>	Revolution per second
<i>VTOL</i>	Vertical Take Off (and) Landing

**SUB- AND SUPERSCRIPTS**

<b>Symbol</b>	<b>Description</b>
$\infty$	Freestream
<i>a</i>	Axial
<i>eff</i>	Effective
<i>eq</i>	Equal
<i>f</i>	Front propeller
<i>hub</i>	Hub of the blade
<i>inst</i>	Installed
<i>iso</i>	Isolated
<i>QS</i>	Quasi steady
<i>s</i>	Slipstream
	Static
<i>r</i>	Rear propeller
<i>t</i>	Tangential
	Total
<i>tip</i>	Tip of the blade
<i>UNS</i>	Unsteady



# I

## BACKGROUND



# 1

## INTRODUCTION

### 1.1. DEMANDS OF ELECTRONIC VTOL VEHICLES

The desire to fly has always been present in humanity, but the first individual to approach the manner "scientifically" was Leonardo Da Vinci. His flying machine, of which we can see the design in Figure 1.1, is basically a helical air screw, and it was conceived to lift off the ground vertically, like modern helicopters do.

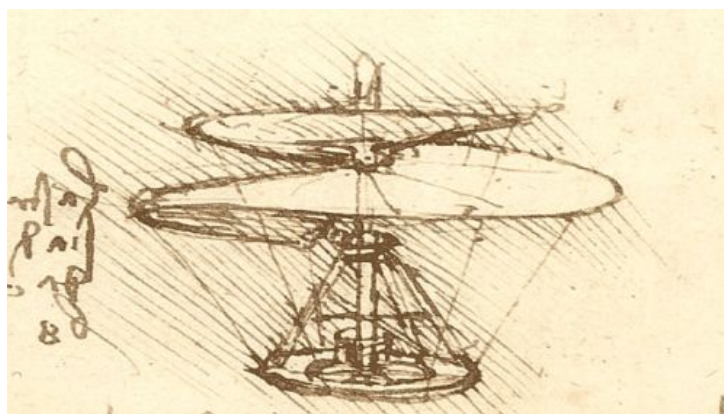


Figure 1.1: Original drawing of the Leonardo da Vinci flying machine

However, the practical solution proposed by Wright brothers of sustainable flight, based on the concept of a fixed wing that generates lift, became the first and most widespread way to achieve human flight. During the second half of the previous century helicopters proved to be an essential machine for numerous works and application. The main limits of the helicopters are related to the extremely short range and speed achievable. So, the search for an aircraft type with Vertical Take Off and Landing (VTOL) has always been present in the aerospace research, since it could fill the gap between a direct lift aircraft and helicopters, thanks to the high vertical lift efficiency and relatively low disc loading, as it's shown in Figure 1.2.

VTOL field of application is potentially very broad, even though its biggest and well known example is the Bell Boeing V-22 Osprey, a tiltrotor military aircraft. However recently, thanks to the rise of small unmanned vehicles, a renewed interest in urban air transportation has grown, and electric VTOL could really represent a groundbreaking solution to this demand. The problem of wasted time during commuting between work and home in big cities is becoming more and more relevant. On average, in 2015 commuters in Los Angeles and Sidney spent seven whole working weeks each year commuting, two of which are wasted stuck in gridlock. In megacities like Mumbai, the average daily commuting time is more than 90 minutes [1]. This means less time working or with families, but also more money spent on fuel and increased level of stress.

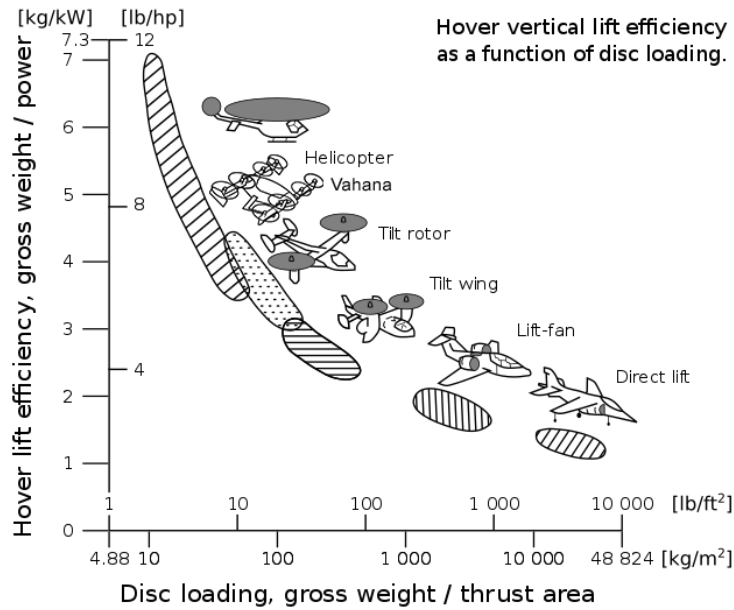


Figure 1.2: Power loading vs. disc loading for different VTOL vehicle types. (From [2], original at [3])

Uber Elevate project and the Clean Sky research programme funded by the EU’s Horizon 2020 programs both contributed in rising and pushing the industry and the research toward disruptive concepts in the aerospace industry. Numerous companies have joined in the recent years their mission, developing a wide range of different types of eVTOL vehicles, along with other technologies like vehicle autonomy or distributed electric propulsion. The idea of distributed electric propulsion is to replace the single complex rotor system with multiple simpler thrusters, in most cases propeller driven by electric motors, in order to improve emissions, safety and noise [4]. Many requirements define the eVTOL model proposed by Uber, such as high specific energy batteries (around 400 Wh/kg) or 500 kW of power for short term take-off [1]; thanks to the dramatic development of electric motors and batteries, it is possible to obtain very high specific powers and energy, as shown in Figures 1.3 and 1.4.

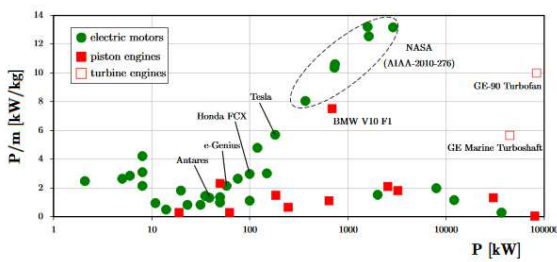


Figure 1.3: Specific power density of current piston engines (squares) and electric motors (circles) [5]

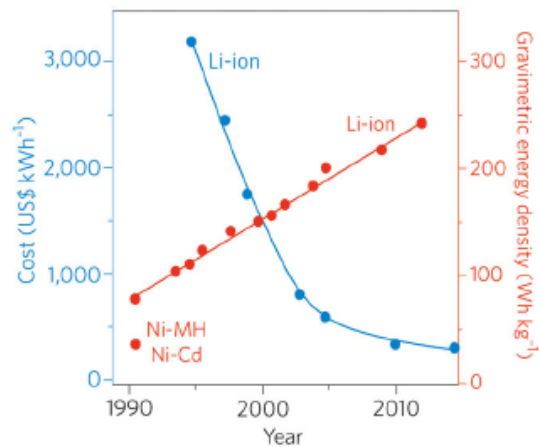


Figure 1.4: Yearly development of cost and energy density of batteries [6]

The most recent unveiled concept is the Nexus by the American-based company Bell. The Bell Nexus was announced on April 25, 2017 at the Uber Elevate Summit and a cabin experience was presented at the Consumer Technology Association’s CES 2018; a full mock up concept of the aircraft was shown at the 2019 edition of Consumer Technology Association’s CES [7] and is depicted in figure 1.5a. This hybrid electric aircraft has six propellers, each of them located inside a tilting duct, three for each side with the central pair of propellers attached to a 2.4 m wing. Two different versions of the Nexus are currently in developments, one that holds one passenger and one pilot and one that holds six passengers.

In early 2016, A<sup>3</sup> (pronounced "A-cubed") - an advanced project of Airbus Group in Silicon Valley - began the development of Project Vahana, an autonomous vehicle featuring two tilting wing, with four propellers attached to each wings. A<sup>3</sup> Vahana's first test flight occurred in January 31st, 2018, and since then, 50 full-scale test flights have been flown, for a total of 5 flight hours [8]; in figure 1.5b the vehicle is shown in the hovering condition. Key features of the Project Vahana regards mainly safety, scalability and affordability. They aim to save a total of 78% of the costs if compared to a conventional helicopter. Moreover, by implementing a full-autonomous piloting system, A<sup>3</sup> believes that an improvement in safety and situational awareness will follow [4]. Two versions of the Vahana have been planned, for one and two passengers.

At last, it is worth mentioning the vehicle proposed by the Santa Cruz company Joby Aviation (possible name, according to FAA registration records is S4). The company takes a low profile on promoting this concept, and at the present moment no technical details have been released. The S4 has a large aspect ratio wing with inverted delta, equipped with 8 tilt-rotors, and a v-tail with 4 tilt-rotors mounted on it. It is known that the first flight occurred on February 1st, 2018 where the prototype took off and completed a 15 minute, 15 mile loop and performed a safe landing [9]. A rendering of the S4 is presented in Figure 1.5c



Figure 1.5: Most relevant eVTOL concepts mentioned in this work. From top left: Bell Nexus, A<sup>3</sup> Vahana, Joby Aviation.

## 1.2. ROTOR-ROTOR INTERFERENCE CHALLENGES IN EVTOL VEHICLES

Referring to the vehicle configuration just presented, it is possible to appreciate the high number of propellers driven by electric motors. Many challenges are related to these configurations, for example the assessment of an accurate autonomous controller system, or the integration between different avionic system for such a complicate design. Moreover, it is possible to notice how the propellers are close to each other, and overlap between them is present. This means that it is possible to predict that different degrees of interaction happen between propellers. In particular, it is possible to delineate two main types of interaction, outlined in Figure 1.6.

Interactions could happen when two propeller are close in a side by side configuration, especially if between the thrust direction and flight direction a strong angle is present. The two slipstreams might interacts, therefore influencing the load distribution of the propellers.

This thesis work, however, is focused on the second case of interaction, where propellers are in a overlapping configuration. In this case, the slipstream of the front propeller reaches the rear propeller disc. It is possible to appreciate, looking again at Figure 1.5, the variety of distances between the propeller disc, and the degree of overlap. We can expect that the both propeller are mutually influenced in this configuration, even though the rear one, probably, is much more affected. In a propeller's slipstream, depending on the load level of the pro-

propeller, an axial and tangential velocities are present. When a propeller operates in such type of flow, its blades are subject to unsteady inflow, therefore generating unsteady load. We can already expect that this behaviour will have some strong impact on the overall, time averaged propeller performance.

The majority of the studies regarding interaction between propellers or rotors comes from the research about coaxial rotors in helicopters, while the available data and researches about partial overlapping are very limited and case-specific. This is justified by the fact that, until now, an aircraft configuration for which such a phenomenon happens has never been really common. Moreover, apart from experiments, the simulation of such interaction is still computationally expensive. However, we can find already from the '50s some interest in this topic, especially for propellers mounted on a wing, with some authors that underline an increase in thrust of the rear propeller due to the overlap [10] in a configuration where both propeller discs are close to each other. Another study [11] concerning rotors overlapping in tandem configuration for helicopters, shows an increased  $\kappa_{ind}^1$  for overlaps up to  $d/D = 0.6$  in hover flight. This increased induced power of the tandem system is conceivably due to the increased inflow velocity seen by the rear rotor.

Attention towards rotors interaction due to overlap has recently seen a new rise thanks to investigation towards small unmanned drones equipped with a quadrotor system. Ref. [12] shows a dramatic loss in thrust has been found for an overlap of a propeller radius, along with a much smaller loss in drag. In ref. [13] shows interesting and unexpected results, partially confirming the results obtained in ref. [11]. The most extensive research about the argument is presented in ref. [14], where both rotors performance involved in the interaction are studied for a wide range of overlap.

However, at the present day, it is not possible to find a research where such interaction is extensively studied. Each of the aforementioned researches presents results where the axial separation between propellers disc is quite small, therefore not useful to understand what the interaction's effects could be in cases where the axial distances between the propellers is more than one propeller radius, for example. Moreover in general the main focus of the cited references is to understand the effects in terms of gain or loss of efficiency of the whole system made by two rotors.

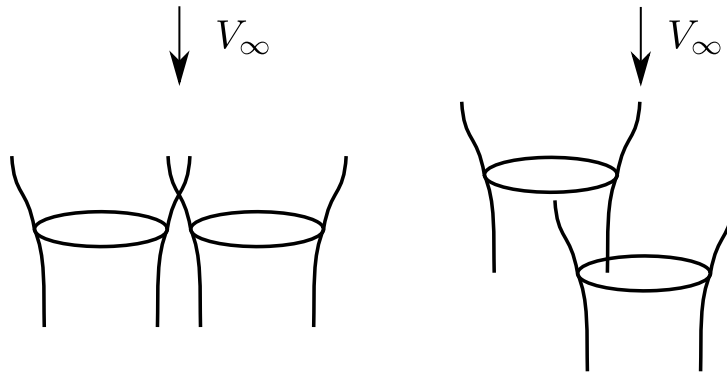


Figure 1.6: Propellers configurations present in eVTOL vehicles: side by side or one after another.

### 1.3. RESEARCH OBJECTIVES

The main topic of this thesis is focused on the understanding of the fundamental aerodynamic phenomena that characterize the interaction between two propellers in overlapping configuration. In particular, through numerical and experimental investigation, the main research aim can be defined as such:

*The aim of this research project is to study from a numerical and experimental approach the effect on the performance of an interaction between rotors, when they are in an overlapping configuration.*

It should be noted that, due to limitation both from numerical resources and experimental setup, the results presented are mainly focused on the effect of the interaction relative to the propeller downstream the front one.

In order to fulfill the research aim, it is required to satisfy the following research objectives :

- To understand and study what are the main parameters and operating conditions that influence the interaction and what are their effect on the performance

---

<sup>1</sup> $\kappa_{ind} = \frac{(P_i)_{tandem}}{2(P_i)_{single}}$ , see [11]

- the influence of the lateral and axial distance between the propellers on the interaction
- the influence of the thrust levels of both propellers on the interaction

The experimental campaign planning was structured so that the largest range of possible configuration was studied.

- To develop a numerical tool capable to predict the effects of the interaction on the rear propeller. This tool needs to be reliable and fast, the desired outcome from its development is to predict the entire range of configurations tested during the experiments.

## 1.4. THESIS OUTLINE

The body of this thesis work consists in three main Parts and a total of eight Chapters, organized as in Figure 1.7. Part I consists of this Chapter which serves as a general introduction to the propellers interaction issues present in eVTOL future concepts. In Chapter 2 a theoretical background is discussed, presenting the main theories used to study propellers' behaviour and performance.

The second Part presents the methodology used in this work. The numerical evaluation performed in order to predict the effects of the interaction is treated in Chapter 3, and subsequently Chapter 4 deals with the setup and methodology adopted in the experimental test campaign.

Finally, in Part III the results are discussed, and following the structure of the previous Part, in Chapter 5 the numerical evaluation are presented, while the results obtained through the experiments are proposed in Chapter 6. After the separate discussion of numerical and experimental results, in Chapter 7 they are compared. At last, in Chapter 8 the conclusions drawn from this work are stated, along with recommendations for future research.

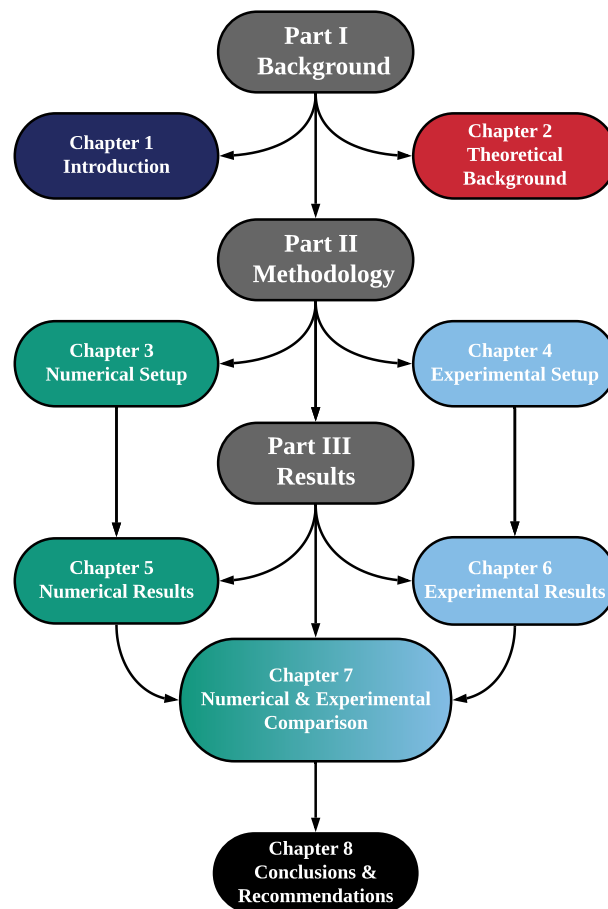


Figure 1.7: Thesis outline



# 2

## THEORETICAL BACKGROUND ON PROPELLERS

This chapter presents an overview of the theoretical background on which the present work is based. The main methods and theories used to study propellers are presented in Section 2.1, a description of the propeller slipstream in Section 2.2, and finally in Section 2.3 a general framework on propeller in non uniform inflow is presented.

### 2.1. ISOLATED PROPELLER THEORY

In this Section the two main theories used to describe propellers are presented. In Subsection 2.1.1 the basis of the momentum theory are shown, while in 2.1.2 the Blade Element Momentum Theory is discussed in its main aspects.

#### 2.1.1. MOMENTUM THEORY

The main function of a propeller is to convert mechanical energy, provided by a motor, into a force, called thrust. In the momentum theory [15] the propeller is an infinitely thin disc and the thrust is seen as a change in the momentum of the flow, generated by a low static pressure distribution in front of the propeller and a higher pressure right behind the propeller. The decrease in pressure accelerates the flow through the control volume defined as a streamtube, outside of which the flow is at a constant stagnation pressure. The total pressure at the disc location sees a jump of its value and remains constant inside the downstream part of the streamtube, that, due to the acceleration of the flow, contracts. The induced axial velocity  $v_a$  at the propeller disc is half its value in the far field downstream, due to the equalization of the static pressure inside and outside the streamtube [16]. The axial momentum theory neglects the swirl component imparted by the propeller's rotation, but it is useful to get the thrust generated by the propeller. For future reference, in Figure 2.1 are shown also the non dimensional radial coordinate  $\eta = r/R_p$ , the non dimensional axial coordinate  $\zeta = x/R_p$  and the polar angle  $\Psi$ . The effects on the flow quantities can be seen in Figure 2.2.

The thrust generated by the propeller, following the general momentum theory is given by

$$T = 2A_p \rho (V_\infty + v_a) v_a \quad (2.1)$$

The power generated by the propeller  $P$  must be equal to the increase of the kinetic energy inside the slipstream, so that:

$$P = 2A_p \rho (V_\infty + v_a)^2 v_a \quad (2.2)$$

Along with the thrust, which is the force in the direction normal to the propeller disc, torque and normal forces are the other main components that acts on the propellers. It is often useful to consider non dimensional quantities to represent the thrust and power so that the comparison between different propellers, or within the same propeller's different configurations, is more appropriate.

$$C_T = \frac{T}{\rho n^2 D_p^4} \quad C_P = \frac{P}{\rho n^3 D_p^5} \quad (2.3)$$

With  $n$  the rotational speed of the propeller in rps and  $D_p$  the diameter of the propeller. In the literature there is some contradiction about how to represent the efficiency of the propeller, but the most common form is the one from Glauert [16].

$$\eta = V \frac{T}{P} \quad (2.4)$$

Generally, to understand the behaviour and the performance of a propeller, the adimensional quantities in Equation 2.3 and 2.4 are plotted versus the advance ratio  $J = \frac{V_\infty}{nD}$ , which is an adimensional factor that represent the load level of the propeller. A propeller operating at a low advance ratio is defined as highly loaded propeller, while it is a lightly loaded propeller for high values of  $J$ .

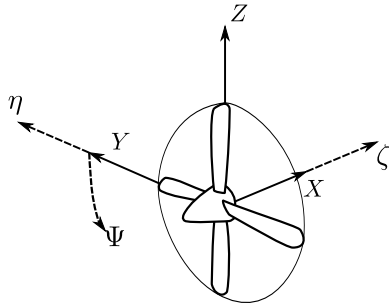


Figure 2.1: Propeller coordinate system

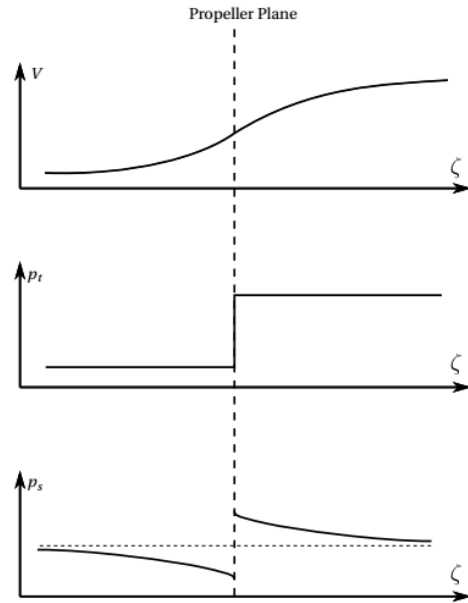


Figure 2.2: Distribution of the flow quantities in the momentum theory

### 2.1.2. BLADE ELEMENT MOMENTUM THEORY (BEMT)

The momentum theory bases the evaluation of the thrust and torque of the propeller by considering of the mean axial and rotational velocity in the slipstream. An attractive method that extends the momentum theory, initially developed by W. Froude and then established by S. Drzewiecki [17], is the blade element momentum theory.

This method is well known for its accuracy and relatively low computational cost, and due to its adaptability to different problems, is indeed the foundation of the numerical approach explored in this thesis; in this section only the main features and formulations will be presented.

Considering an element of a blade extending over a length  $dr$  of the radius at a distance  $r$  from the axis of rotation, the cross-section of this element has the shape of an airfoil section. It is important to notice that an assumption of the BEMT is that each individual blade element is independent and not influencing each other. As shown in Figure 2.3, in BEMT the aerodynamic force acting on the blade element can be estimated as the force on an airfoil, advancing through air at a velocity  $W$ , defined as:

$$W = V_\infty^2 + \Omega^2 r^2 \quad (2.5)$$

With  $\Omega r$  the rotational velocity and  $V$  the forward velocity. The local incidence of each element is:

$$\tan \phi = \frac{V}{\Omega r} \quad (2.6)$$

Propeller blades present are generally highly twisted, and we can associate to each element a local pitch angle  $\beta$ , therefore the local angle of attack  $\alpha$  is:

$$\alpha = \beta - \phi \quad (2.7)$$

The validity of the theory and therefore the actual solution of the propeller loading depends on the lift and drag characteristics of the airfoil (or airfoils) chosen for the blade element. Each element will experience a lift force

$dL$  perpendicular to the direction of motion and a drag force  $dD$  opposed to the motion, expressed as follows:

$$\begin{aligned} dL &= \frac{1}{2} \rho W^2 c c_l dr \\ dD &= \frac{1}{2} \rho W^2 c c_d dr \end{aligned} \quad (2.8)$$

With  $c$  the chord of the local airfoil. We can solve the thrust and the torque of the element, the former in the direction of the forward motion and the latter in the opposite direction of rotation:

$$\begin{aligned} dT &= dL \cos \phi - dD \sin \phi \\ dQ &= (dL \sin \phi + dD \cos \phi) r \end{aligned} \quad (2.9)$$

By substituting in , and considering the number of blades  $B$ :

$$\begin{aligned} \frac{dT}{dr} &= \frac{1}{2} B c \rho W^2 (c_l \cos \phi - c_d \sin \phi) \\ \frac{dQ}{dr} &= \frac{1}{2} B c r \rho W^2 (c_l \sin \phi + c_d \cos \phi) \end{aligned} \quad (2.10)$$

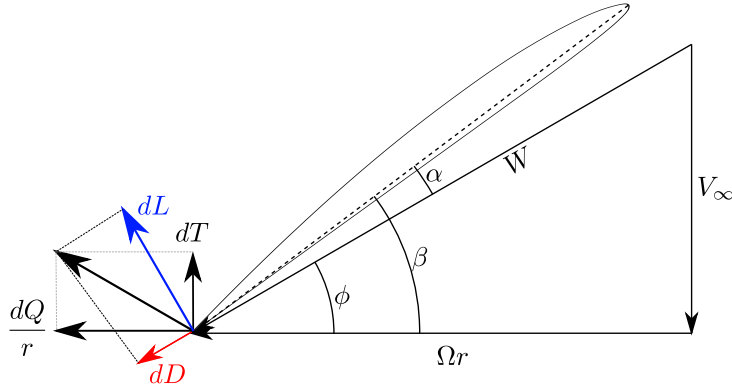


Figure 2.3: Blade element velocity and force diagram without induced velocities

## 2.2. PROPELLER SLIPSTREAM PROPERTIES

The slipstream generated by a propeller is a complex aerodynamic system. An intuitive representation of the propeller wake is described in the work of Veldhuis [18]. The blade is nothing more than a rotating wing that produces an helical vortex system, that produces self-induced velocities. These velocities cause a roll up of the vortex wakes, creating a slipstream tube with strong gradients of quantities both in radial and axial direction. Many aspect and quantities are involved, but the most relevant for this research are:

- Axial and tangential velocity profile
- Total and static pressure distribution
- Contraction

These quantities are further described in the following sections. More on the slipstream model used for the numerical work can be found in the "Methodology" part of this work.

### 2.2.1. INDUCED VELOCITY PROFILE

The lifting line theory by Prandtl [19] was adapted to propeller by Betz [20], and describes the potential flow around the blade in which the lifting surface is represented as a bound circulation distribution  $\Gamma_B$ . The variation of bound circulation generates free vortex lines  $\gamma$  with a magnitude equal to the variation of the bound circulation.

If we split this vortex system in an axial and tangential direction it is possible to understand better the effect on the induced field. The two components are:

$$\gamma_a = -\frac{d\Gamma_B}{dy} \cos \phi \quad (2.11)$$

$$\gamma_t = -\frac{d\Gamma_B}{dy} \sin\phi \quad (2.12)$$

This schematic picture can be seen in Figure 2.4 where the tangential vorticity is represented as vortex rings. The tangential vorticity  $\gamma_t$  induces the axial component of the velocity,  $v_a$ .

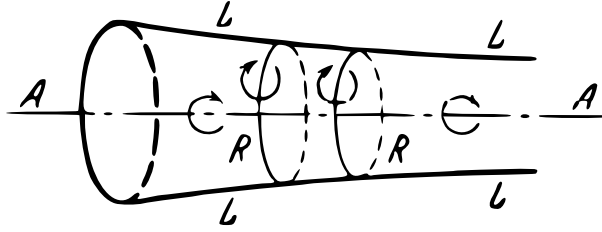


Figure 2.4: Streamtube model with vortex distribution (from [16])

So,  $v_a$  is directly related to the loading distribution in the blade spanwise direction, and usually the maximum value is around  $\frac{3}{4}R$  location and its value at the propeller disc is half that in the far wake. The tangential, or swirl, component of the induced velocity,  $v_t$ , is due to the bound circulation, and upstream, since there is no vorticity, its value is zero. So, the axial component of the vorticity,  $\gamma_a$ , contributes to the swirl velocity and cancels the upstream effect of the bound circulation, causing a value of tangential velocity at the propeller disc equal to half the one right behind the propeller. If we look at Figure 2.5 it is more clear how two different elemental bound vortices OR and OS induce an equal but opposite in sign axial components, while a different situation concerns the tangential components, whose direction is the same. Along the slipstream, the circulation must remain constant and equal to  $2\pi v_t r^2$ , with  $r$  the radius of the slipstream section. With the slipstream contracting to a smaller radius, by the conservation of the circulation, the tangential velocity in the slipstream increases slightly.

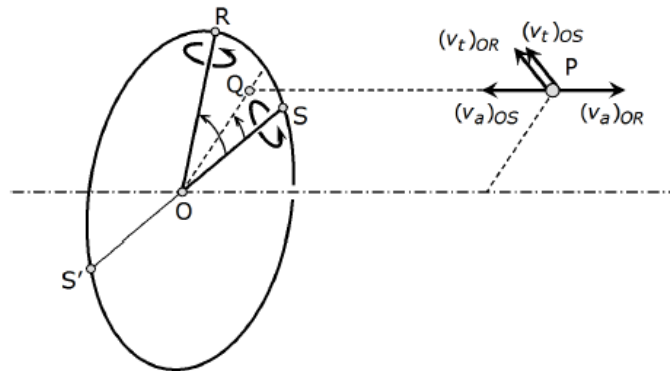


Figure 2.5: Axial and tangential velocities induced by the propeller blades (from [18])

### 2.2.2. TOTAL AND STATIC PRESSURE DISTRIBUTION

Looking at the static pressure development in front of the propeller, it decreases until a jump across the disc, and then decreases again until it reaches the constant pressure outside the slipstream. The total pressure jumps as well but to a constant value. At the location of the propeller disc there is a small difference between the total increase in static pressure and total pressure. This can be explained with the kinetic energy of the rotational motion imposed to the fluid by the torque of the propeller [18], and it can be demonstrated as follows. Considering the total pressure of the flow before and behind the propeller disc, assuming no contraction in the slipstream and the radial component of the velocity  $v_r = 0$ :

$$\begin{aligned} p_{t,\infty} &= p_\infty + \frac{1}{2}\rho V_\infty^2 = \\ &= p + \frac{1}{2}\rho((V_\infty + v_a)^2 + v_t^2) \end{aligned} \quad (2.13)$$

Let's now consider the total pressure far downstream, whose quantities are denoted with the index  $s$ :

$$\begin{aligned} p_{t,s} &= p + \Delta p + \frac{1}{2}\rho((V_\infty + v_{a_s})^2 + v_{t_s}^2) = \\ &= p_s + \frac{1}{2}\rho((V_\infty + v_{a_s})^2 + v_{t_s}^2) \end{aligned} \quad (2.14)$$

Therefore, the jump in total pressure is:

$$p_{t,s} - p_{t_\infty} = \Delta p + \frac{1}{2}\rho v_t^2 \quad (2.15)$$

The total pressure is increased, compared to the static pressure jump  $\Delta p$ , by a factor  $\frac{1}{2}\rho v_t^2$ , which is the kinetic energy imparted to the fluid by the torque of the propeller.

### 2.2.3. CONTRACTION

As the axial velocity in the slipstream increases, the slipstream radius has to decrease in order to preserve the mass flow. The contraction of the slipstream is quite small, but for heavy loaded propellers is not negligible and has to be taken into account for the interaction with the rear propeller.

Theodorsen proposed a complicated model for the slipstream that takes into account the radial component of the velocity, and in [21] is shown how the contraction in the ultimate wake is a few percent of the propeller diameter. However, an easier method can be adopted, and the ratio of contraction can be approximated as [18]:

$$\frac{R_s(x)}{R} = \sqrt{\frac{1+a}{1+a\left(1+\frac{x}{\sqrt{R^2+x^2}}\right)}} \quad (2.16)$$

With  $a = v_a/V_\infty$  is the adimensional axial factor.

## 2.3. PROPELLER IN NON-UNIFORM INFLOW

In practical applications, propellers are usually subject to non-uniform inflow, due to the presence of a body like a wing, or due to an angle of attack of the whole aircraft. The absence of an axis-symmetric inflow field generates an azimuthal variation of the local angle of attack experienced by the blade, thus inducing a non-symmetric load distribution over the propeller disc.

### 2.3.1. PROPELLER IN ANGLE OF ATTACK

Assuming an incidence angle  $\alpha$ , in fig 2.6 the propeller plane is shown, with  $\Psi$  the azimuthal angle. From 2.7 we can see that the horizontal component of the inflow velocity is constant for the whole propeller, while the one in the propeller plane,  $W \sin \alpha$  depends on  $\Psi$ . Between  $\Psi = 0^\circ$  and  $\Psi = 180^\circ$  the blade is downgoing and the in-plane speed is the sum of the rotational velocity and  $W \sin \alpha$  component, while from  $\Psi = 180^\circ$  to  $\Psi = 360^\circ$  the situation is the opposite. The two areas are called advancing and retreating blade area [22].

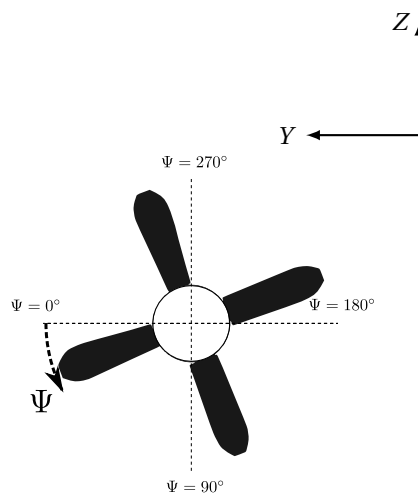


Figure 2.6: Azimuthal reference system

Due to the increased local angle of attack and speed in the advancing area, the overall lift and drag in this area will be greater than in the retreating area. If we project the resultant of the two forces on the propeller plane, we obtain a positive force.

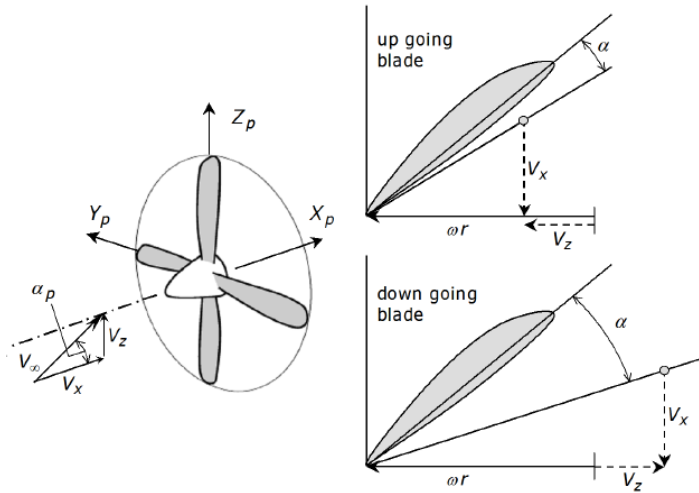


Figure 2.7: Blade angle of attack variation due to propeller pitch angle [18]

In the advancing area the blade generates more thrust, therefore the wake shed in this region is richer in circulation which induces greater velocity, compared to the retreating half. From numerical simulation of the propeller it's possible to see how the area of greater induced velocity is between  $\Psi = 330^\circ$  and  $\Psi = 150^\circ$  and as a result of this, the blade at the azimuthal position of  $\Psi = 180^\circ$  sees a greater angle of attack, compared to a blade passing at  $\Psi = 0^\circ$ . This non symmetrical condition generates an in-plane horizontal positive force.

### 2.3.2. ROTOR - ROTOR INTERFERENCE

In literature is difficult to find a fast and easy method supported by a well established theory that covers the problem of propellers interaction in the case of partial overlap at high axial distance. The flow tube developing downstream from the front propeller influences the rear rotor, and this is the fundamental physical concept of the rotor interference, assuming that the rear propeller has no influence upstream. Looking at the situation in 2.8 we can already see that the geometrical relative position between the two propellers is critical for the interference. In particular, assuming that both propellers have parallel axis of rotations, the axial separation  $d_x$  and lateral separation  $d_y$  are the most important parameters.

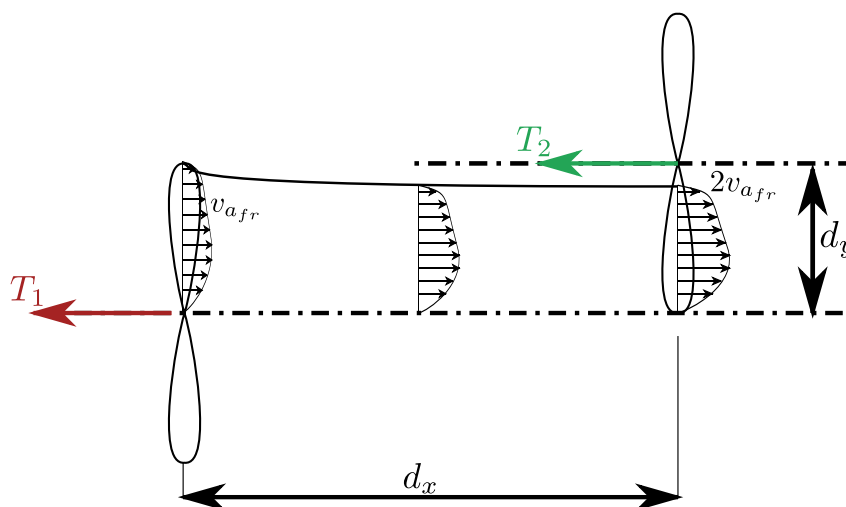


Figure 2.8: Geometrical schematization of the interaction between propellers in overlapping configuration

The rear propeller will see, partially, an increased axial velocity field due to the slipstream of the front propeller. This cause the blade to see a decreased local angle of attack therefore generating less aerodynamic forces compared to those in the region unaffected by the impingement. It is already possible to expect an increase in the loss of thrust with the decrease of the factor  $d_y$ , since the effect of the axial velocity are not related to the rotational velocity direction of the rear propeller. Moreover, the mean axial velocity of the slipstream grows with the thrust level of the front propeller.

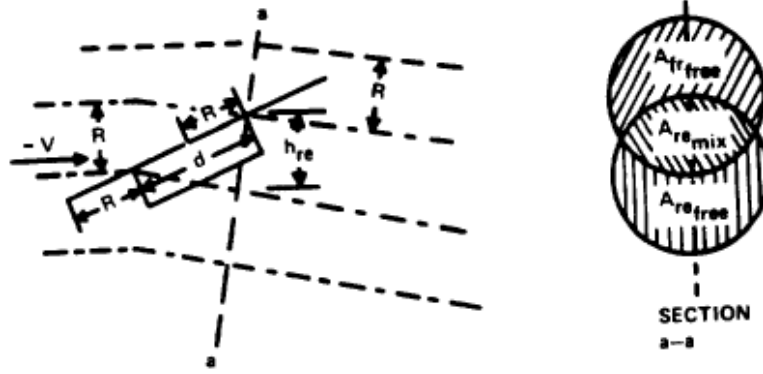


Figure 2.9: Streamtube mix of two rotors (from [23])

A low - level approach, based on momentum theory, was taken by Stepniewsky [23] for the case of rotors interactions in tandem configuration in helicopters as depicted in 2.9. The geometric position of the rear rotor with respect to the centerline of the streamtube affected by the front rotor is  $h_{re}$ , which can be seen as a resultant of the previous mentioned  $d_x$  and  $d_y$ . The induced power of the front rotor is:

$$P_{ind_{fr}} = v_{fr} T_{fr} \quad (2.17)$$

While the induced power of the rear one can be broken down into two components, one related to the undisturbed part:

$$P_{ind_{re_{free}}} = T_{re} v_{re} \left( \frac{A_{re_{free}}}{\pi R^2} \right) \quad (2.18)$$

and the part where the slipstream impinges the disc:

$$P_{ind_{re_{mix}}} = T_{re} (2v_{fr} + v_{re}) \left( \frac{A_{re_{mix}}}{\pi R^2} \right) \quad (2.19)$$

The  $A_{re_{mix}}$  is the mixed area and  $A_{re_{free}}$  represents the part of the rotor disc interested only by the freestream. By summing the three components, we obtain the total induced power of the tandem system:

$$P_{ind} = v_{fr} T_{fr} + \left( \frac{T_{re}}{\pi R^2} \right) \left[ v_{re} A_{re_{free}} + (2v_{fr} + v_{re}) A_{re_{mix}} \right] \quad (2.20)$$

The average induced velocity can be expressed as

$$\begin{aligned} v_{fr} &= \frac{T_{fr}}{2\pi R^2} pV \\ v_{re} &= \frac{T_{re}}{2\pi R^2} pV \end{aligned} \quad (2.21)$$

In the case of both rotors producing the same thrust, equal to  $T/2$ , the final expression for induced power is:

$$P_{ind} = \left( \frac{T^2}{\pi R^2} pV \right) \left[ \frac{1}{4} + \left( \frac{1}{4\pi R^2} \right) (A_{re_{free}} + 3A_{re_{mix}}) \right] \quad (2.22)$$

Stepniewski then adopts an adimensional factor,  $k_{ind_{ho}}$ , to evaluate the ratio between the induced power of the tandem system and the induced power of two isolated rotors:

$$k_{ind_{ho}} = \frac{P_{ind}}{2P_{ind_{\frac{1}{2}T}}} \quad (2.23)$$

And we obtain:

$$k_{ind_{ho}} = 2 \left[ \frac{1}{4} + \left( \frac{1}{4\pi R^2} \right) (A_{re_{free}} + 3A_{re_{mix}}) \right] \quad (2.24)$$

As can be seen in the Figure 2.10 for the two rotor in a coaxial configuration,  $k_{ind_{ho}}$  is equal to 2. The behaviour of the curve in respect to the factor  $h_{re}$  is then compared to measurement obtained by Boeing Vertol in wind-tunnel test, and shows a remarkable agreement with the theory.

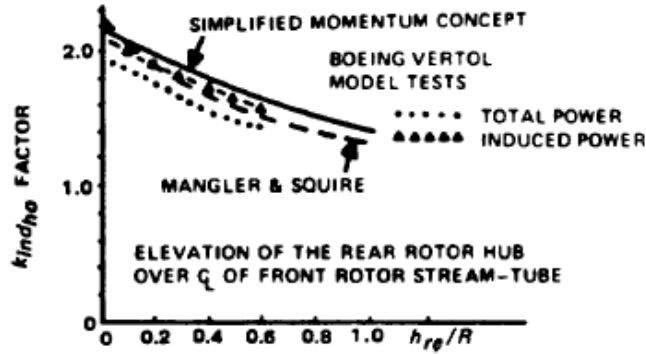


Figure 2.10: The  $k_{ind_{ho}}$  factor vs separation  $h_{re}$  (from [23])

Another study on the subject ([14]) shows results that agrees well with the theory, except for the case of full overlap, for which the theory seems to overestimate the induced power of the tandem system. Same for reference [24], where the lower values for the  $k_{ind_{ho}}$  are due to the closer spacing between the two rotors, where the contraction is not yet fully developed. Less contraction of the wake cause a reduced induced axial velocity in the impingement region, therefore decreasing the effect of the interaction.

This simplified approach based on momentum theory leaves out of the frame the tangential component of the slipstream, and is worth to understand how it's expected to have an influence on the rear propeller behaviour. Assuming that both propellers have the same rotational direction, looking at point A in reference 2.11 the blade section sees the induced tangential velocity from the front propeller  $v_{t_{fr}}$  opposing the rotational speed  $\Omega r$ , therefore causing the angle  $\phi$  to increase, reducing the local angle of attack. This reduced angle of attack causes the aerodynamic forces on the blade to be lower if compared to an ideal situation where only the axial component of the slipstream is present. On the other side, in B the tangential component increases the in-plane velocity causing an increased angle of attack therefore when the blade is in that position will generates more thrust compared to the previous mentioned situation.

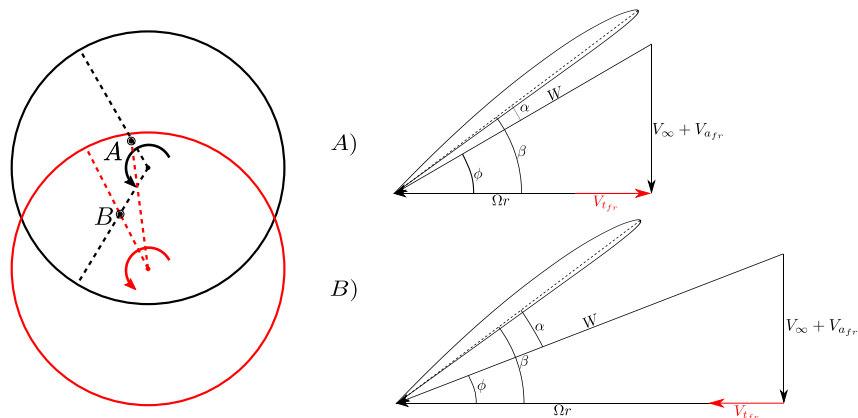


Figure 2.11: How the slipstream tangential component interacts with the blade section: in A) it opposes the rotational velocity; in B) it is in the same direction of the rotational velocity

# II

## METHODOLOGY



# 3

## NUMERICAL SETUP

In this chapter the methodology used in the numerical analysis is described, analysis performed to compute the effects of the interaction between the front propeller slipstream and the rear propeller. A schematic presentation of the approach followed is depicted in Figure 3.1.

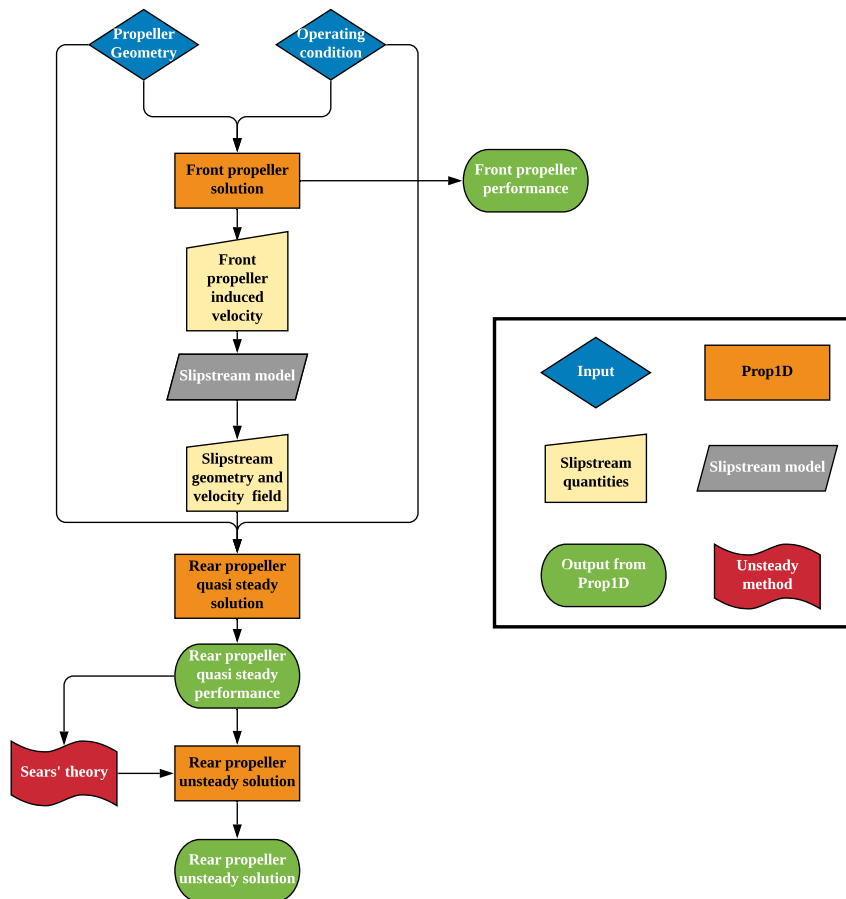


Figure 3.1: Schematic flowchart of the numerical approach used in this work

First, the front propeller loading distribution is solved as discussed in Section 5.2. Subsequently, from the solution of the front propeller it is possible to obtain the velocity distribution in the slipstream, as described in Section 3.2. At this point the superimposition of the slipstream "disturbance" field over the rear propeller disc is performed, and the effects on the rear propeller performance are discussed in Section 5.4.

### 3.1. ISOLATED PROPELLER SETUP

The main solution of the propeller is based on the BEMT program *Prop1D*, written in F77 language by Veldhuis and adapted for this particular study. The solution of the propeller loading performed by the program is based on the theory by Glauert [16] adapted to the blade element method, and uses the tip loss factor of Prandtl. The program needs the airfoil properties in term of sectional lift and drag coefficients,  $c_l$  and  $c_d$ , in order to evaluate the whole induced field for each element. In fact, obtaining the correct induced field, hence the right angles of attack and forces acting on the blade element, requires a convergence loop that iteratively evaluates the induced  $v_a$  and  $v_t$ . The main input for the program is, for each section, two polar curves for two different  $Re$  numbers, and then a bilinear interpolation is performed to obtain the appropriate values of the lift and drag coefficients. In Subsection 3.1.1 the procedure to obtain the airfoil properties is shown. The evaluation of the local angles and velocities acting on the airfoil is presented in 3.1.2, while in Subsection 3.1.3 it is shown how the program interpolates the input aerodynamic data in order to obtain the local thrust and torque. The induced velocity evaluation is described in Subsection 3.1.4 and finally in Subsection 3.1.5 the propeller is fully solved and the adimensional coefficients are evaluated.

#### 3.1.1. 2D AERODYNAMIC ANALYSIS

A BEMT code usually needs to be fast and not computationally expensive, and in order to achieve this goal usually the aerodynamic analysis is performed through a 2D sectional computation. Since the research aim of this thesis is to validate a method, a design and optimization process is not required, therefore the airfoils geometry is taken by the CAD model of the blade we are referring to. For the analysis 15 sections of the F29 propeller's blade are chosen, but in the program 6 more sections are taken into account by interpolating the values from the analyzed sections.

The tool used for the 2D analysis is RFOIL ([25], [26]), a modified and improved version of XFOIL developed by TU DELFT, ECN (Energy Research Center of Netherlands) and NLR (Netherland Aerospace Center) and it's mainly used for wind turbine studies. RFOIL is a 2D panel method and the transition calculation is based on the  $e^n$  method. The main improvements of this method compared to XFOIL are:

1. Improved convergence stability for high angle of attack
2. The closure relations for the turbulent boundary layer calculation have been adjusted, leading to an improved stability of the code
3. Correction to the evaluation of the maximum lift
4. Integration of the rotational effects

As cited by Rooij in [26]: *'In general the prediction of the airfoil characteristics with RFOIL will show a reduced drag coefficient of 10% and its prediction of the lift curve near stall will be reasonably well.'*

The tool is run by a MATLAB script that inputs into the program the desired requirements in terms of flow condition, transition properties and airfoil sections. A complete list of RFOIL inputs is presented below:

- Range of  $\alpha$  to perform the analysis
- Inflow velocity  $V_\infty$
- Rotational speed  $n$
- Radial position of the airfoil section  $\eta = r/R$
- Air properties like density  $\rho$ , viscosity  $\mu$  and speed of sound  $a$
- Critical amplification factor  $N$
- Airfoil properties like chord  $c$  and the profile geometry (either NACA digits or coordinates)
- Transition can be set either free or forced
- In order to evaluate the rotational effects, the chord to radius ratio  $c/r$  (or local solidity) is needed, along with the adimensional freestream velocity  $f_0$

The effective velocity that reaches the airfoil is evaluated as the resultant of the inflow velocity and the rotational:

$$W = \sqrt{V_\infty^2 + (\Omega r)^2} \quad (3.1)$$

The Reynolds number is evaluated based on the current  $W$  and section chord and is the main inflow input for the program:

$$Re = \frac{\rho c W}{\mu} \quad (3.2)$$

**COMPRESSIBILITY CORRECTION**

The outboard sections of a propeller blade usually operate in transonic range, and therefore a correction that takes this into account is needed, and the program uses a Karman-Tsien compressibility rule:

$$C_p = \frac{C_{p,0}}{\sqrt{1 - M_\infty^2 + \left[ M_\infty^2 / \left( 1 + \sqrt{1 - M_\infty^2} \right) \right]} C_{p,0}/2} \quad (3.3)$$

with  $M_\infty$  the Mach number of the freestream velocity and  $C_{p,0}$  the uncorrected pressure coefficient.

**ROTATIONAL EFFECTS**

Based upon the analysis by Snel [25], the effect of the rotation of the blade is taken into account. The rotational effects due to Coriolis and centrifugal forces are 'translated' into the local solidity  $c/r$  of the blade section. Due to this feature the code can be interpreted as a quasi-3D program. The Coriolis acceleration is given by:

$$a_{cor} = -2\Omega \times V_{rel} \quad (3.4)$$

With  $V_{rel}$  the velocity vector relative to the rotating propeller frame of reference. The centrifugal acceleration is given by:

$$a_{cen} = \Omega \times (\Omega r) \quad (3.5)$$

In the work of Himmelskamp [27] an increase in lift coefficient can be found going from the tip to the hub, combined with separation delayed to a higher angle of attack.

This approach shows to predict well the effects of rotation, and in reference [26] the main effects of the cross-flow are presented:

1. An increase in lift beyond sectional stall
2. Delayed and increased peak of maximum lift
3. Postponed turbulent separation
4. Increased maximum lift coefficient at the blade hub

All these effects can be explained by the influence of the Coriolis force acting on the boundary layer that, combined with the centrifugal force transports boundary layer material away from the hub, therefore stabilizing the boundary layer at the hub and leading to a better  $c_l - \alpha$  behaviour.

The in-built method that RFOIL integrates inside the analysis process is based on the  $c/R$ , but as cited both in references [26] and [25] the local solidity needs to be corrected by a factor of 2/3, since RFOIL tends to overestimate the effects of rotation.

In reference [25] it is also presented an engineering method that can be compared to the in-built solution, and is based on a correction of the non viscous solution and viscous solution without rotational effects.

Below the procedure for the correction of the lift coefficient is shown. With  $c_{l,inv}$  the lift coefficient given by the non viscous solution and  $c_{l,nonrot}$  the solution from RFOIL with the rotational method suppressed, the formula to obtain the rotational lift coefficient is:

$$\begin{aligned} c_{l,rot eff} &= c_{l,nonrot} + f_L(c_{l,inv} - c_{l,nonrot}) \\ \alpha_{rot eff} &= \alpha_{inv} = \alpha \end{aligned} \quad (3.6)$$

With  $f_L$ :

$$f_L = 1 - \left( 1 + \frac{c}{r} \right)^{B e^{(C/r)}} \quad (3.7)$$

With B and C obtained from two polynomials:

$$\begin{aligned} B &= b_1 + b_2\alpha + b_3\alpha^2 \\ C &= c_1 + c_2\alpha + c_3\alpha^2 \end{aligned} \quad (3.8)$$

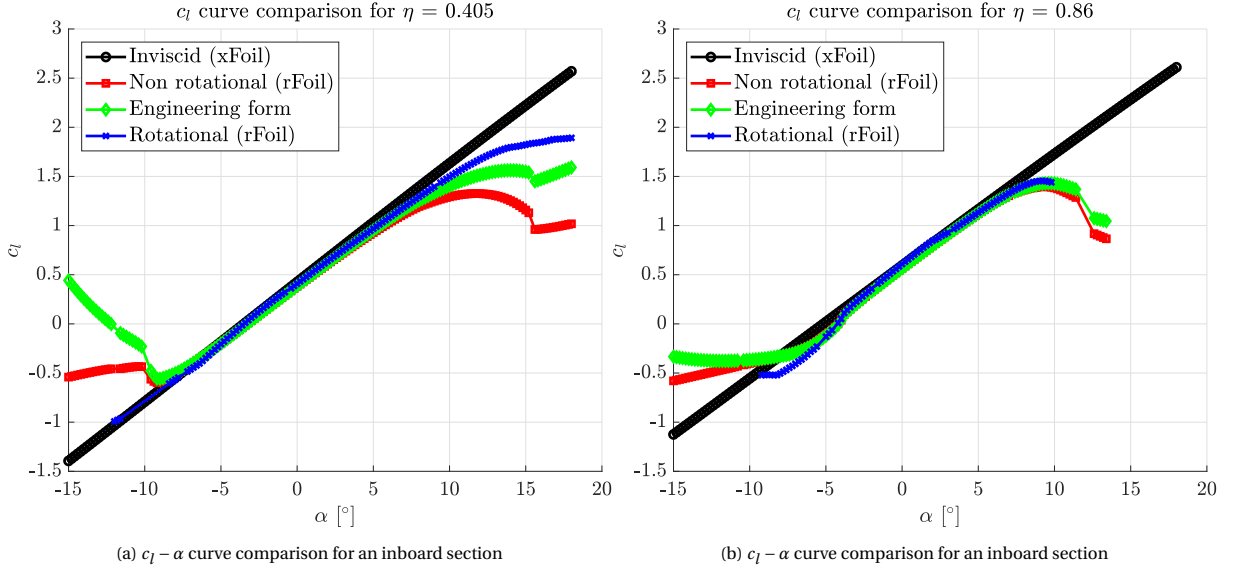


Figure 3.2: Comparison between  $c_l - \alpha$  curves that shows the difference between the in built method in RFOIL for rotational effects and the engineering method, for an inboard section in 3.2a and an outboard section in 3.2b

The comparison can be seen in Figure 3.2, with the curve generated by the engineering method that slightly underestimates the increased lift in the post stall region. The blade used for the analysis is a blade of TU Delft's XPROP research propeller. To obtain a more precise fit of the curve generated by Equation 3.6 the coefficients of the polynomials needs to be tuned. Moreover, it is worth noticing how for an inboard section the effects of the rotation are way more pronounced compared to the outboard part of the blade. Eventually the 2-D database was defined using the in built method in RFOIL, because computationally was slightly less expensive and faster and for the region of interests in terms of  $\alpha$ , between  $-5$  and  $10^\circ$  the  $c_l$  values are not so much different between the two approaches.

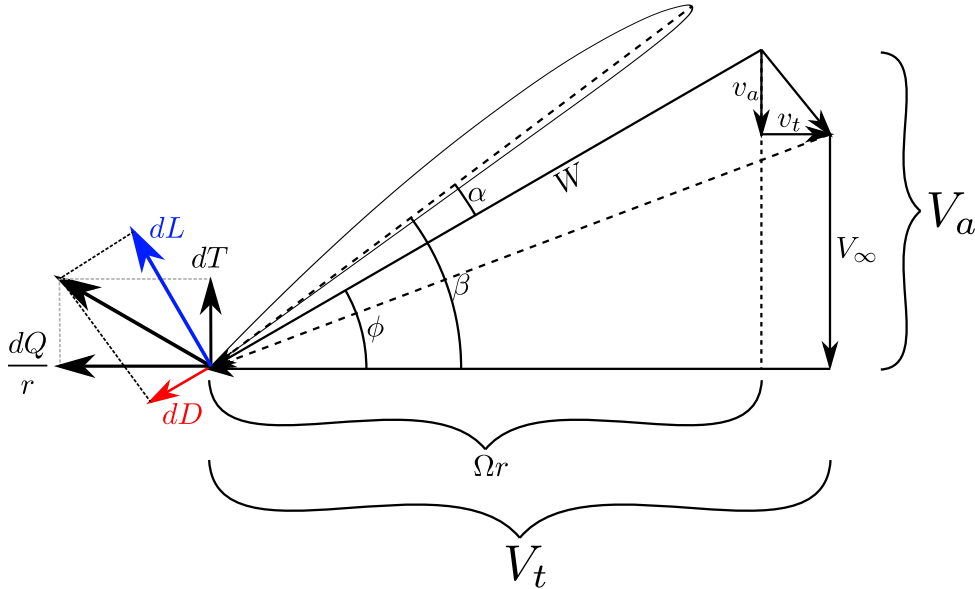


Figure 3.3: Velocities and forces reference frame on the blade element with induced velocities

### 3.1.2. EVALUATION OF SECTIONAL ANGLE OF ATTACK

After the input section, the program evaluates the aerodynamic angles with respect to the airfoil chord, as shown in Figure 3.3. The axial and in-plane components of the velocity are derived as such:

$$V_a(\eta, \Psi) = V_\infty \cos(\alpha_p) + v_a(\eta, \Psi) \quad (3.9)$$

$$V_t(\eta, \Psi) = \Omega r(\eta, \Psi) - v_t(\eta, \Psi) + V_\infty \sin(\alpha_p) \sin(\Psi) \quad (3.10)$$

The local incidence is defined as:

$$\phi(\eta, \Psi) = \tan\left(\frac{V_a(\eta, \Psi)}{V_t(\eta, \Psi)}\right) \quad (3.11)$$

Hence, the local angle of attack is:

$$\alpha(\eta, \Psi) = \beta(\eta, \Psi) - \phi(\eta, \Psi) \quad (3.12)$$

The effective velocity  $W$  is needed to evaluate the  $Re$  number:

$$W(\eta, \Psi) = \sqrt{V_a^2(\eta, \Psi) + V_t^2(\eta, \Psi)} \quad (3.13)$$

$$Re(\eta, \Psi) = \frac{\rho c(\eta) W(\eta, \Psi)}{\mu} \quad (3.14)$$

### 3.1.3. EVALUATION OF SECTIONAL THRUST AND TORQUE

The bilinear interpolation uses the 2-D sectional data previously obtained and the  $Re$  number and the  $\alpha$  evaluated in the previous section. In the following equations the values from the airfoil analysis are denoted with the subscripts 1 and 2. Two fractions are used to determine the interpolated values, the first one involves the  $Re$  numbers:

$$fr = \frac{Re - Re_1}{Re_2 - Re_1} \quad (3.15)$$

It is now necessary to interpolate between the given aerodynamic coefficients, and to do so the program evaluates the second fraction by choosing two values of  $\alpha$  from the given polars so that the previously calculated  $\alpha$  is included between the two.

$$fr_\alpha = \frac{\alpha - \alpha^-}{\alpha^+ - \alpha^-} \quad (3.16)$$

The program now actually interpolates between the input data to get the correct values of  $c_l$  and  $c_d$ :

$$\begin{aligned} c_l(\eta, \Psi) &= fr_\alpha(fr c_{l,2}^+ + (1 - fr)c_{l,1}^+) + (1 - fr_\alpha)(fr c_{l,2}^- + (1 - fr)c_{l,1}^-) \\ c_d(\eta, \Psi) &= fr_\alpha(fr c_{d,2}^+ + (1 - fr)c_{d,1}^+) + (1 - fr_\alpha)(fr c_{d,2}^- + (1 - fr)c_{d,1}^-) \end{aligned} \quad (3.17)$$

It is now possible to evaluate the sectional thrust and torque per radial element  $dr$ :

$$\begin{aligned} \frac{dT}{dr}(\eta, \Psi) &= \frac{1}{2} \rho W^2 B c (c_l \cos(\phi) - c_d \sin(\phi)) \\ \frac{dQ}{dr}(\eta, \Psi) &= \frac{1}{2} \rho W^2 B c r (c_l \sin(\phi) + c_d \cos(\phi)) \end{aligned} \quad (3.18)$$

### 3.1.4. EVALUATION OF INDUCED VELOCITIES

Now that we have the sectional thrust and torque it is possible to obtain the axial and tangential components of the induced field. The cause of the induced velocity is explained in Subsection 2.2.1 and the method followed by the code is based upon the conclusion given by Glauert in reference [16].

First of all, the code integrates the Prandtl loss factor in its most general form. Prandtl realized that the fluid velocity between the vortex sheets generated by the blade, is a fraction  $F$  of the vortex sheets velocity. Prandtl proved that this flow was similar to a 2-dimensional flow along edges of parallel plates, as depicted in Figure 3.4

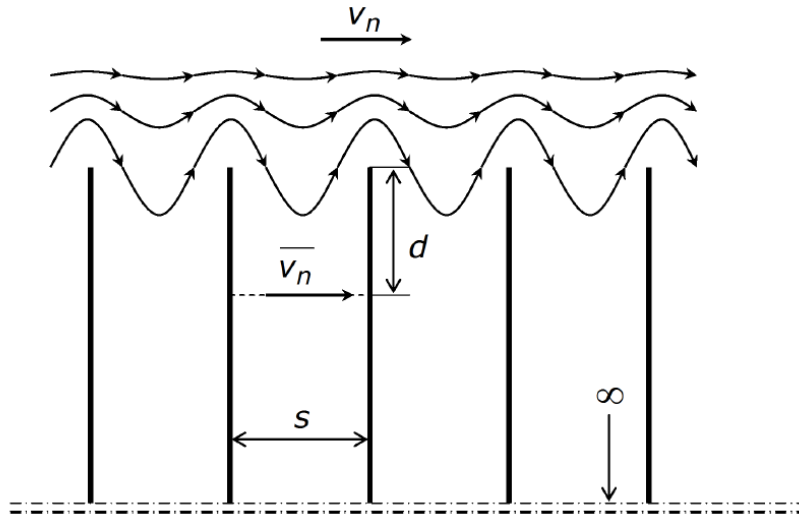


Figure 3.4: Two dimensional flow along semi-infinite plates (from [18])

The Prandtl tip loss factor used is defined by:

$$F_{tip} = \frac{2}{\pi} \arccos(e^{-f_{tip}}) \quad (3.19)$$

With:

$$f_{tip} = \frac{B}{2} \frac{D/2 - r}{r \sin(\phi_t)} \quad (3.20)$$

with  $\Phi_t = \arctan(\eta \tan(\Phi))$ .

The same approach can be used to estimate the loss effect due to the hub vortex:

$$F_{hub} = \frac{2}{\pi} \arccos(e^{-f_{hub}}) \quad (3.21)$$

With:

$$f_{hub} = \frac{B}{2} \frac{r - r_{hub}}{r \sin(\phi_t)} \quad (3.22)$$

Hence the loss factor used in the program is the product of the two factors:

$$F = F_{tip} \cdot F_{hub} \quad (3.23)$$

The loss factor is then applied to the axial momentum equation in order to evaluate the induced velocity components, which in the first step of the iteration are both set to 0. Once that the new values  $v_a$  and  $v_t$  are evaluated, the program checks the difference between the old and new values to see if convergence is reached. The axial momentum equation with loss factor for each blade element is:

$$\frac{dT}{dr} = 4\pi r \rho (V_\infty \cos(\alpha_p))^2 (1 + a) a F \quad (3.24)$$

With  $a = v_a / V_\infty \cos(\alpha_p)$ . Inverting the equation we obtain:

$$v_a(\eta, \Psi) = -\frac{1}{2} (V_\infty \cos(\alpha_p)) + \frac{1}{2} \sqrt{(V_\infty \cos(\alpha_p))^2 + \frac{dT/dr}{\pi F \rho r}} \quad (3.25)$$

Same can be done for the angular momentum equation:

$$\frac{dQ}{dr} = 4\pi r^3 \rho V_\infty \cos(\alpha_p) \Omega (1 + a) a_t F \quad (3.26)$$

With  $a_t = v_t / \Omega r$ . The tangential induced velocity is:

$$v_t(\eta, \Psi) = \frac{dQ/dr}{4\pi F \rho r^2 (V_\infty \cos(\alpha_p) + v_a)} \quad (3.27)$$

### 3.1.5. EVALUATION OF TOTAL FORCES AND PERFORMANCE OF THE PROPELLER

After the convergence of the induced velocity, the propeller total thrust and torque are computed. With  $\eta$  the radial coordinate ( $r/R$ ) and  $\Psi$  the azimuthal angle, the quantities for each azimuthal position are obtained by summing the contributions of each blade element:

$$T_{\psi} = \sum_{k=2}^{TOT_{\eta}} \frac{1}{2} \left[ \left( \frac{r}{R} \right)_k - \left( \frac{r}{R} \right)_{k-1} \right] \frac{(dT/dr)_k + (dT/dr)_{k-1}}{B} R \quad (3.28)$$

$$Q_{\psi} = \sum_{k=2}^{TOT_{\eta}} \frac{1}{2} \left[ \left( \frac{r}{R} \right)_k - \left( \frac{r}{R} \right)_{k-1} \right] \frac{(dQ/dr)_k + (dQ/dr)_{k-1}}{B} R \quad (3.29)$$

While the contribution of each blade is obtained by summing each azimuthal contribution and dividing it by the angular divisions used for the analysis. In case of uniform inflow only one azimuthal position is studied and its load distribution is used as the solution for the whole propeller. But in case of non uniformity in the inflow distribution, since at every  $\Psi$  location the load distribution can be different, it is necessary to average each contributes over the whole rotation. The quantities for each blade are given by:

$$T_B = \frac{\sum_{i=1}^{TOT_{\psi}} T_{\psi}}{TOT_{\psi}} \quad (3.30)$$

$$Q_B = \frac{\sum_{i=1}^{TOT_{\psi}} Q_{\psi}}{TOT_{\psi}} \quad (3.31)$$

Finally the thrust and torque of the entire propeller are:

$$T_{TOT} = T_B \cdot B \quad (3.32)$$

$$Q_{TOT} = Q_B \cdot B \quad (3.33)$$

Once obtained the torque it's possible to compute the power as:

$$P_{TOT} = 2\pi n Q_{TOT} \quad (3.34)$$

From the total thrust and torque is possible to obtain the corresponding thrust and torque coefficients:

$$C_T = \frac{T_{TOT}}{\rho n^2 D^4} \quad (3.35)$$

$$C_Q = \frac{Q_{TOT}}{\rho n^2 D^5} \quad (3.36)$$

Same for the power coefficient:

$$C_P = \frac{P_{TOT}}{\rho n^3 D^5} \quad (3.37)$$

The efficiency is another important parameter useful to estimate the performance of the propeller, and is given by

$$\eta = \frac{C_T J}{C_P} \quad (3.38)$$

### 3.1.6. VALIDATION OF THE PROGRAM

In Chapter 7 the comparison of the experimental and numerical results can also be seen as a way to validate the numerical methodology used in the present work. However, another comparison with experimental data for another propeller is presented in this subsection. The propeller used is the XPROP, of which the experimental data have been obtained in the OJF and are presented in [28].

In Figure 3.5 it's possible to appreciate the results of the program compared to the experimental data, in terms of the  $C_T$ ,  $C_P$  and efficiency  $\eta$  distribution. The range of advance ratio spans between 0.35 and 0.79, for an

inflow velocity of 18 m/s.

By looking at the  $C_T$  distribution it's possible to see how the program overall overestimates the thrust of the propeller. In particular in the high advance ratio area the discrepancy is even more pronounced. This is due to an overestimation of the sectional lift performed by RFOIL, considering the fact that in this region the whole blade operates at very low Reynolds, therefore the analysis is inaccurate. It's also worth noticing how the whole slope of the  $C_T$  curve is different and this can be due to an overestimated  $c_{l\alpha}$  for each section.

The power, on the other hand, is slight underestimated, and this is because the sectional drag is lower than the effective value, therefore the propeller as solved by the program is more efficient, compared to the real one, for the whole range of advance ratios.

It should be noted that the critical factor used in RFOIL is  $N = 4$ . The effects of the critical factor is discussed in Appendix A for the F29 propeller, the one used for the interaction analysis proposed in this report.

However we can consider the evaluations performed by the program quite reasonable, and especially for the high  $C_T$  region (low advance ratio) the results are almost on top of each other.

Experimental data of the propeller in angle of attack were available, therefore it's possible to see in Figures 3.6 and in 3.7 the comparison of  $C_T$  and  $C_P$  for three different  $\alpha_p$ :  $0^\circ$ ,  $15^\circ$  and  $30^\circ$ . The increase in thrust due to the increased angle of attack is well predicted by the program. As in the case of uniform inflow, also for  $\alpha_p=15^\circ$  the computed thrust coefficient is overpredicted, especially for the higher values of  $J$ . For  $\alpha_p=30^\circ$  the computed  $C_T$  is on top of the experiment results. This can be explained by the fact that now the program underestimates the effect of the reduced axial velocity that causes an increased load distribution on the propeller. However, even the slope of both curves are more similar to each other.

Looking at the  $C_P$  curves comparison, it is possible to see how for each inflow condition the power is underestimated by the program.

It's important to say that for the analysis of the propeller for  $\alpha_p=15^\circ$  and  $30^\circ$  is performed using the same aerodynamic data as in the uniform analysis. Considering this, the program is able to predict well the effects of a non uniform inflow.

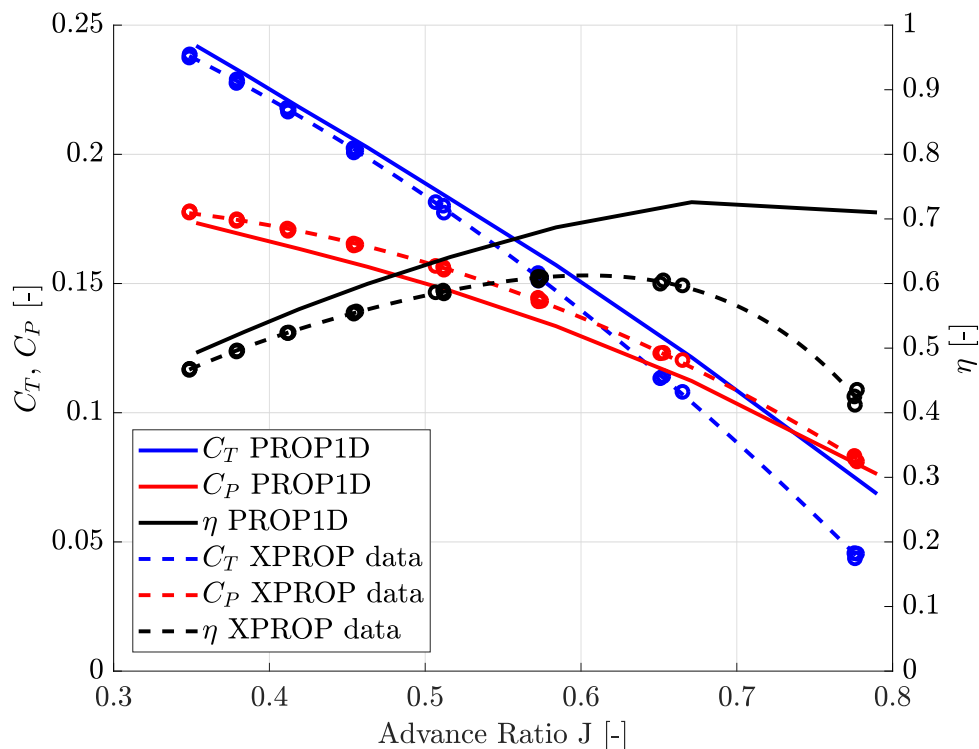


Figure 3.5:  $C_T$ ,  $C_P$  and  $\eta$  comparison from the program Prop1D and experimental results for  $J=[0.35-0.79]$ ,  $V_\infty=18$  m/s and a blade pitch  $\beta=20^\circ$ .

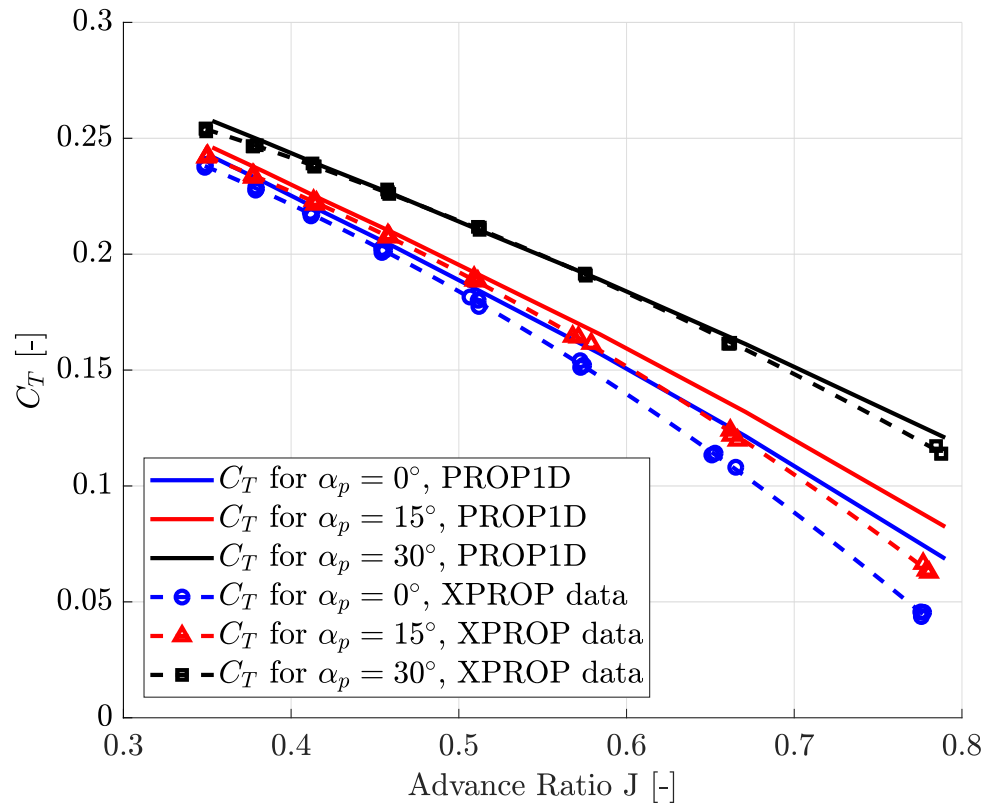


Figure 3.6: Comparison of  $C_T$  curves for three different propeller angle of attack values:  $\alpha_p = 0^\circ$ ,  $15^\circ$  and  $30^\circ$ .

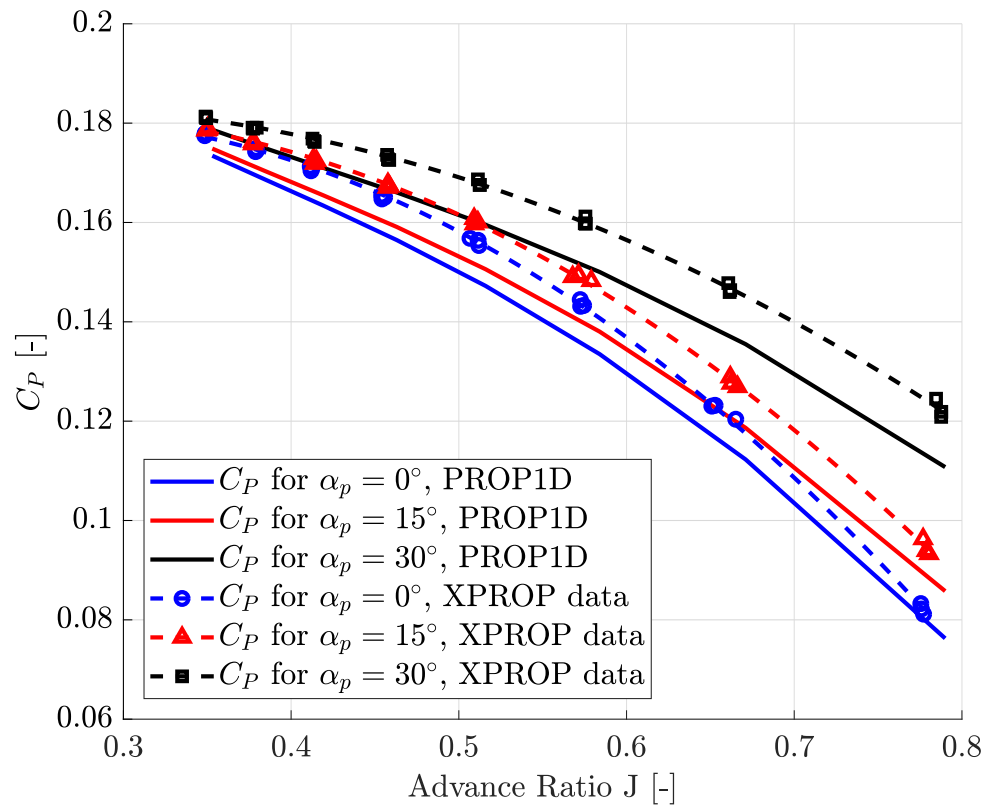


Figure 3.7: Comparison of  $C_P$  curves for three different propeller angle of attack values:  $\alpha_p = 0^\circ$ ,  $15^\circ$  and  $30^\circ$ .

### 3.2. SLIPSTREAM MODEL

The slipstream model used is based on the momentum theory and the blade element theory, and is presented in the work of Chandrasekaran [29]. This method does not provide an accurate nor time dependent model of the slipstream but thanks to its simplicity it was easily integrated in the method.

The approach is that, given the flow characteristics at the propeller disc, it is possible to compute the evolution along the slipstream axis of the slipstream geometry and axial and tangential velocity components. By doing this it is possible to build a 3-D grid, where we have the quantities (induced velocity components) at any point, and we can use them to model the non uniform inflow that impinges the rear propeller disc.

From now on the quantities related to the slipstream will be characterized by an  $_s$  subscript, while the ones related to the rear propeller by  $_r$ .

At first it was necessary to define the input from the front propeller solution, as presented in Subsection 3.2.1. Thereafter, the computation of the axial and tangential velocity distribution along the slipstream are shown in Subsections 3.2.2 and 3.2.3. Finally, the last step to define the non uniform inflow at the rear propeller position is described in Subsection 3.2.4

#### 3.2.1. INPUT FROM THE FRONT PROPELLER SOLUTION

From the front propeller solution, we have the axial and tangential velocity evaluated as in Equations 3.25 and 3.27. These values are computed taking into account the loss factor  $F$ , because they are used in a convergence loop that iteratively changes the angle of attack on the blade section, therefore leading the solution to the correct load distribution on the blade element and finally on the whole propeller.

However, the distribution of these velocities along the radius does not correspond to a "physically correct" induced velocity distribution that is present behind a propeller. And this is because we are applying a correction ( $F$ ) when we apply the momentum equation to obtain the effects on the flow due to the momentum imparted by the propeller load distribution.

Therefore, to obtain the "physical" distribution of induced velocity we need the following relations, given the load per blade element obtained after the convergence:

$$v_{a,s} = -\frac{1}{2}(V_\infty \cos(\alpha_p)) + \frac{1}{2}\sqrt{(V_\infty \cos(\alpha_p))^2 + \frac{dT/dr}{\pi\rho r}} \quad (3.39)$$

$$v_{t,s} = \frac{dQ/dr}{4\pi\rho r^2(V_\infty \cos(\alpha_p) + v_a)} \quad (3.40)$$

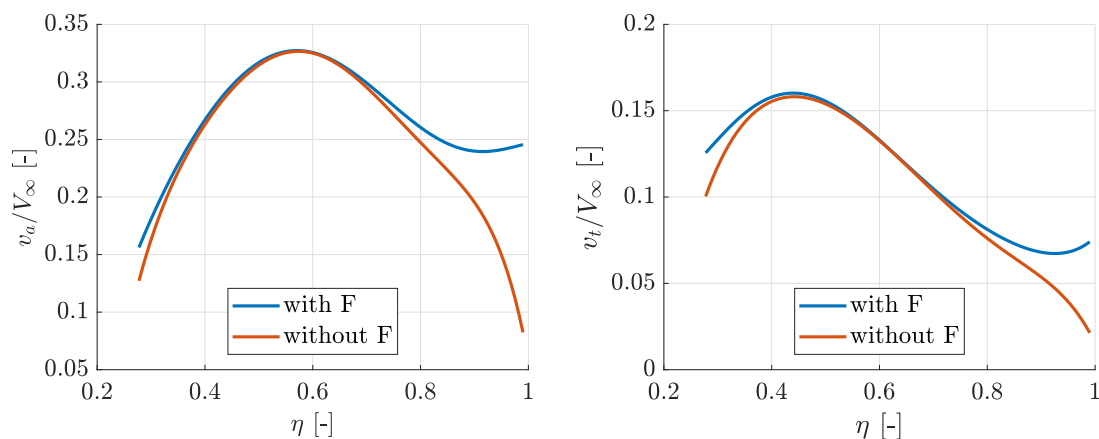


Figure 3.8: Induced axial and tangential components of the velocity (normalized with the freestream velocity) with and without loss factor.

In Figure 3.8 the two radial distributions of induced velocity are compared, in terms of factors  $a$  and  $a'_t = v_t/V_\infty$ , both for the axial and tangential component. It's possible to see clearly how the induced velocity used in the convergence loop due to the loss factor applied both at the hub and tip region is higher than the quantity obtained by Equations 3.39 and 3.40. The situation at the tip is dramatic, with the velocity that not only is not going to zero (as the load on the blade) but it's even experiencing a rising behaviour.

### 3.2.2. EVALUATION OF THE AXIAL INDUCED VELOCITY

The method incorporates two theories for calculating the axial induced velocity: vortex ring modelling and blade element theory (in reference [29] it's called *Blade Performance Theory*).

#### VORTEX RING MODELLING

The vortex system for this part of the method is based on the principle that along the blade a bound vortex is present. At the root and at the tip two free vortices are carried downwind by the flow that invests the propeller. As shown in Subsection 2.2.1 the vortex system behind the propeller can be simplified by considering separately the axial and tangential vorticity. Since the axial vorticity has no effects on the axial direction of the flow, the tangential component can be represented as a stack of vortex rings, spaced so closely that they are equivalent to a continuous cylinder of vorticity.

The strength of the vorticity is determined by the load on the propeller and its operating condition. It is now assumed that the axial induced velocity does not change with the radius, and its value at the center of the propeller disc is given by the following relations, taken from Ref. [29].

$$v_{I,c} = \frac{1}{2} C_T^1 V_T \frac{A_{eff}}{(\mu^2 + \lambda^2)^{\frac{1}{2}}} \quad (3.41)$$

$$\begin{aligned} C_T^1 &= \frac{4}{\pi^3} C_T \\ \lambda &= \frac{(V_\infty + v_I)}{V_{tip}} \\ \mu &= \frac{V_\infty}{V_{tip}} \\ A_{eff} &= \frac{1}{1 - R_{hub}^2} \end{aligned}$$

where  $v_{I,c}$  is the induced velocity at the center of the propeller,  $V_{tip} = \Omega R_p$  is the tip velocity of the blade and  $C_T$  is the thrust coefficient of the propeller.

Equation 3.41 is a nonlinear equation and it's solved iteratively with its initial value obtained from

$$v_{I,c}^0 = \frac{1}{2} \left( -V_\infty + \sqrt{(V_\infty \cos(\alpha_p))^2 + \frac{2T}{\rho A_0}} \right) \quad (3.42)$$

where  $T$  is the thrust of the propeller and  $A_0$  is the whole area of the propeller disc.  $V_{I,c}^0$  is substituted in the definition of  $\lambda$  and Equation 3.41 is iterated until convergence.

The variation of the axial induced velocity with the axial position is given by

$$v_I(\zeta) = v_{I,c} \left( 1 + \frac{\zeta}{\sqrt{1 + (\zeta)^2}} \right) \quad (3.43)$$

We are able to obtain the external radius of the slipstream at any point behind the slipstream by satisfying the continuity relation:

$$\begin{aligned} \rho \pi R_p^2 (V_\infty + v_{I,c}) &= \rho \pi r^2(\zeta) (V_\infty + v_I(\zeta)) \\ r(\zeta) &= R_p \sqrt{\frac{(V_\infty + v_{I,c})}{(V_\infty + v_I(\zeta))}} \end{aligned} \quad (3.44)$$

#### BLADE ELEMENT THEORY

By referring to Figure 3.9 the radius variation computed with Equation 3.44 represents the contraction of the slipstream. The next step is to consider the induced velocity distribution on the propeller disc as it was determined by the BEM, we can imagine that a streamline is shed by each blade element, therefore the radial distance of the element  $R_s$  is the starting radius of the streamline. By referring to the external slipstream radius as  $R_{loc}$ ,  $R_{s,loc}$  is defined by

$$R_{s,loc}(\zeta) = \frac{R_{loc}(\zeta)}{R_p} R_s$$

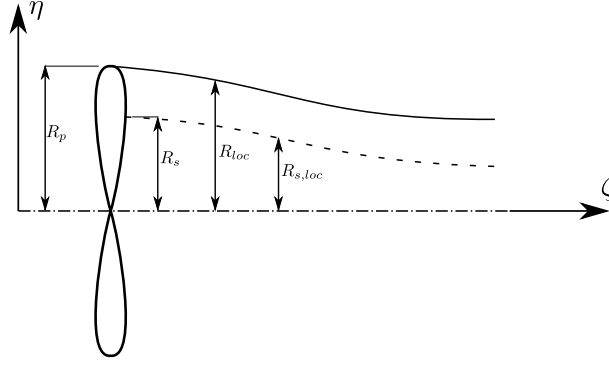


Figure 3.9: Schematic representation of the contraction for each streamline (derived from [29])

Therefore, we are assuming that each slipstream has the same contraction ratio of the slipstream. This is not necessarily a strong assumption, but has the disadvantage to not predict well the contraction of the internal boundary of the slipstream, at the hub location.

The variation of the axial induced velocity for each streamline is

$$v_{a,s}(\eta, \Psi, \zeta) = v_{a,s}(\eta, \Psi, 0) \left( 1 + \frac{\zeta}{\sqrt{1 + (\zeta)^2}} \right) \quad (3.45)$$

### 3.2.3. EVALUATION OF THE TANGENTIAL INDUCED VELOCITY

It can be demonstrated that in the slipstream of the propeller, the circulation  $\Gamma$  remains constant, as presented in Ref. [30]. Due to the contraction, the radius of the slipstream decreases, and according to the conservation of the circulation, the tangential velocity increases. This is true for each control volume defined by the streamline of each blade station. The conservation of the circulation is given by:

$$2\pi R_s(\eta, \Psi, 0) 2v_{t,s}(\eta, \Psi, 0) F = 2\pi R_s(\eta, \Psi, \zeta) v_{t,s}(\eta, \Psi, \zeta) F_s \quad (3.46)$$

$F$  is the tip loss factor at the propeller, while  $F_s$  is the loss factor in the slipstream, assumed to be unity.  $v_{t,s}(\eta, \Psi, 0)$  is the tangential velocity in the propeller plane. As shown in Subsection 2.2.1 the tangential component right behind the propeller is twice its value at the propeller disc. Therefore by inverting Equation 3.46 we obtain

$$v_{t,s}(\eta, \Psi, \zeta) = 2v_{t,s}(\eta, \zeta) F \frac{R_s(\eta, \Psi, 0)}{R_s(\eta, \Psi, \zeta)} \quad (3.47)$$

The swirl angle is evaluated from the following expression:

$$\Theta_{sw} = \arctan \left[ \frac{2v_{t,s}}{V_\infty + v_{a,s}} \right] \quad (3.48)$$

### 3.2.4. DEFINING THE INPUT FOR THE REAR PROPELLER

In Figure 3.10 the solution provided by the model is briefly presented. The quantities shown are the slipstream ratio of contraction and the variation of axial and tangential induced factors  $a = v_a/V_\infty$  and  $a'_t = v_t/V_\infty$ , normalized with the freestream velocity, for two different rotational speeds of the propeller, and it's possible to appreciate how the load on the propeller changes drastically how the slipstreams behaves.

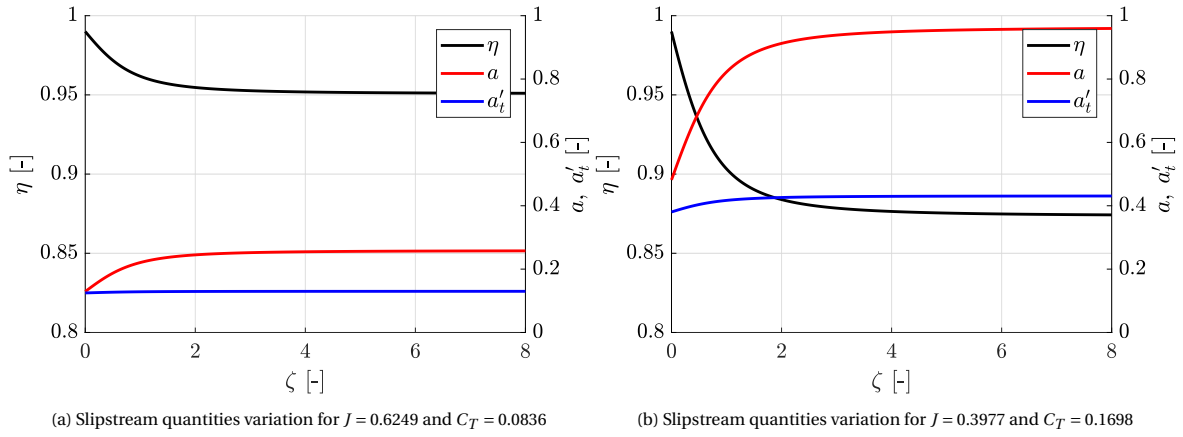


Figure 3.10: Slipstream contraction and variation of the mean axial and tangential induced factors for a lightly loaded propeller and a heavily loaded one

For a lightly loaded propeller (figure 3.10a) the slipstream radius when fully developed is 5% less than the propeller radius, while for a much heavily loaded propeller (figure 3.10b) the contraction is more than the 10% of the propeller radius.

The axial induced velocity behaviour agrees well with the theory, in fact for both cases reaches a value that is more or less twice the one at the propeller location. Obviously we can also appreciate how for an highly loaded propeller in the far wake the ratio of induced axial velocity and freestream velocity is almost equal to 1, because of the greater circulation due to the heavier aerodynamic load.

As expected, the tangential velocity variation is not that relevant and it stays more or less constant.

It's worth to mention how in this model the contraction region is limited to a region that goes from the propeller disc to  $\zeta \approx 2$ , this means that at a distance of one propeller diameter the slipstream can be considered fully developed.

At this point we are able to know the distribution of the velocity at any desirable position behind the propeller. The approach followed in this part consists in a superimposition of the velocity field from the slipstream to the rear propeller disc. In practice this is done through a bilinear interpolation of two polar grids, where the values of the one relative to the slipstream section are interpolated over the propeller grid. A schematization of the two polar grids is shown in Figure 3.11, where the points of each grid are defined by two different polar coordinate systems.

The function `griddata` of Matlab, used for the interpolation, treats the points of the first grid as scattered data and returns the interpolated values over the propeller grid, defined as the query points.

The superimposition of the induced velocity does not require any particular adjustment, because its direction is parallel to the  $x$  axis, which is common for both reference systems.

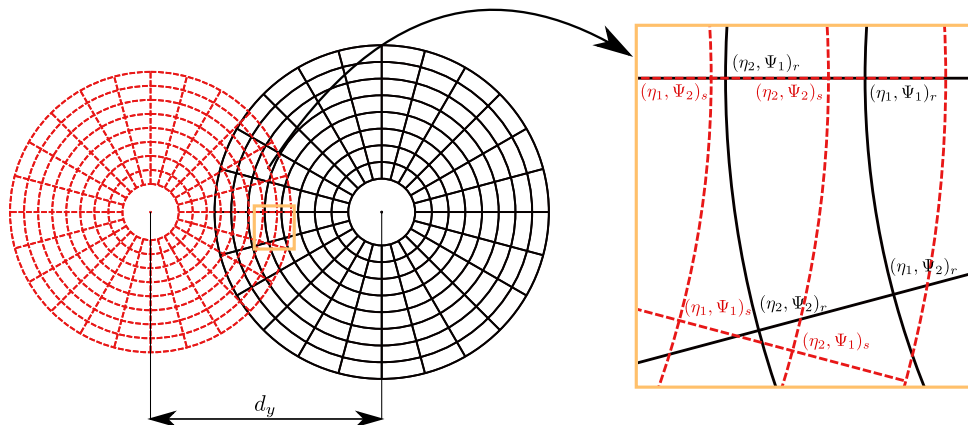


Figure 3.11: The slipstream grid (in red) and the propeller grid (in black).

The tangential component, on the other hand, requires to be adapted since its value it's relative to the polar coordinate system of the slipstream grid. Therefore, a transformation from polar to cartesian coordinate is performed as shown in Figure 3.12, and the two components  $v_{y,s}$  and  $v_{z,s}$  are given by the following relations:

$$\begin{aligned} v_{y,s} &= v_{t,s} \cos(\Psi) \\ v_{z,s} &= -v_{t,s} \sin(\Psi) \end{aligned} \quad (3.49)$$

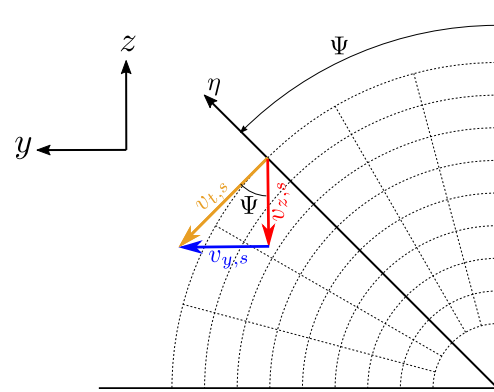


Figure 3.12: Cartesian components of the slipstream tangential velocity

Finally we can associate to each point of the polar grid, relative to the rear propeller, the values of  $v_{a,s}$ ,  $v_{y,s}$  and  $v_{z,s}$  and in the following section the analysis is presented.

### 3.3. REAR PROPELLER SETUP

The body of the code that solves the rear propeller is the same used for the front one, modified in order to evaluate the non-uniform inflow, i.e. the axial and in-plane components of the slipstream velocity.

Due to the non-uniform inflow the blade, when passing through the impingement area, experiences an unsteady flow that results in unsteady loads on the blade. The effects of this time-varying inflow seen by the rotating blade are going to be studied as following:

1. *Quasi steady solution of the propeller*

The solution is computed by assuming that each azimuthal section is representative of the whole propeller, as the front propeller is solved as shown in Section 5.2.

2. *Unsteady solution of the propeller*

The results obtained by the quasi steady solution are used as input for an unsteady solution, based on the work of Sears' 1D unsteady theory, is adopted. The approach is described in references [31] and [32], while in [33] it's applied to a case of interaction between a propeller and a pylon's wake.

#### 3.3.1. QUASI STEADY ANALYSIS

The quasi steady solution follows the same steps presented in Section 5.2, therefore the slipstream velocity components  $v_{a,s}$ ,  $v_{x,s}$  and  $v_{y,s}$  are used appropriately in the solution of each blade element. Once that each element of the blade is solved for an azimuthal position, the program switches to the next  $\Psi$  and the procedure is repeated.

It's important to mention that since this is a quasi steady solution, its main assumption is that each blade element, when analyzed, becomes representative of the whole propeller, therefore its local inflow it's assumed to be the total inflow that invests the propeller.

As said before, the general solution is still valid and already presented extensively. However, it is now necessary to incorporate the slipstream velocity.

In order to handle properly the in-plane component, it's necessary a second transformation of the values presented in Equation 3.49 from the cartesian plane to the polar coordinate system of the propeller.

Assuming that the radial component has no effects, the new tangential velocity that invests the rear propeller disc is given by:

$$v_{t,s}(\eta, \Psi) = v_{y,s}(\eta, \Psi) \cos(\Psi) - v_{z,s}(\eta, \Psi) \sin(\Psi) \quad (3.50)$$

Therefore the new axial and in plane velocities<sup>1</sup> that are used to evaluate the angle of attack are:

$$V_{a,r}(\eta, \Psi) = V_{\infty} + v_{a,r}(\eta, \Psi) + v_{a,s}(\eta, \Psi) \quad (3.51)$$

$$V_{t,r}(\eta, \Psi) = \Omega r(\eta, \Psi) - v_{t,r}(\eta, \Psi) + V_{\infty} - v_{t,s}(\eta, \Psi) \quad (3.52)$$

<sup>1</sup>  $\alpha_p = 0^\circ$

By knowing the two components of the velocity we obtain the local incidence and subsequently the local  $\alpha_r(\eta, \Psi)$

$$\alpha_r(\eta, \Psi) = \beta(\eta, \Psi) - \phi(\eta, \Psi) \quad (3.53)$$

With

$$\phi(\eta, \Psi) = \tan\left(\frac{V_{ax,r}(\eta, Psi)}{V_{tan,r}(\eta, \Psi)}\right)$$

The program then performs the bilinear interpolation described in Subsection 3.1.3, obtaining the local  $c_{l,QS}$  and  $c_{d,QS}$ , used for the evaluation of the sectional contributes to the thrust, normal force and torque of the blade element.

As the output of the quasi steady analysis we have the radial and azimuthal distribution of every aerodynamic and performance quantities.

At this point we can proceed with the unsteady analysis.

### 3.3.2. UNSTEADY ANALYSIS

The unsteady analysis used in the present work to compute the change in blade loads due to the variation of the angle of attack in the slipstream impingement region is based on the Sears' method, described in references [31] and [32]. Once that the results in terms of lift coefficients are evaluated, they are integrated with the results obtained from the quasi steady solution in order to obtain the final response. Only the lift is considered, while the drag coefficients used in the final computation are the one evaluated from the quasi steady analysis.

Due to the peculiarity of this interaction, some modification have been applied but the fundamental core of the method is unchanged.

#### COMPUTATION OF THE ANGLE OF ATTACK VARIATION

The main input for this method is going to be the periodic distribution of angle of attack  $\alpha_r(\eta, \Psi)$  that a blade element sees along the rotation. In order to obtain the blade response only due to the variation the periodic distribution of angle of attack is subtracted by its mean.

Since the computation of the unsteady response is done in the frequency domain, it's necessary to express the variation of  $\alpha_r(\eta, \Psi)$  as a complex Fourier series:

$$\alpha_r(\eta, \Psi) = \sum_{k=-\infty}^{\infty} \alpha_{r,k}(\eta) e^{ik\Psi} \quad (3.54)$$

with  $k$  the harmonic order and  $\alpha_{r,k}$  the Fourier coefficients, given by:

$$\alpha_{r,k}(\eta) = \frac{1}{2\pi} \int_0^{2\pi} \alpha_r(\eta, \Psi) e^{-ik\Psi} d\Psi \quad (3.55)$$

The Fourier coefficients are the input for the actual computation of the unsteady load as discussed next.

#### COMPUTATION OF THE BLADE RESPONSE

For each radial segment, the effect of the variation of the angle of attack due to the slipstream impingement is computed. The Fourier coefficients of the blade response, or better the harmonics of the unsteady lift coefficient are defined by:

$$\Delta c_{l,k}(\eta) = 2\pi \alpha_{r,k}(\eta) S \quad (3.56)$$

With  $S$  the Sears function. The incompressible form of the Sears function, as in reference [31]:

$$S(\sigma) = [J_0(\sigma) - iJ_1(\sigma)] C(\sigma) + iJ_1(\sigma) = \frac{J_0(\sigma)K_1(\sigma) + iJ_1(\sigma)K_0(\sigma)}{K_1(i\sigma) + K_0(i\sigma)} \quad (3.57)$$

with  $C$  the Theodorsen's function,  $J_0$  and  $J_1$  the zeroth- and first-order Bessel functions of the first kind,  $K_0$  and  $K_1$  the modified zeroth- and first-order Bessel function of the second kind and  $\sigma$  the reduced frequency:

$$\sigma = \frac{k\Omega c}{2W_{QS}}$$

Due to the rotation of the propeller the local effective Mach numbers in the outboard region are typically close to values for which the compressibility effects become relevant. Therefore, the Sears function with a correction for compressibility is given by:

$$S(\sigma, M) = \frac{S_{M=0}(\sigma/\beta_{compr})}{\beta_{compr}} \left\{ J_0 \left( \frac{M^2 \sigma}{\beta_{compr}^2} \right) + i J_1 \left( \frac{M^2 \sigma}{\beta_{compr}^2} \right) \right\} e^{\frac{i \sigma f M}{\beta_{compr}^2}} \quad (3.58)$$

with  $M = W_{QS}/a_\infty$  the effective Mach number,  $\beta_{compr}$  the Prandtl-Glauert compressibility factor and  $f$  a corrective factor defined by:

$$f(M) = (1 - \beta_{compr}) \ln(M) + \beta_{compr} \ln(1 + \beta_{compr}) - \ln 2 \quad (3.59)$$

In Figure 3.13 we can see the Sears function in the complex plane and how it depends on the reduced frequency. The Sears function spirals around the origin, with the amplitude decreasing with increasing reduced frequency. For values of reduced frequency the phase shift  $\phi$  can be either positive or negative, therefore resulting in an anticipated or delayed blade response to the disturbance, compared with the quasi steady solution.

With the coefficient of the unsteady lift coefficient we can now compute the local unsteady lift:

$$\Delta c_l(\eta, \Psi) = \sum_{k=-\infty}^{\infty} \Delta c_{l,k}(\eta) e^{ik\Psi} \quad (3.60)$$

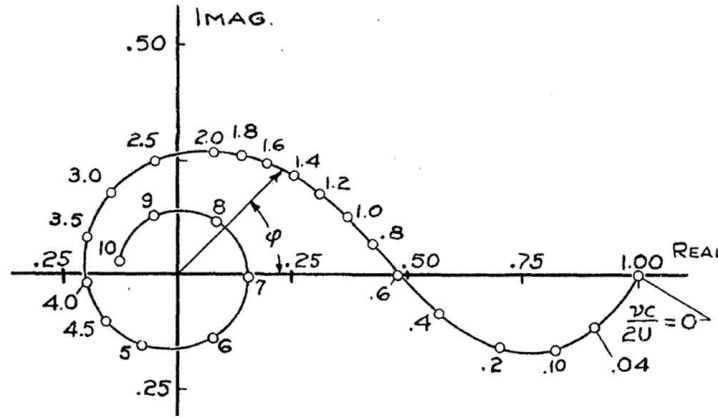


Figure 3.13: Vector diagram of the Sears function in the complex plane ([31])

### UNSTEADY PROPELLER LOAD

From this point, we can integrate the unsteady lift coefficient just obtained in two ways:

1. The final lift coefficient used is exactly the one evaluated by the Sears method, therefore:

$$c_{l,UNS}(\eta, \Psi) = \Delta c_l(\eta, \Psi) + \text{avg}(c_{l,QS}(\eta)) \quad (3.61)$$

It's necessary to add the mean value of the quasi steady periodic variation of the lift coefficient since the input distribution of  $\alpha_r$  used was obtained by subtracting its mean value.

2. A second approach that could be adopted is the one where from the unsteady lift coefficients obtained previously we derive only the "variational" part of it, basically only taking into account the value of the Sears function:

$$\Delta c'_l(\eta, \Psi) = \Delta c_l(\eta, \Psi) - 2\pi\alpha_r(\eta, \Psi) \quad (3.62)$$

thus, the final lift coefficient is obtained by adding this "variational" component to the quasi steady lift coefficient:

$$c_{l,UNS}(\eta, \Psi) = \Delta c'_l(\eta, \Psi) + c_{l,QS}(\eta) \quad (3.63)$$

The differences between the two methods are shown later in the numerical results chapter. Whatever the method, the  $c_{l,UNS}$  distribution is now used in a third instance of the code *Prop1D*. The convergence part is

skipped and the new  $c_{l,UNS}$ , along with the previously obtained  $c_{d,QS}$  are imposed to find the new distribution of thrust, normal force and torque.

The unsteady thrust and torque that the blade experience in each azimuthal position are given by:

$$T_{\psi,UNS} = \sum_{k=2}^{TOT_{\eta}} \frac{1}{2} \left[ \left( \frac{r}{R} \right)_k - \left( \frac{r}{R} \right)_{k-1} \right] \frac{(dT/dr)_{k,UNS} + (dT/dr)_{k-1,UNS}}{B} R \quad (3.64)$$

$$Q_{\psi,UNS} = \sum_{k=2}^{TOT_{\eta}} \frac{1}{2} \left[ \left( \frac{r}{R} \right)_k - \left( \frac{r}{R} \right)_{k-1} \right] \frac{(dQ/dr)_{k,UNS} + (dQ/dr)_{k-1,UNS}}{B} R \quad (3.65)$$

Therefore we can now obtain the quantities for each blade by

$$T_{B,UNS} = \frac{\sum_{i=1}^{TOT_{\psi}} T_{\psi,UNS}}{TOT_{\psi}} \quad (3.66)$$

$$Q_{B,UNS} = \frac{\sum_{i=1}^{TOT_{\psi}} Q_{\psi,UNS}}{TOT_{\psi}} \quad (3.67)$$

And finally the total quantities, by multiplying for the number of blades

$$T_{TOT,UNS} = T_{B,UNS} \cdot B \quad (3.68)$$

$$Q_{TOT,UNS} = Q_{B,UNS} \cdot B \quad (3.69)$$

At last, the performance coefficients are evaluated as follow

$$C_{T,UNS} = \frac{T_{TOT,UNS}}{\rho n^2 D^4} \quad (3.70)$$

$$C_{Q,UNS} = \frac{Q_{TOT,UNS}}{\rho n^2 D^5} \quad (3.71)$$

$$C_{P,UNS} = \frac{P_{TOT,UNS}}{\rho n^3 D^5} \quad (3.72)$$

$$\eta_{UNS} = \frac{C_{T,UNS} J}{C_{P,UNS}} \quad (3.73)$$



# 4

## EXPERIMENTAL SETUP

The following Chapter discusses the characteristics of the experimental approach used in this study. An overview of the experimental campaign is presented in Section 4.1. The Wind Tunnel Facility is described in Section 4.2, while in Section 4.3 the models used for the experiments are presented. Different measurement techniques have been used to obtain useful data, and these techniques are shown in Section 4.4. Finally the test parameters and variables are discussed in Section 4.5.

### 4.1. TEST CAMPAIGN OVERVIEW

The experimental setup presented in this chapter was part of an experimental campaign aimed to study the interactions between propellers. In Figure 4.1 an overview of the main elements of the test campaign is presented.

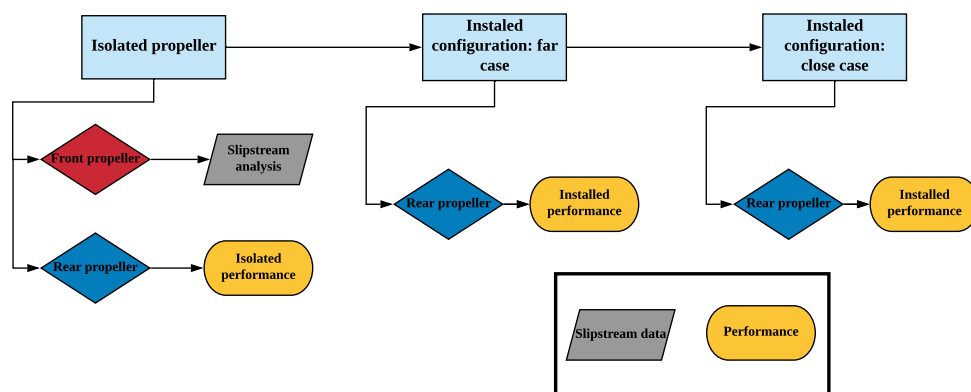


Figure 4.1: Overview of the main elements of the wind tunnel test campaign

The configuration presented here is made by a front propeller in a pusher configuration, whose slipstream impinges the rear propeller. At first, the rear propeller in isolated configuration was the subject of preliminary measurements. The performance were measured by using an internal Static 6-component balance. Subsequently the front propeller slipstream velocity field was studied. Finally, both propellers are put together in the test section and the effects of the interaction on the rear propeller were measured. Two different distances between the propellers were studied, a "close" case and a "far" case, corresponding to  $d_x = 0.6$  and  $d_x = 5.5$  (geometry schematized in Figure 2.8).

The isolated propeller measurements served not only as a reference model in order to compare the interaction effect with an isolated configuration, but also to test the effectiveness of the sensor used. A large range of rotational speeds were considered.

The measurements of the slipstream field was performed by using a total pressure probe. The purpose of these measurements is not only to understand the magnitude of the velocity in the slipstream that impinges the rear propeller, but also, since the front propeller is in a pusher configuration and its inflow is disturbed by the presence of the structural pylon, covered with an airfoil shaped fairing, it is useful to understand the effects on the generation of the slipstream. The slipstream analysis was made by moving the probe behind the propeller and

taking the measurements at each step of the sweep.

Finally, both propellers have been mounted and operated together. In both cases, "far" and "close", the rear propeller loads were measured for a set of  $d_y$  values, in order to understand how the level of overlap affects the results. For each  $d_y$  value, the front propeller was set at a fixed rotational speed (therefore a fixed load) while, for the rear one, an appropriate range of rotational speed was chosen.

## 4.2. WIND TUNNEL FACILITY

The experiments were performed in Delft University of Technology's Open Jet Facility (OJF). OJF is a closed circuit wind tunnel with an open test section and an equivalent exit jet diameter of 3.1 m with a maximum wind velocity of 30 m/s. The available test section is 6.0 m wide, an height of 6.5 m and a length of 13.5 m. In order to provide a flow as much laminar as possible and to reduce the flow's turbulence level, the settling chamber is equipped with a honeycomb rectifier grid and five screens. This results in velocity deviations smaller than 0.5% in the vertical plane at two meters from the outlet, with a longitudinal turbulence intensity level lower than 0.24%. The entire tunnel is covered with perforated plates installed on mineral wood and sound absorbing foam, in order to reduce noise levels. In Figure 4.2 a cutaway drawing of the OJF is depicted.

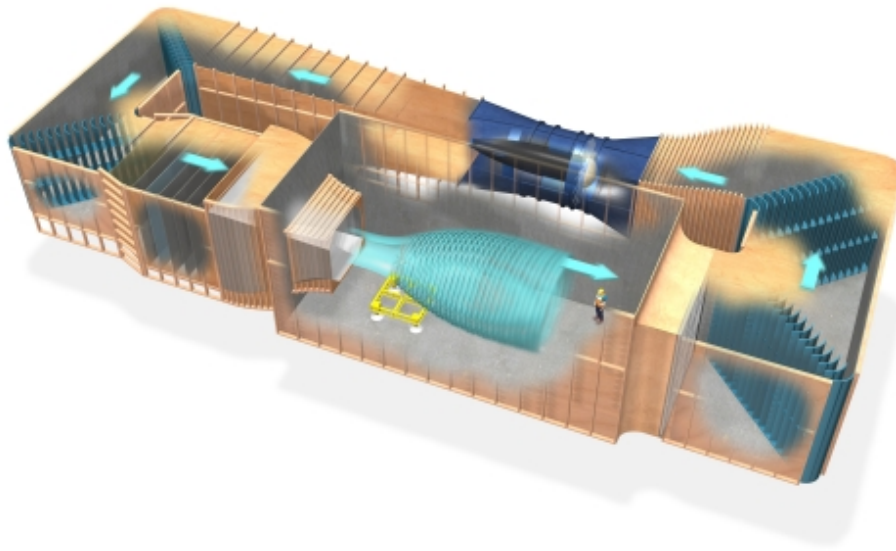


Figure 4.2: A representation of the circuit of the Delft University of Technology's Open Jet Facility (OJF). From [34]

## 4.3. WIND TUNNEL MODELS

The experimental setup for the interaction study involved two propellers supported on two pylons, both fixed on two horizontal beams mounted on the testing table. The position of the rear propeller was determined by fixing the beams on the test table, while the  $d_y$ , defined as the lateral separation of the two propellers' axis, can be chosen by sliding the model over the two beams. In Figures 4.4 and 4.5 the two configurations are depicted, respectively for the far and close case.

The propeller used on both models was made by Fokker during the development of the conceptual Fokker F-29. The model have a diameter of 0.304 m and are equipped with four blades, that can be removed independently. The blade angle at 70% of the blade span is set to  $20^\circ$  for both propellers, in order to achieve the same desired thrust in isolated configuration. In Figure 4.3 the chord and blade pitch angle distribution for the F29 propeller blade used in the experimental test and numerical analysis are presented.

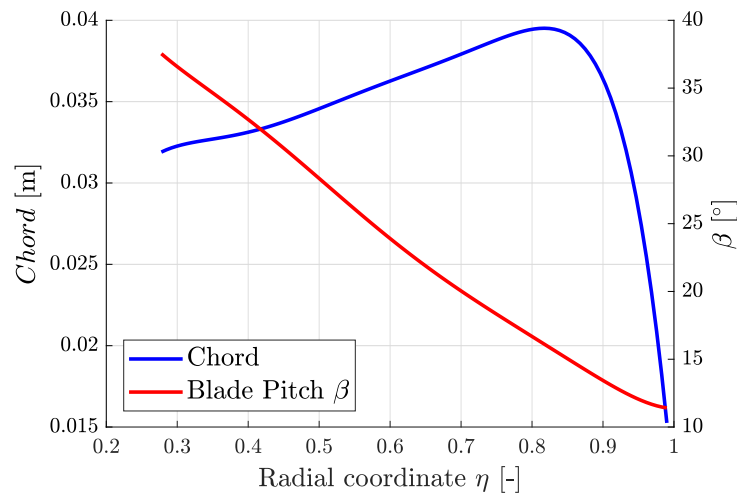


Figure 4.3: Blade pitch angle  $\beta$  and chord distribution for the F29 propeller blade.

The front propeller is in a pusher configuration, and this means that the nacelle is upstream and the whole structure is being pushed by the propeller. The propeller is driven by a Lehner LMT 3080, an electric motor powered by a TDK-Lambda Genesys power supply which has a rated power of 5kW. The motor is controlled by the electronic speed controller MGM HBC series TMM 25063. Through a custom Labview control software the DC voltage of the power supply can be controlled, converted into a 3 phase alternating voltage seen by the motor, in order to select the desired rps. The software is characterized by a closed loop control on the rps value, in order to adjust properly the input voltage and avoid undesired fluctuations of the voltage itself. It is also possible to control the direction of the rotation, and this propeller, as the rear one, are right-handed propellers (anti-clockwise direction).

The pusher configuration is chosen so that the slipstream shed by the propeller is as much undisturbed as possible, however the front propeller inflow itself is disturbed not only by the presence of the nacelle, where the electric motor is stored, but also by the supporting pylon. An airfoil shaped frame is installed on the pylon to reduce the impact of the body. The airfoil used is a NACA 65<sub>4</sub> - 021, which has a large maximum thickness located at the correct chordwise location for the pylon, and the leading edge close to the front of the nacelle to prevent horseshoe vortex.

The back spinner of the model was chosen after a topological study aimed to obtain the lowest drag possible. The reference geometry is a Myring Cubic (ESDU 77028 afterbody 9) with variable  $L/D$  and  $\tau_0$ , which have been selected equal to  $L/D = 1.625$  and  $\tau_0 = 10^\circ$ .

In the rear model, the propeller is mounted in front of the nacelle. The propeller is driven by the same type of motor as the front one, but it features a customized longer shaft, necessary to fit the sensor used to measure the forces and torques acting on the propeller. The sensor used is an ATI-IA Mini45 Titanium.

So, except for the sensor and the propeller mounted in a tractor configuration, the rear model has the same features of the front one.

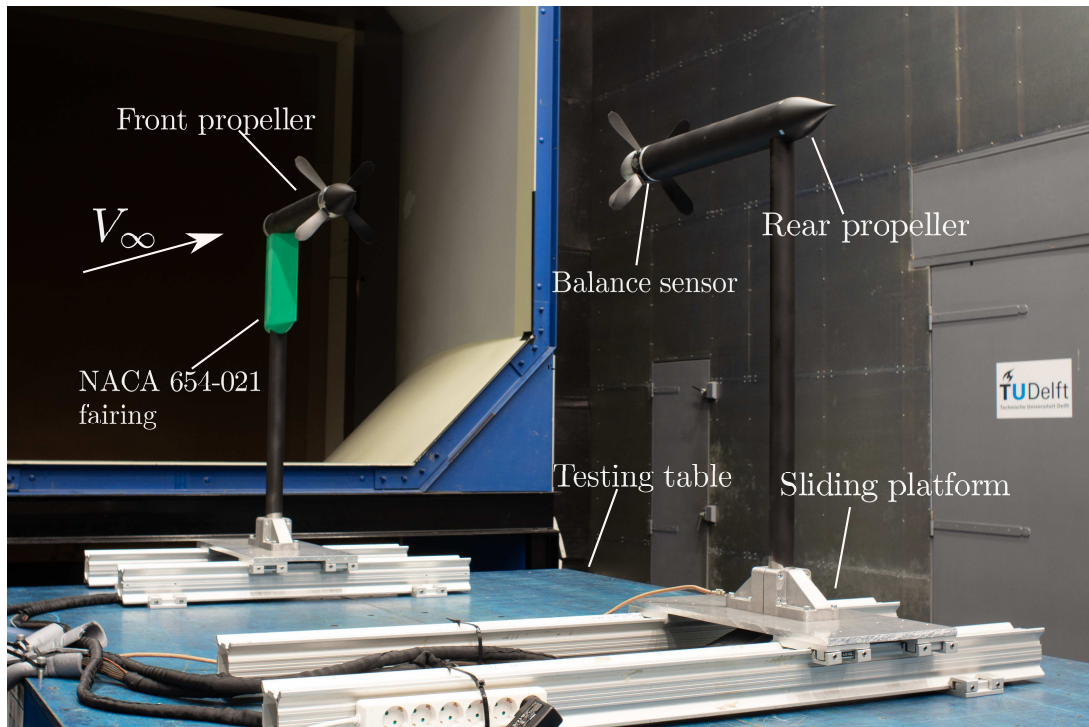


Figure 4.4: Photograph of the models in the far case configuration inside the OJF

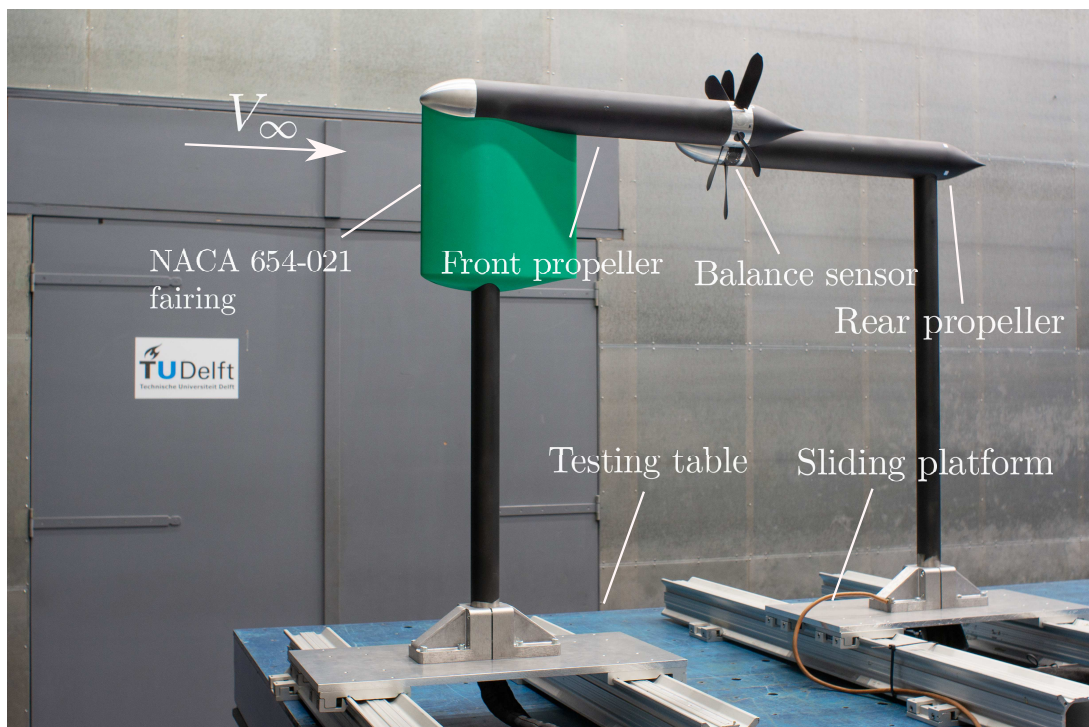


Figure 4.5: Photograph of the models in the close case configuration inside the OJF

## 4.4. MEASUREMENT TECHNIQUES

Several different measurement techniques were employed to obtain quantitative data from the wind tunnel experiments. The propeller performance, both for the isolated case and the interaction case, were measured using the balance sensor, described in Subsection 4.4.1. The wake of the front propeller was measured by using a total pressure probe, as described in Subsection 4.4.2.

### 4.4.1. PROPELLER PERFORMANCE MEASUREMENTS

The six-axis force and torque sensor ATI-IA Mini45 Titanium was used to measure the forces and moments acting on the propeller. Developed by the ATI Industrial Automation, the sensor is basically a short cylinder made of two parts. The front part is fixed to the nacelle and the rear part is fixed to the motor. In this way, all the forces and moments on the motors are measured through the shaft. In Figure 4.6 the balance used is depicted.



Figure 4.6: Photograph of the ATI-IA Mini45 Titanium balance sensor

A SI-240-12 calibration was performed by the manufacturer and in Table 4.1 and 4.2 the calibrated ranges of forces and torques are presented, along with the measurement uncertainty. The uncertainty is defined as the maximum amount of error for each axis expressed as a percentage of its full-scale load.

$F_x$	$F_y$	$F_z$	$T_x$	$T_y$	$T_z$
480 N	240 N	240 N	12 Nm	12 Nm	12 Nm

Table 4.1: Calibrated range for the balance used in the wind tunnel test.

$F_x$	$F_y$	$F_z$	$T_x$	$T_y$	$T_z$
1.75 %	1.75 %	1.75 %	1.75 %	1.75 %	1.75 %

Table 4.2: Maximum measurements uncertainty on each axis for the balance used in the wind tunnel test.

The measurement were performed at a sampling frequency of 10 kHz and a measurement time of ten seconds. Before each measurement, in order to obtain the actual response due to the propeller forces, it is necessary to subtract the offset present in the balance when the propeller is not rotating. The two 'zero measurements' are performed before the first useful measurements of the run and after the last one. The sensor returns analog output voltages from the six channels corresponding to the forces/moments on the propellers. The signal from the sensor is acquired by two 24 bit National Instruments acquisition cards. The actual forces and moments were computed using a calibration matrix, presented in Appendix B.

### 4.4.2. TOTAL PRESSURE MEASUREMENTS

The reason behind the measurement of the total pressure in the front propeller slipstream is threefold. At first, since the front propeller was not equipped with a balance sensor, it was necessary to verify that its thrust, for the

same rps and inflow condition, was equal to the rear one. Secondly, an investigation of how the body (airfoil-shaped frame) affects the overall behaviour of the slipstream was necessary. Finally, these measurements are important to verify the velocity distribution inside the slipstream. To perform the measurement, the probe was mounted on a thin pylon, attached to a traversing system.

The pitot probe was connected to a Mensor DPG 2400 pressure sensor. Its range of measurements is between -1000 and 3500 Pa, with an accuracy of 0.03%. A photograph in Figure 4.7 depicts the setup used in the wind tunnel testing to measure the total pressure right behind the front propeller.

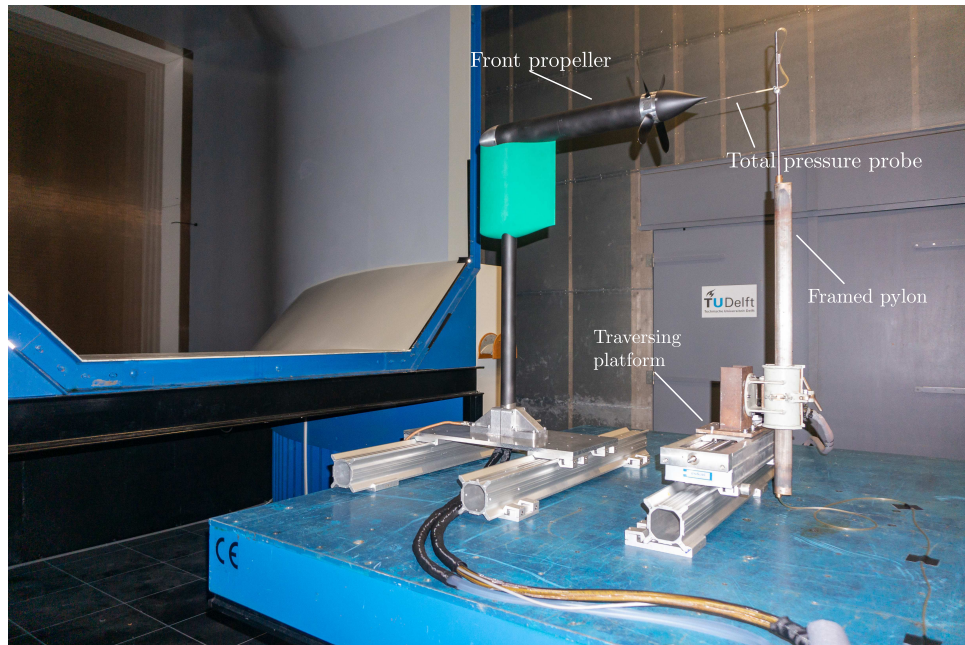


Figure 4.7: Photograph of the setup adopted to measure the total pressure of the front propeller slipstream

#### 4.5. TEST CONDITIONS AND PARAMETERS

Several different parameters define the operating conditions of this experimental setup. A part from the atmospheric conditions, defined by atmospheric pressure  $p_\infty$  and density  $\rho_\infty$ , the user can control directly other conditions such as the freestream velocity  $V_\infty$ , the rotational speed of both propellers  $n_f$  and  $n_r$  and the axial and lateral separation between the propeller, namely defined as  $d_x$  and  $d_y$ .

The aim of the entire work is to understand the effects of a propeller slipstream ingestion by another propeller, in a cruise configuration. Therefore, a freestream velocity of  $V_\infty = 20$  m/s, which was the best trade-off between an high freestream velocity and a stable behaviour of the wind tunnel. Moreover, for values of freestream velocity of 25 m/s and more, the thrust developed by the propeller was quite a bit lower. Since this campaign aimed to be representative of a cruise condition, both models were set with an angle of attack  $\alpha_p$  equal to 0 degrees. Since the freestream velocity has been fixed, and since both propellers have the diameter, the variation in rotational speed can be represented by the variation of advance ratio, since it is a more effective way to represent the propeller load. The other two factors are the lateral and axial separation. The values of these parameters were chosen based on the following criteria:

- Advance ratio: In order to understand the effect of the front propeller load on the interaction effects, two values of advance ratio were chosen, one representative of a moderately high loading,  $J = 0.49$ , corresponding to a rotational speed  $n_f$  of 135 rps, and a slightly higher advance ratio but still relevant in terms of thrust, equal to  $J = 0.57$ , corresponding to  $n_f=115$  rps.

Chosen these values for the front propeller, it is necessary to define the range of advance ratio for the rear propeller. For the isolated configuration, a broad range was chosen, between  $J = 0.4$  and  $J = 0.77$ . However, since in the slipstream the induced axial velocity component can be of the order of the freestream velocity, it is necessary to choose the range of advance ratio so that the rear propeller was still in a positive torque situation. Therefore, the range is different for each value of lateral separation, because it determine how much the propeller is affected by the accelerated inflow. Anyhow, the minimum value of advance ratio is the same for each  $d_y$  selected and equal to  $J = 0.4$ .

- Axial separation  $d_x$ : To understand how the distance between the two propeller disks influences the effects of the interaction, two value of axial separation have been chosen. By looking at the most common early concepts of eVTOL vehicles, as the ones presented in the Chapter 1, it is possible to notice how the general distance between the front and rear rows of propellers is in the order of 4-6 propeller radius. The representative value of  $d_y$  chosen to study this configuration is  $d_x = 5.5$  propeller radius. on the other hand, the other  $d_x$  value was chosen to be representative of a "close" overlap situation, therefore an axial separation of 0.6 propeller radius was selected.
- Lateral separation  $d_y$ : For the far case, a broad range of  $d_y$  values was chosen. In fact, by controlling the lateral separation we can appreciate how the overlapping area influences the effects of the impingement. Therefore, the range of lateral separation for the far case varies between  $d_y = 0$  and  $d_y = 3$ . In the close case, since the two propellers are very close to each other, it was not possible to go through the whole range adopted in the previous case. So, a more limited range was chosen, between  $d_y = 1.28$  and  $d_y = 3$ , and a further  $d_y$  position was added, equal to  $d_y = 1.75$ .

The operating condition discussed are summarized in Table 4.3.

<b>Variables</b>	<b>Values far case</b>	<b>Values close case</b>
Freestream velocity $V_\infty$ [m/s]	[20]	[20]
Advance ratio front propeller $J_f$	[0.49, 0.57]	[0.49, 0.57]
Advance ratio rear propeller $J_r$	[0.4 - depends on $d_y$ ]	[0.4, depends on $d_y$ ]
Rotational speed front propeller $n_f$	[135, 115]	[135, 115]
Rotational speed rear propeller $n_r$	[165 - depends on $d_y$ ]	[165, depends on $d_y$ ]
Axial separation $d_x$	[5.5]	[0.6]
Lateral separation $d_y$	[0, 0.25, 0.375, 0.5, 0.625, 0.75, 0.875, 1, 1.25, 1.5, 2, 3]	[1.28, 1.5, 1.75, 2, 3]

Table 4.3: Overview of the test conditions



# III

## RESULTS



# 5

## NUMERICAL RESULTS

In this chapter the results from the numerical studies of the isolated propeller are presented. In Section 5.1 the operating condition and an overview of the analysis is shown. The performances of the front propeller are discussed in Section 5.2, and in Section 5.3 the slipstream model results are shown. Thereafter, the results obtained for the rear propeller are treated in Section 5.4, in which the effects of the slipstream impingement are discussed.

### 5.1. ANALYSIS OVERVIEW

Using the methodology described in Chapter 3, the performance of both propellers is computed. The geometry used for the propeller is the same as for the wind tunnel testing, described in Chapter 4. The front propeller rotational speed used are 115 and 135 rps, and the freestream velocity used is 20 m/s.

At first, the 2D analysis of the blade sectional airfoil is performed by using RFOIL, with the rotational effects enabled. For each section two polars are obtained, so that the program is able to interpolate in order to get the correct lift and drag coefficients. Once the database is obtained, the first instance of Prop1D evaluates the solution of the front propeller, in terms of performance and components of the induced velocity in the slipstream. The slipstream model is now used to compute the contraction and the evolution of axial and tangential components of the induced velocity. The outputs of the model are stored and can be used as an input for the second instance of Prop1D, relative to the rear propeller.

All the setup parameters are the same as in the experiments, therefore two main cases have been analyzed, one for  $d_x = 0.6$  and the other one for  $d_x = 5.5$ . For each condition, the relative range of  $d_y$  is studied. The solution of the propeller loading is done by performing at first a quasi-steady analysis, from which we obtain the periodic distribution of angle of attack that each blade sections sees through the revolution, followed by an unsteady analysis using the Sears method. The lift coefficient distribution obtained by the unsteady analysis is then used to derive the performance of the rear propeller, and the effects of the interaction are shown.

### 5.2. ISOLATED PROPELLER PERFORMANCE

The front propeller solution is performed by assuming that it can be considered as in an isolated configuration. The performance of the propeller in terms of  $C_T$ ,  $C_P$  and efficiency  $\eta$  is shown in Figure 5.1. The range of advance ratio used is the same as the one used during the experimental testing at the OJF, from  $J = 0.398$  to  $J = 0.772$ , with an inflow velocity of 20 m/s. The 2D aerodynamic data supplied to the program are obtained with the methodology described in Subsection 3.1.1, with a value of  $N = 4$  and free transition on suction and pressure side.

The results proposed in this Section, other than being representative of the front propeller, are also relative to the isolated reference case used to estimate the effects of the interference in the following parts of this Chapter. We can see that the behaviour of the thrust coefficient is almost linear for the whole range of advance ratios. By looking at the radial angle of attack for different  $J$  in Figure 5.2a, we can see how, decreasing the advance ratio, an increase in the overall distribution of  $\alpha$  is observed. The maximum value of  $\alpha$  is located at  $\eta$  between 0.4–0.5, however in the lift coefficient distribution the maximum lift is located slightly more inboard, as shown in 5.2b. Increasing the rotational speed, the averaged lift is of course higher and its maximum value shifts even more towards lower values of radial distance.

By looking at Figure 5.1, it can be observed how the power coefficient distribution is slightly less linear compared to the thrust coefficient, while by looking at the efficiency distribution its maximum value is around  $\eta = 0.75$ , for an advance ratio of  $J = 0.68$ .

In the  $c_l$  distribution (Figure 5.2b) it is possible to get an idea of how the load on the blade is distributed, even though the induced axial velocity distribution is even more representative. In Figure 5.3a we can appreciate how the maximum of its value shifts from  $\eta \approx 0.5$  for the highest  $J$ , to  $\eta = 0.6$  for the higher load studied. The tangential velocity distribution follows quite well the lift coefficient distribution, and also its maximum value slightly shifts toward the inboard sections of the blade, as can be seen in Figure 5.3b.

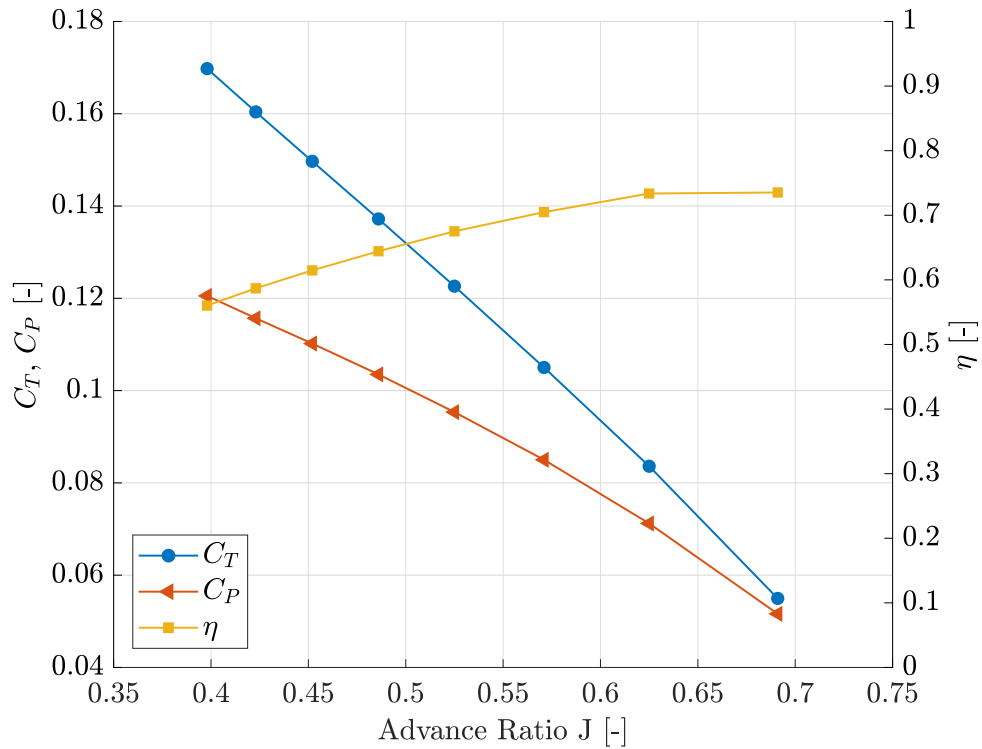


Figure 5.1: Isolated propeller performance:  $C_T$ ,  $C_P$  and efficiency  $\eta$  evaluated through the numerical code Prop1D. Freestream velocity  $V_\infty = 20$  m/s

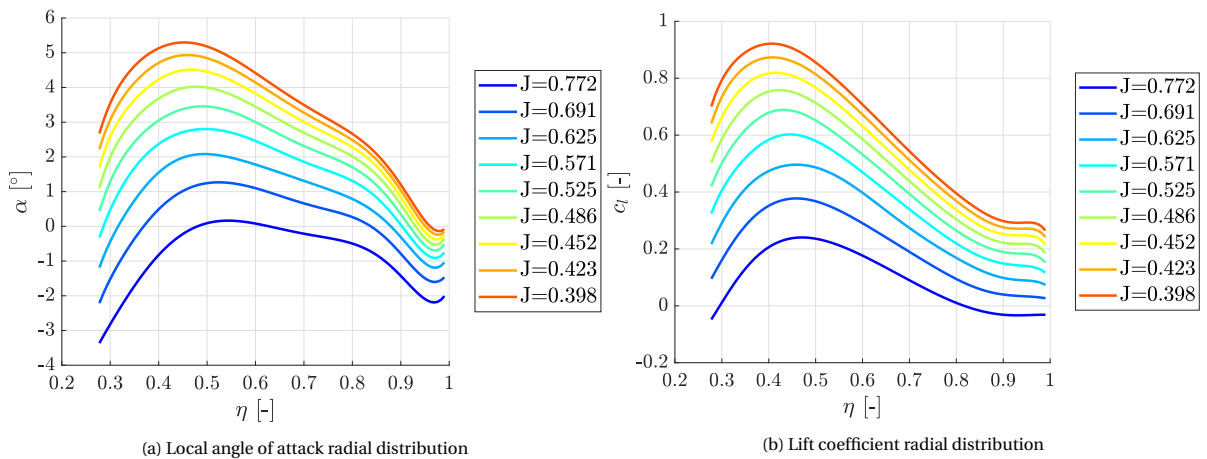


Figure 5.2: Local angle of attack  $\alpha$  and lift coefficient  $c_l$  radial distribution for  $V_\infty = 20$  m/s and  $J = [0.398 - 0.772]$

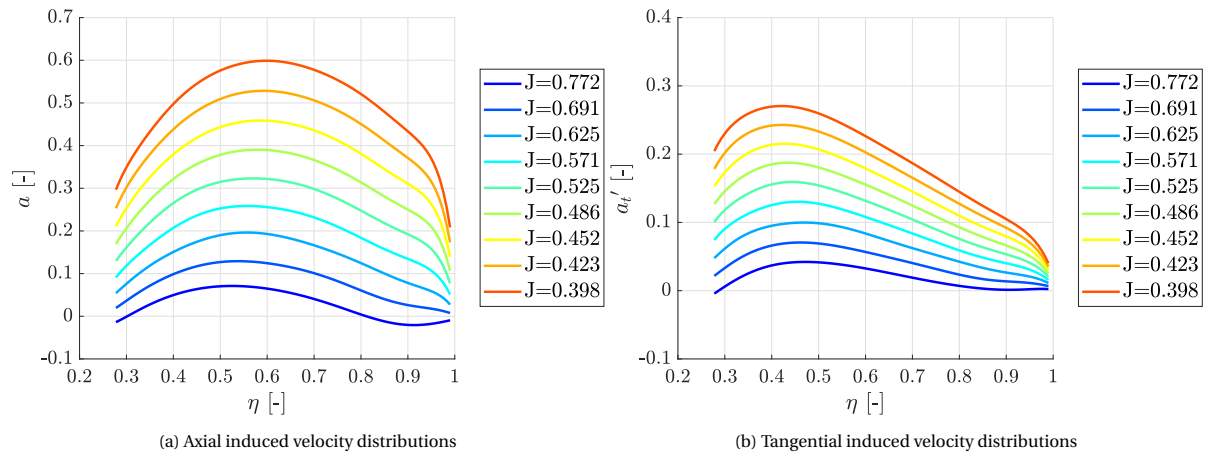


Figure 5.3: Axial and tangential velocity radial distribution for  $V_\infty = 20$  m/s and  $J = [0.398 - 0.772]$

### 5.3. SLIPSTREAM MODEL RESULTS

The analytical model of the slipstream is now applied for the two front propeller rotational speed values used in the experimental test. So, the results obtained from the front propeller analysis corresponding to the two values of rps, 115 and 135, are used. The values of rps correspond to advance ratios of, respectively,  $J = 0.57$  and  $J = 0.49$ . In particular, the axial and tangential induced velocity averaged distributions at the propeller disc are the input for the model, that is capable to obtain the restriction of the slipstream radius and the increase in tangential and axial component.

In this model, the slipstream is built as a 3D quasi cylindrical grid, as depicted in Figure 5.4. At any point downstream  $\zeta$  it is possible to know the induced velocity components distribution.

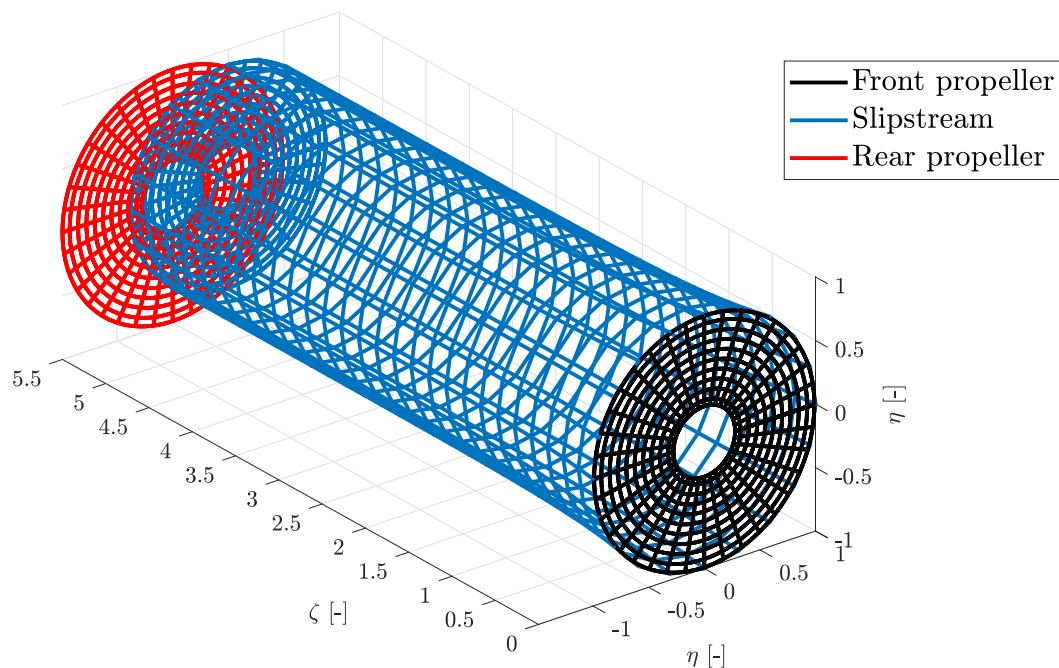


Figure 5.4: Numerical model of the slipstream grid

By looking at Figures 5.5a and 5.5b it is possible to appreciate the behaviour of the axial component of the velocity in the slipstream. The results are presented through the distributions of induced factors  $a$  and  $a_t'$ . We can see how the contraction and the magnitude of the velocity depends on two factors: the load of the propeller and the position downstream.

In the case of  $n_f = 115$  rps the contraction at  $d_x = 0.6$  is already equal to 3% of the propeller radius, and reaches

the 5% at  $d_x = 5.5$ . The maximum value of  $a$ , located at  $\eta \approx 0.55$ , from the close to the far case sees an increase of 30%. Looking now at the case of  $n_f = 135$  rps, the contraction is more important already for  $d_x = 0.6$ , equal to the 8% of the propeller radius, that goes up to the 13% for  $d_x = 5.5$ . However, even in this case the maximum value of  $a$  increases from  $\sim 0.6$  to  $\sim 0.78$ , meaning an increase of the 30%, close to the lower load case.

Therefore, it is possible to appreciate how the contraction is not negligible for both load levels and both axial distances. It should be noted, however, that the behaviour at the internal boundary of the slipstream is not well developed. Therefore, when the bilinear interpolation with the rear propeller grid, the internal region of the slipstream is filled with the computed velocity values found at the most inboard station, where a solution is present.

In Figures 5.6a and 5.6b the tangential component of the velocity in the slipstream is presented for the two  $d_x$  cases and the two  $n_f$ .

It is possible to appreciate how the change along the slipstream axis of the tangential velocity, for both cases, is almost negligible, except for the contraction effects, that slightly shifts the maximum value of the distribution.

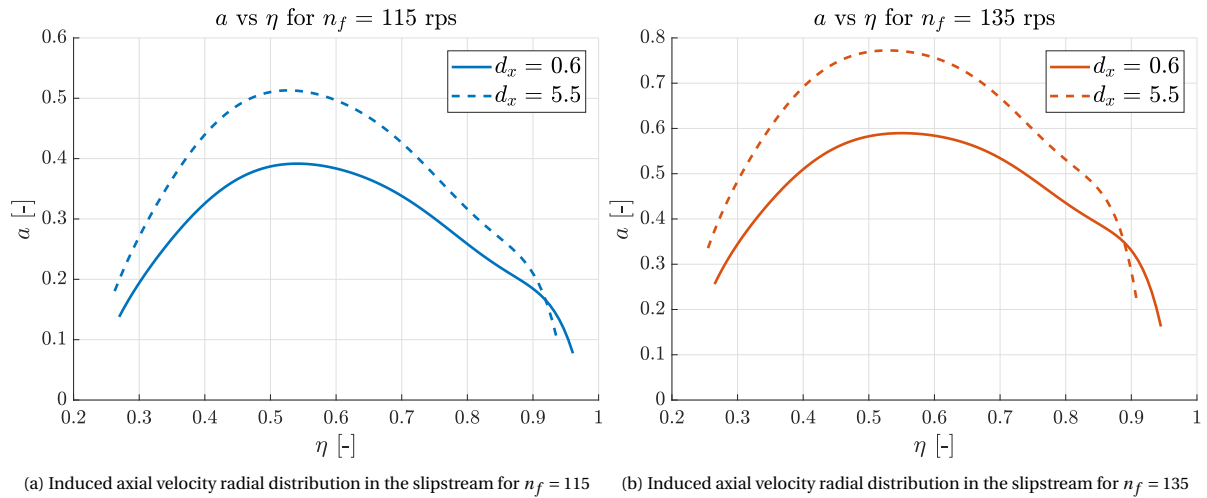


Figure 5.5: Induced axial velocity radial distribution in the slipstream for  $n_f = 115$  and  $n_f = 135$  and  $V_\infty = 20$  m/s

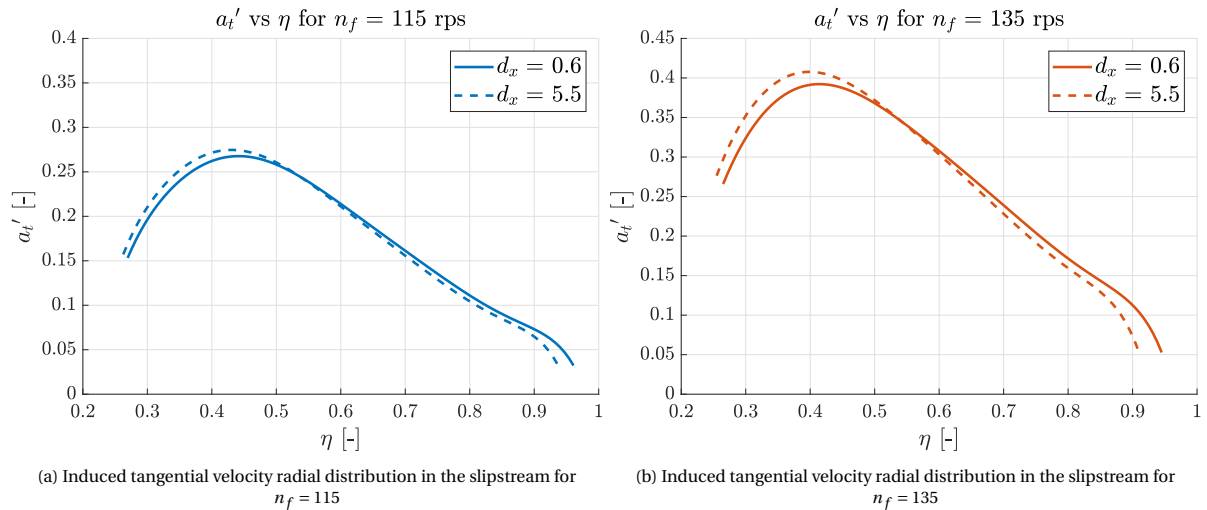


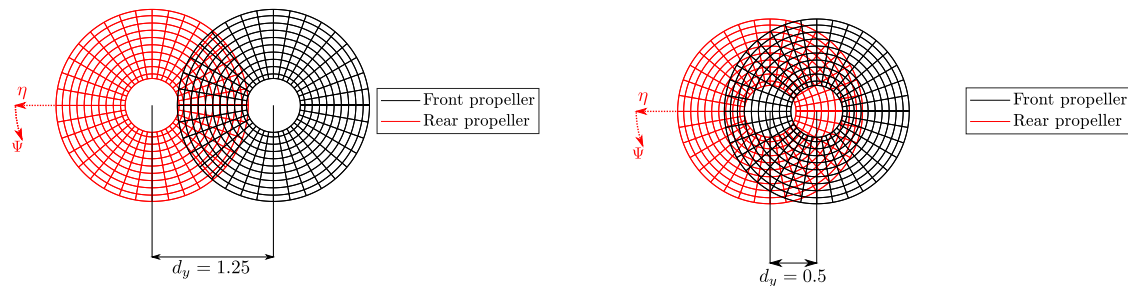
Figure 5.6: Induced tangential velocity radial distribution in the slipstream for  $n_f = 115$  and  $n_f = 135$  and  $V_\infty = 20$  m/s

## 5.4. REAR PROPELLER PERFORMANCE: INTERACTION EFFECTS

### 5.4.1. PROPELLER INFLOW

The propeller inflow is determined by the superimposition of the slipstream velocity field over the rear propeller inflow. This Subsection focuses on the velocity inflow in terms of the slipstream axial and tangential velocity components. For simplicity the results presented here are relative to the far case ( $d_x = 5.5$ ) and

$n_f = n_r = 135$  rps, since the substantial results are similar. However, it is interesting to see the differences in what the blade sees for two lateral separations values,  $d_y = 1.25$  (Figure 5.7a) and  $d_y = 0.5$  (Figure 5.7b).



(a) Schematization of the overlap of the two propeller's grids, for  $d_y = 1.25$  (b) Schematization of the overlap of the two propeller's grids, for  $d_y = 0.5$

Figure 5.7: Front and rear propeller grid overlaps, for  $d_y = 1.25$  and  $d_y = 0.5$

#### INFLOW DISTRIBUTION FOR $d_y = 1.25$

In the first case, the lateral separation between the two propeller is  $d_y = 1.25$ . We can appreciate how the blade of the rear propeller, by looking at Figure 5.7a, does not go on the "right" side of the front propeller grid. In Figure 5.8 the polar distribution of  $v_{a,s}$  encountered by the rear propeller blade is presented, divided by the freestream velocity. The outboard part of the blade experiences the higher values of the slipstream axial velocity. However, for the higher values of  $\eta$  shown, it's possible to see a decrease in  $v_{a,s}$ , due to the fact that the tip of the rear propeller blade passes through the radial distribution of  $v_{a,s}$ . Therefore, in the central part, for  $\Psi = 180^\circ$ , its value, if we look at 5.5b, is almost half the values at  $\sim 160^\circ$  and  $\sim 200^\circ$ . Focusing the attention towards the inner part of the blade, the effects of the interference affects a smaller range of polar angles when compared to the outboard region. Combined to fact that the magnitude is higher in the outboard region, we can conclude that the outboard sections will experience increased effects of the interaction, in particular a decreased local  $\alpha_r$ .

Focusing the attention of the plot presented in Figure 5.8, it is possible to see how the tangential component of the inflow velocity affects the blade. It should be noticed that this value is defined as the tangential velocity component relative to the rear propeller polar coordinate system. Therefore, this means that a negative value contributes to the rotational speed seen by each section, increasing the local angle of attack, or rather it reduces the effects of the increased axial component due to  $v_{a,s}$ , in the sense that contributes positively to the in-plane component of the velocity seen by the blade section. However, since it is a component of the overall dynamic. Due to the different distribution over the slipstream radius of  $v_{t,s}$ , we can appreciate how the maximum value it is seen by a blade section at  $\eta = 0.7375$ . In Figure 5.8 for the same section, the  $v_{a,s}$  maximum value is slightly lower than its value as seen by the most outboard section.

#### INFLOW DISTRIBUTION FOR $d_y = 0.5$

In this case the distance between the two propeller axes is lower. Therefore, a larger part of the rear propeller disc is affected by the front propeller inflow. Looking at the  $v_{a,s}$  polar distribution, we can see how, in this case, the inboard section ( $\eta = 0.4003$ ) whole rotation is affected by the slipstream inflow. This means that its time averaged behaviour will be substantially different, compared to the isolated case. The more we go toward the tip of the blade, the smaller is the polar range of disturbance. It's possible to see, moreover, how in this model the inflow relative to the internal region of the slipstream is characterized by a constant value. The maximum values of  $v_{a,s}$  are similar to the previous case, but now almost every blade sections experiences that maximum, and for a much broader range. Looking at the  $v_{t,s}$  polar distribution, it should be notice how the situation is dramatically different from the previous case. The largest part of the blade now sees a positive slipstream tangential velocity. This means that the overall in-plane velocity experienced by the blade sections is reduced, therefore decreasing the local  $\alpha_r$ . We can then expect even more sectional losses.

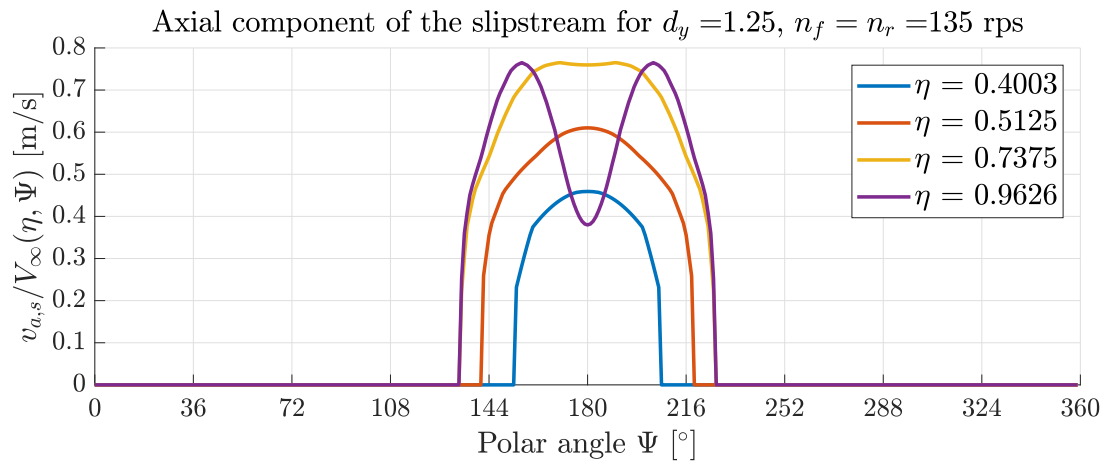


Figure 5.8: Propeller inflow: slipstream axial velocity distribution on the rear propeller at various radial station  $\eta$  for  $n_f = n_r = 135$  and  $d_y = 1.25$ ,  $V_\infty = 20$  m/s

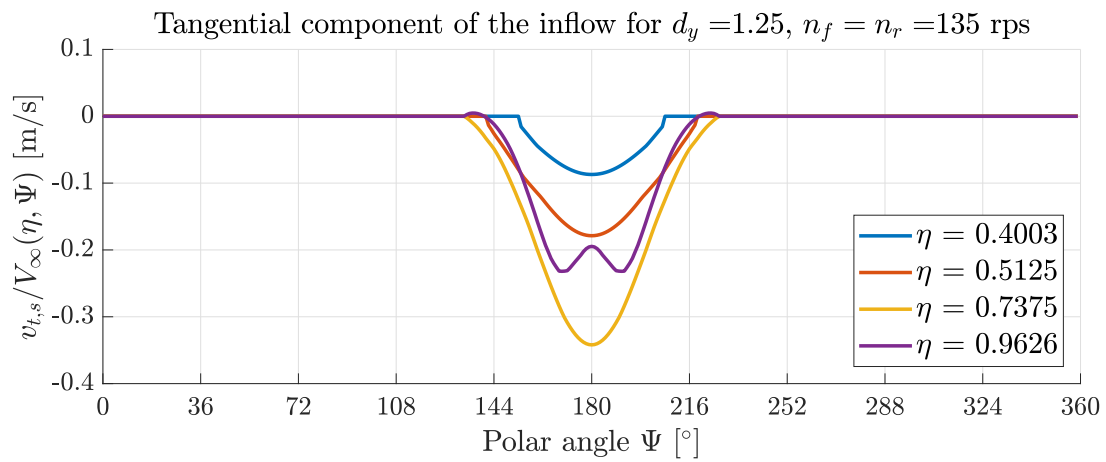


Figure 5.9: Propeller inflow: slipstream tangential velocity distribution on the rear propeller at various radial station  $\eta$  for  $n_f = n_r = 135$  and  $d_y = 1.25$ ,  $V_\infty = 20$  m/s

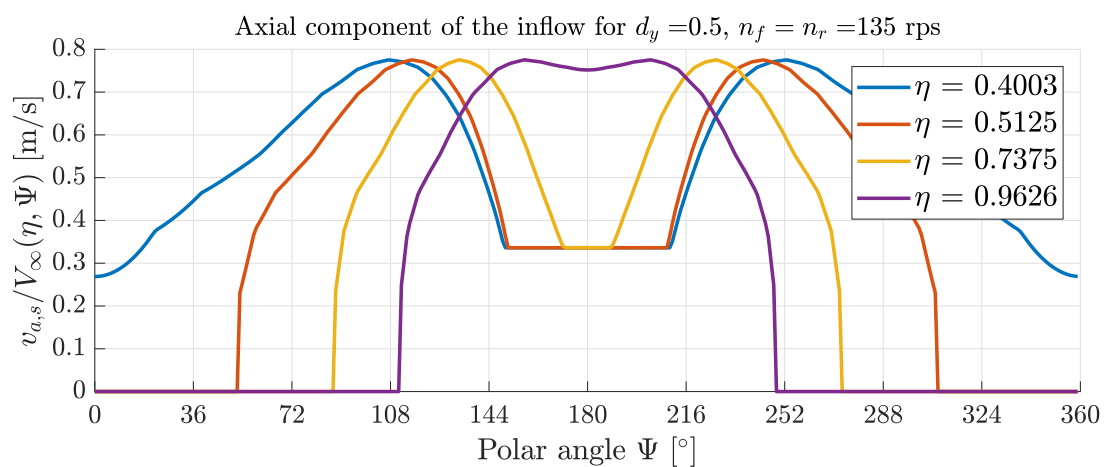


Figure 5.10: Propeller inflow: slipstream axial velocity distribution on the rear propeller at various radial station  $\eta$  for  $n_f = n_r = 135$  and  $d_y = 0.5$ ,  $V_\infty = 20$  m/s

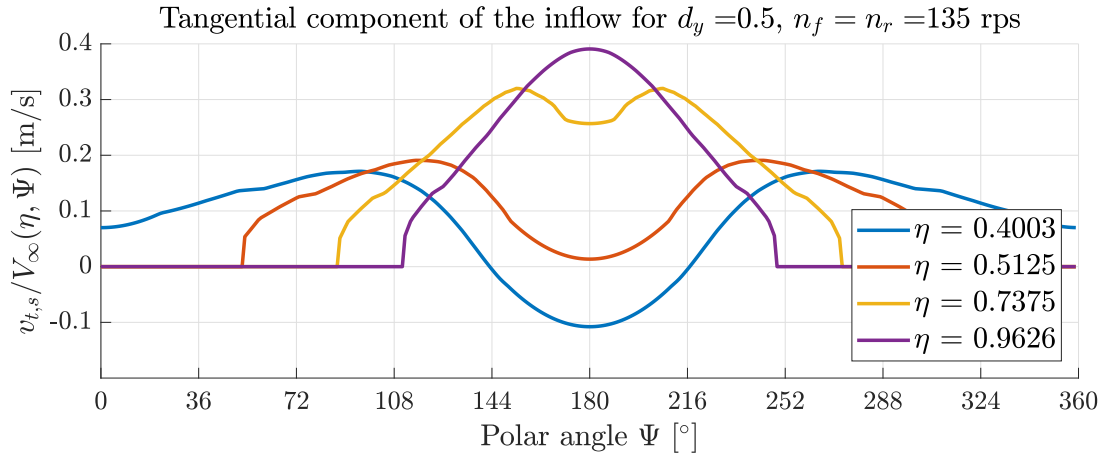


Figure 5.11: Propeller inflow: slipstream tangential velocity distribution on the rear propeller at various radial station  $\eta$  for  $n_f = n_r = 135$  and  $d_y = 0.5$ ,  $V_\infty = 20$  m/s

#### 5.4.2. COMPARISON BETWEEN QUASI STEADY AND UNSTEADY RESULTS

Proceeding further with the analysis, we are now able to solve the propeller loading distribution by using a two steps procedure: a preliminary quasi-steady solution, done inside Prop1D, and the unsteady analysis of the propeller computed by using the Sears' theory. In this Subsection, as in the previous, only the results corresponding to the  $d_x = 5.5$  case are presented. Furthermore, in order to compare two relevant cases, the results for  $d_y = 0.5$  and  $d_y = 1.25$  are shown. Both propellers are set to have the same rotational speed, equal to  $n_f = n_r = 135$  rps. At first, the quasi steady computation is performed, and the results in terms of the local  $\alpha_r$  seen by the blade, for the two values of  $d_y$ , are shown in Figures 5.12 and 5.13. The  $\alpha_r$  values over the polar angle have been subtracted by the average made for each  $\eta$ . It is evident how the disturbed inflow causes the local angle of attack to drop quite dramatically if compared to its values in the undisturbed region. By comparing the  $\alpha_r$  variation over  $\Psi$  and the distribution of  $v_{a,s}$  (Figures 5.8 and 5.10 we can notice the strong relation between the two. In fact, the positive peaks of the inflow axial velocity correspond to negative valleys in the  $\alpha_r$  distribution, and vice versa. It should also be noticed how the program does not iterate over the rotation in order to "spread" the disturbance, but instead solves each  $\Psi$  section independently. This means that sudden drops in quantities are expected, not only in the  $\alpha_r$  but also in the local  $c_l$  or in the sectional  $dT/dr$ .

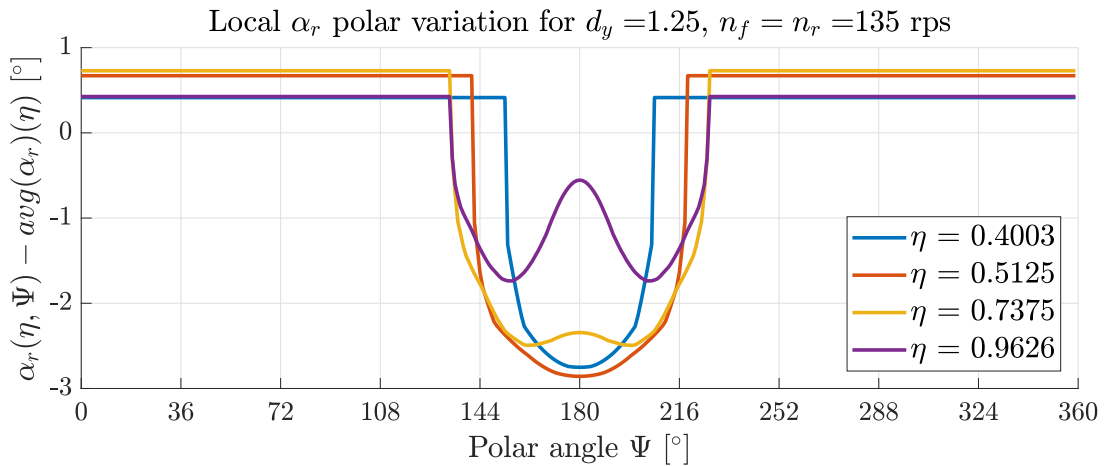


Figure 5.12: Propeller distribution: local  $\alpha_r$  distribution on the rear propeller at various radial station  $\eta$  for  $n_f = n_r = 135$  and  $d_y = 1.25$

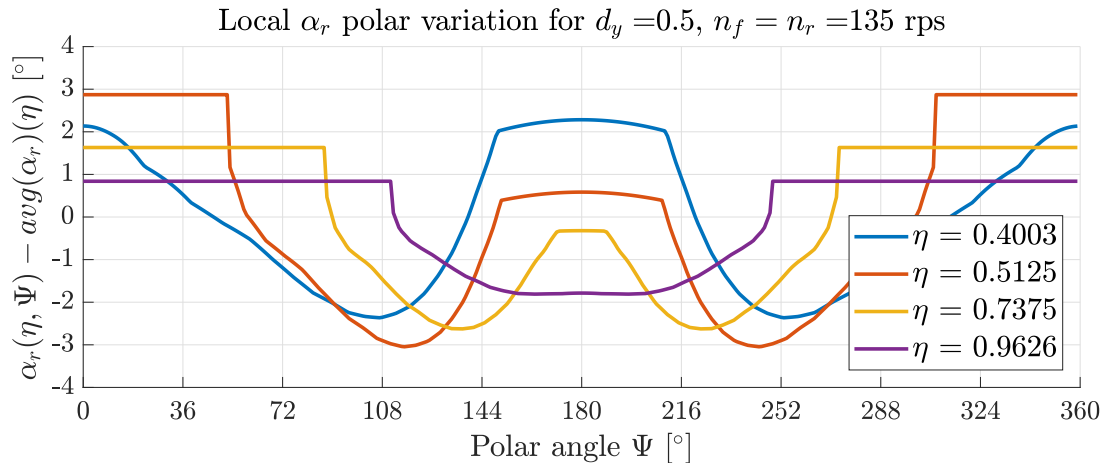


Figure 5.13: Propeller distribution: local  $\alpha_r$  distribution on the rear propeller at various radial station  $\eta$  for  $n_f = n_r = 135$  and  $d_y = 0.5$

Starting from the quasi-steady solution it is possible to proceed further with the unsteady analysis. The  $\alpha_r$  distribution, subtracted by its mean value for each station  $\eta$  is the main input for the Sears' analysis method. A comparison between the  $c_l$  provided by the quasi-steady solution and the two methods discussed in the numerical setup Chapter are presented in Figure 5.14. The case of  $n_f = n_r = 135$  rps and  $d_y = 0.5$  is shown, and the distribution relative to  $\eta = 0.7375$  is taken as an example. It is quite clear how the method, now, spreads the disturbance over the whole rotation. If the quasi-steady distribution of  $c_l$  follows closely the  $\alpha_r$  one, as expected, the unsteady lift is now anticipated, and the two negative peaks are less pronounced. It is possible to explain why the unsteady lift is anticipated by referring to the discussion regarding the Sears' function done in Subsection 3.3.2. The reduced frequency, for  $J = 0.49$ , a freestream velocity of  $20\text{ m/s}$  and a radial station of  $\eta = 0.7375$  is approximately  $0.17k$ , with  $k$  the harmonic order. With values of  $k$  of four and higher, the phase shift in the Sears function will be positive.

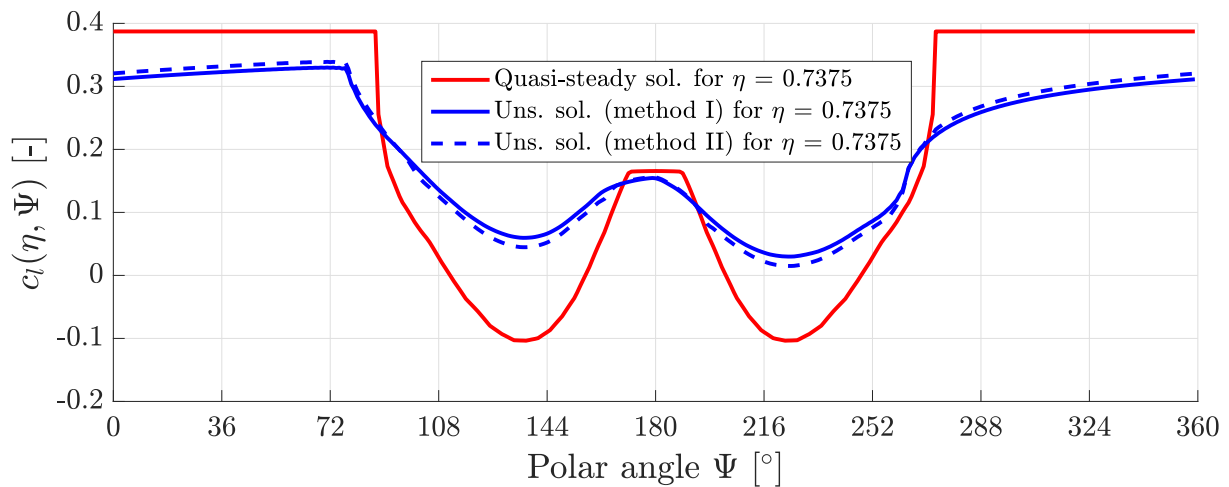


Figure 5.14: Comparison of the  $c_l$  distribution computed by the different methods, for a radial section  $\eta = 0.7375$ ,  $n_f = n_r = 135$  and  $d_y = 0.5$

If we now look at the difference between the two unsteady approaches, it is possible to notice that the 2nd method tends to be slightly closer, in terms of values, to the quasi steady solution, keeping, however, the same behaviour over the rotation of the 1st method. Due to this small difference, the 2nd method was chosen solely on the fact that the solution computed by the program is, in fact, more considered. As mentioned in Subsection 3.3.2, the 2nd method takes into account only the "variational" influence, i.e. the values of the Sears function over the rotation, and by adding them to the quasi steady distribution, the unsteady response of the blade is obtained.

It can be observed that even though the negative peaks magnitude is smaller for the unsteady lift, the fact that the blade response to the disturbance has an effect also in the undisturbed region, means that the time averaged values of the two solutions are quite close to each other, meaning that the overall propeller loading

solution computed by the unsteady method is probably similar to the quasi steady solution. However, this method is useful to have an idea of how the load is distributed over the propeller disc.

In Figures 5.15a and 5.15b the averaged distribution over the propeller disc of the lift coefficients are presented, for  $d_y = 0.5$  and  $n_f = n_r = 135$  rps, showing clearly how the two methods are different from each other. The unsteady  $c_l$  distribution is more smoothly scattered over the disk, and its distribution is not symmetric around  $\Psi = 180^\circ$  as it is in the quasi steady solution. In Appendix C further results regarding the disc loading distribution as evaluated in the program are presented.

As already mentioned, we are not expecting a big difference in the overall propeller solution. By looking at Table 6.1 it is to be observed how the thrust coefficients differs between the two solution by less than 1% of its value. On the other hand, the power coefficient from the unsteady analysis is less than 4% smaller if compared to the one from the quasi-steady solution, which can actually be considered as a relevant difference.

Variables	QS solution	UNS solution	(QS-UNS)/QS
$C_T$	0.0629	0.0626	0.0043
$C_P$	0.0531	0.0549	-0.0341

Table 5.1:  $C_T$  and  $C_P$  values computed from the quasi-steady and the unsteady solution, for  $d_y = 0.5$  and  $n_f = n_r = 135$ .

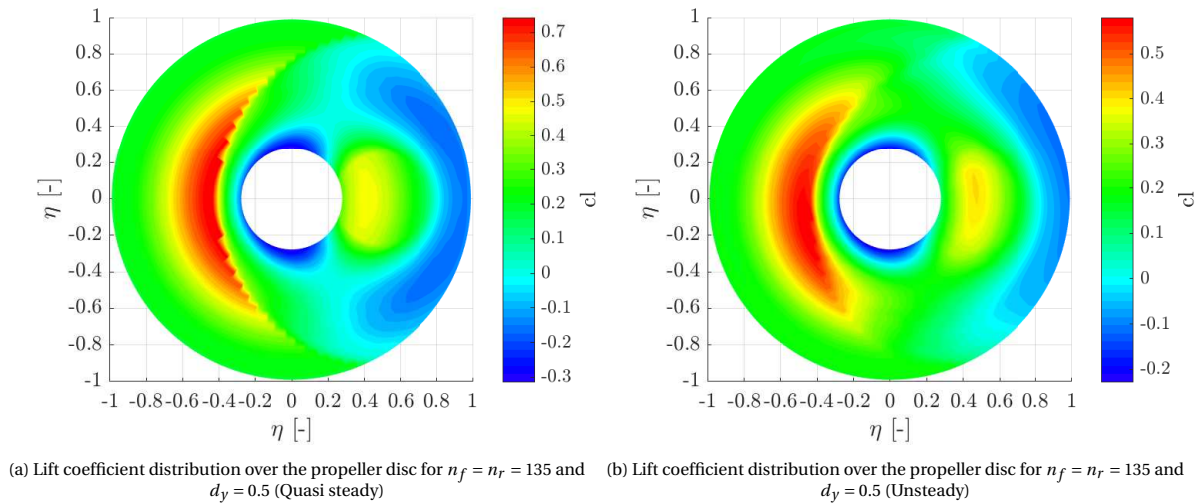


Figure 5.15: Lift coefficient distribution over the propeller disc as seen from the front (counter clockwise rotational direction), as computed by the quasi steady method and unsteady method for  $n_f = n_r = 135$  and  $d_y = 0.5$

### 5.4.3. EFFECTS OF THE INTERACTION ON THE PERFORMANCES

In this Subsections the effects on the  $C_T - J$  and  $C_P - J$  curves due to the effects of the interaction are presented. As expected from the preliminary discussion done in the previous Subsection, we are expecting the performance of the rear propeller to drop, in terms of thrust and power generated, with decreasing lateral separation between the two propeller axis  $d_y$ . Considering  $d_x = 5.5$ , in Figures 5.16a and 5.16b the interaction curves are presented in terms of  $C_T$  and  $C_P$ , in case of  $n_f = 135$  rps. At first it should be noticed how the highest value of  $J$  used for each  $d_y$  setting is different, and this is done because it was necessary to keep the thrust and torque of the propeller at an acceptable level in order to avoid windmilling.

Starting from the highest value of separation  $d_y = 3$  and  $d_y = 2$  we can notice how the rear propeller is unaffected by the front propeller slipstream. This is due to the fact that in this method the flow outside the slipstream tube is unaffected by the accelerated and swirled inflow inside, therefore the inflow of the rear propeller for those two is characterized by the freestream velocity  $V_\infty$  for the whole disc.

It can be observed how the decreases in the  $C_T$  and  $C_P$  values is not proportional within the whole range of  $d_y$ . In fact, starting from the value of  $d_y = 1$  it can be seen a much steeper gradient in how the propeller is affected by the interaction. One of the reasons of this behaviour can be explained by looking at how the slipstream tangential component is seen by the local section of the rear propeller's blade. As discussed in the previous Subsection, the  $v_{t,s}$  can be positive or negative, with respect to the rotational speed direction of the propeller's blade, therefore causing a decreased or increased contribution to the local  $\alpha_r$ .

It should be observed how, by looking at Figures 5.17a and 5.17b how, due to the lower rotational speed of the front propeller, the trend in both  $C_T$  and  $C_P$ , for the lowest  $J$ , is quite different from the previous case where  $n_f = 135$  rps. This can be explained by just looking at the slipstream axial and tangential velocity profile in Figures 5.5a and 5.6a. The magnitude of the velocity components in the slipstream is almost one third if compared to the 135 rps case, therefore a less dramatic effect on the rear propeller performance should be expected. It is interesting, however, to notice that in the case of equal rps between the front and the rear propeller, the trend of the various  $C_T$  curves is almost the same.

Focusing now the attention on the interaction curves for  $d_x = 0.6$  (Figures 5.16a, 5.16b, 5.17a and 5.17b), it can be observed the more restricted range of  $d_y$  used for this case. It can also be noticed how the loss in terms of thrust and power looks less pronounced. This can be explained by considering that for  $d_x = 0.6$  the slipstream contraction is not fully developed, therefore the velocity magnitude (especially for the axial component) is smaller if compared with the  $d_x = 5.5$  case.

It should be noticed that in this numerical model the rear propeller has no influence on the front propeller behaviour. If this assumption can be safely made for the case of  $d_x = 5.5$ , due to the large separation between the two propeller discs, in the close case the assumption is probably too strong. In fact, the slipstream tube generated in front of the rear propeller is characterized by an axial velocity component which is higher than the freestream velocity, therefore inducing a change in the local axial velocity seen by the front propeller blade, when passing through the interaction region.

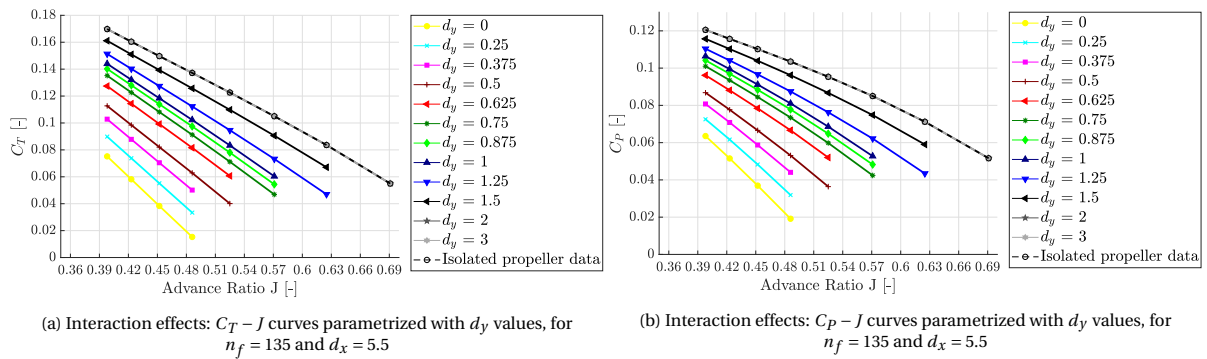


Figure 5.16: Interaction effects:  $C_T - J$  and  $C_P - J$  curves parametrized with  $d_y$  values, for  $n_f = 135$  and  $d_x = 5.5$  (Numerical results)

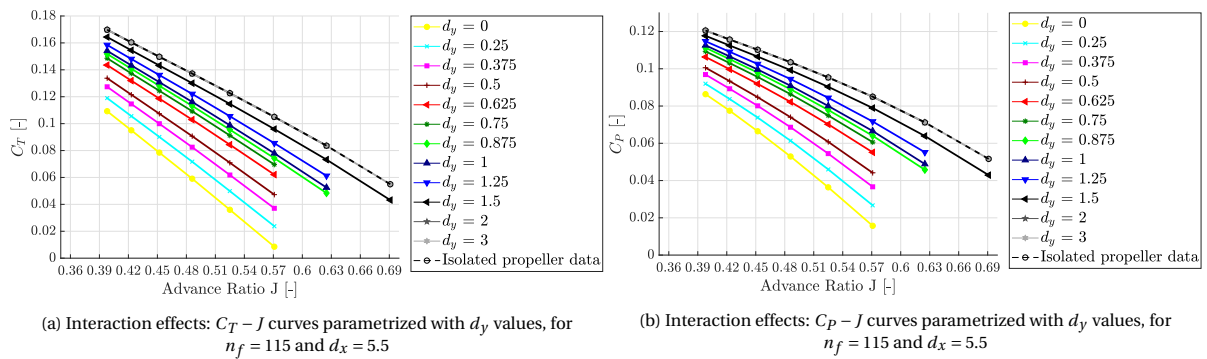


Figure 5.17: Interaction effects:  $C_T - J$  and  $C_P - J$  curves parametrized with  $d_y$  values, for  $n_f = 115$  and  $d_x = 5.5$  (Numerical results)

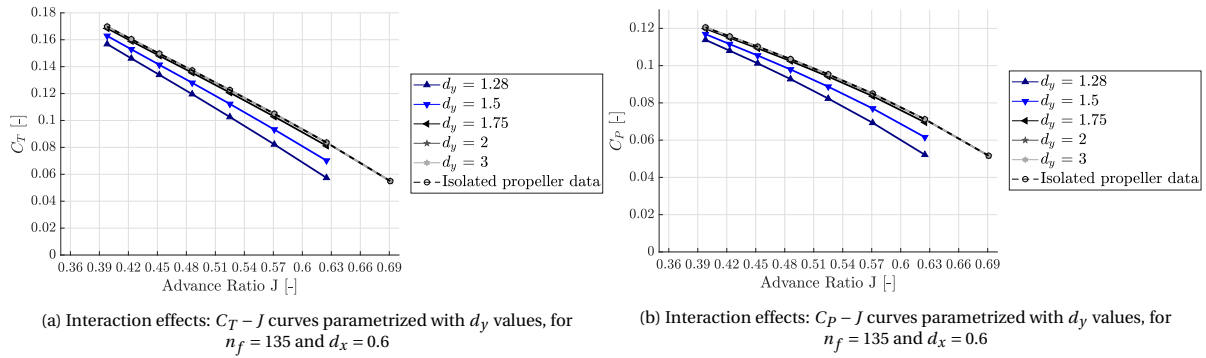


Figure 5.18: Interaction effects:  $C_T - J$  and  $C_P - J$  curves parametrized with  $d_y$  values, for  $n_f = 135$  and  $d_x = 0.6$  (Numerical results)

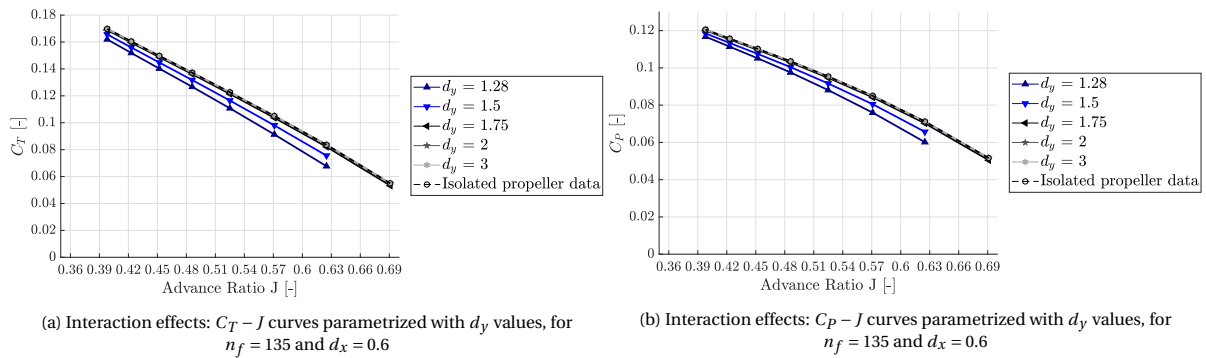


Figure 5.19: Interaction effects:  $C_T - J$  and  $C_P - J$  curves parametrized with  $d_y$  values, for  $n_f = 115$  and  $d_x = 0.6$  (Numerical results)

#### 5.4.4. EFFECT OF THE INTERACTION ON THE REAR PROPELLER THRUST

In this Subsection the attention will be focused mainly on how the thrust of the rear propeller is affected by the front propeller slipstream impingement. Considering the interaction plots presented in the previous Subsection, the change in  $C_T$  is now plotted vs. the range of  $d_y$  used. The change in  $C_T$  is expressed by the "loss factor"  $\Delta C_T$ , given by:

$$\Delta C_T = \frac{C_{T,iso} - C_{T,inst}}{C_{T,iso}} \quad (5.1)$$

With  $C_{T,iso}$  the thrust coefficient in the isolated configuration and  $C_{T,inst}$  the thrust coefficient of the rear propeller for the different  $d_y$  configurations. In Figures 5.20a and 5.20b the  $\Delta C_T$  variation are presented for the far and close case, for  $n_f = 135$  rps. The two curves shown in the Figures are relative to the maximum value of rps used for the rear propeller ( $n_r = 165$  rps, which correspond to  $J_r = 0.398$ ), and to the case where both propellers have the same rotational speeds. In the diagram relative to the the far case, it can be observed how the slope of the curve changes at the value of  $d_y = 0.75$ . In fact, starting by the case where the rear propeller is not influenced by the front slipstream, the rate of how much the rear propeller's thrust decreases increases drastically from  $d_y = 0.75$  on. This is true for both values of  $J_r$ . As already said in the previous Subsection, this can be explained by the fact that decreasing the lateral separation, not only a larger part of the propeller disc is affected by the impingement, but also the tangential component of the slipstream velocity field starts to act in the same direction of the blade rotation, therefore decreasing the local  $\alpha$ .

The curve relative to the equal rps case looks very similar to the maximum rps one, except that, starting from  $d_y = 1.5$ , the corresponding  $\Delta C_T$  values are increased by a factor which is inversely proportional to the increase in lateral separation. Therefore, it can be said that, given the same front propeller slipstream, how the rear propeller behaves through a range of  $d_y$  values depends on the rear propeller load distribution (which is equivalent to say that it depends on its rotational speed).

Looking now at the plot relative to the close case, it can be noticed how the effects, in terms of loss in thrust, are more modest if compared with the far case. Even if not directly comparable, it is possible to see how, for  $d_y = 1.25$  in the far case and  $d_y = 1.28$  in the close case, the loss of thrust is reduced for both values of  $J_r$ . The reason behind this, as already said previously, is the reduced axial velocity of the slipstream in  $d_x = 0.6$ . Similar conclusions can be drawn by looking at Figures 5.21a and 5.21b, relative to  $n_f = 115$  rps.

Moreover, by comparing Figures 5.20a and 5.21a it is possible to see how, when both propellers have the same rotational speed, the  $\Delta C_T$  behaviour is similar, leading to almost the same losses within the whole range of  $d_y$ . This can be explained by considering that the induced velocity field depends on the propeller load distribution, that, for a given freestream velocity and blade pitch, is related to the rotational speed. Therefore, if we keep the same rotational speed for both propellers, the induced velocity field from the front slipstream has a certain effect on the rear propeller, effect that in terms of decreased performance is the same for another level of rotational speed.

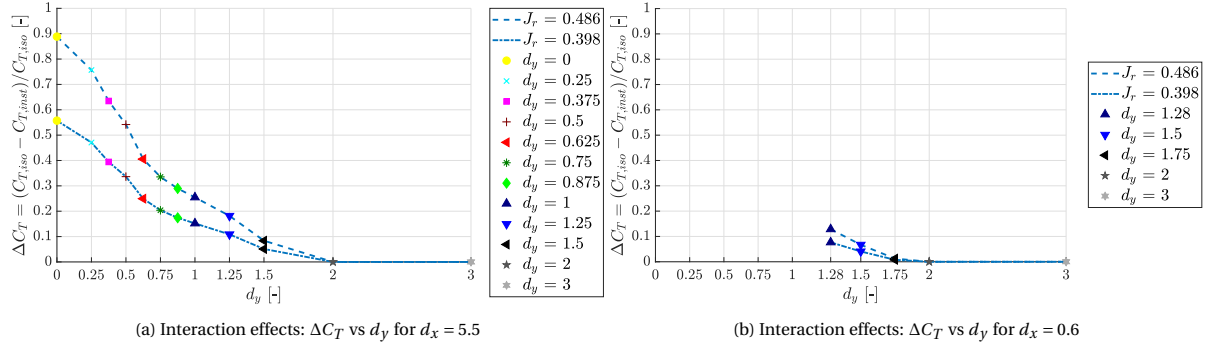


Figure 5.20: Interaction effects:  $\Delta C_T$  vs  $d_y$  for  $d_x = 5.5$  and  $d_x = 0.6$  parametrized with two values of advance ratio  $J_r$  and  $n_f = 135$  rps (Numerical results)

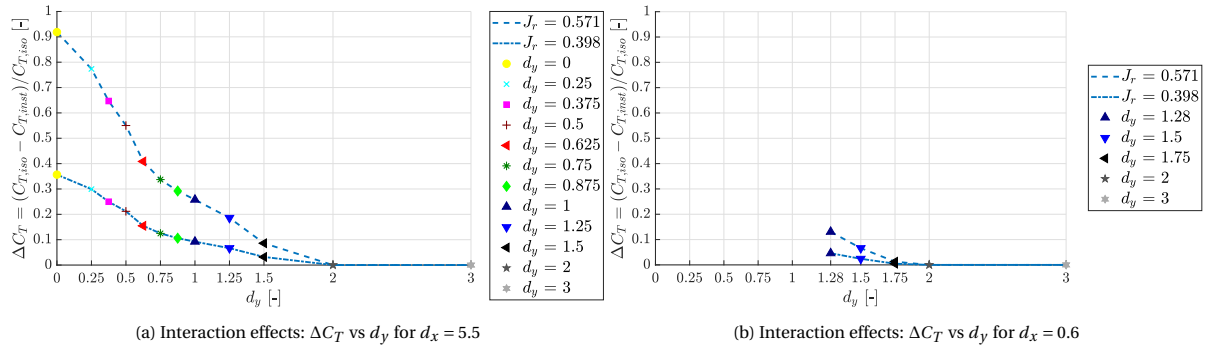


Figure 5.21: Interaction effects:  $\Delta C_T$  vs  $d_y$  for  $d_x = 5.5$  and  $d_x = 0.6$  parametrized with two values of advance ratio  $J_r$  and  $n_f = 115$  rps (Numerical results)

#### 5.4.5. INCREASED POWER REQUIREMENT TO RECOVER THE LOSS OF THRUST

We have seen in the previous Subsection the effects of the interaction considering constant values of rotational speed. But we saw that due to the interaction, the thrust can be heavily affected because of the increased velocity of the slipstream. Therefore, we can imagine a situation where it is required to keep the same thrust for both propellers. In order to do this it is necessary to recover the loss by increasing the rotational speed of the propeller, therefore consuming more power.

The analysis proposed here is focused on the configuration relative to  $d_x = 5.5$ . The first step of this analysis is to obtain the value of thrust that we want to keep constant. An alternative form of the thrust coefficient is used, named  $T_C$ , which is given by:

$$T_C = \frac{T}{\rho V_\infty^2 D^2} \quad (5.2)$$

For each case of  $n_f$ , the  $T_C$  reference value chosen is relative to the  $J_r$  value equivalent to the case of  $n_r = n_f$ . By looking at Figure 5.23a, the thrust level selected is  $T_C = 0.581$ . Drawing a horizontal line, it is possible to intersect each curve relative to each  $d_y$ , therefore obtaining the relative  $J_{T_{eq}}$  values, that are going to be used to enter in the  $P - J$  curves (Figures 5.23b and 5.25b). Intersecting the curves we obtain the power values needed to keep the same thrust, called  $P_{T_{eq}}$ . Therefore, it is possible to define a  $\Delta P$ , as in Equation 5.3.

$$\Delta P = \frac{P_{T_{eq}} - P_{iso}}{P_{iso}} \quad (5.3)$$

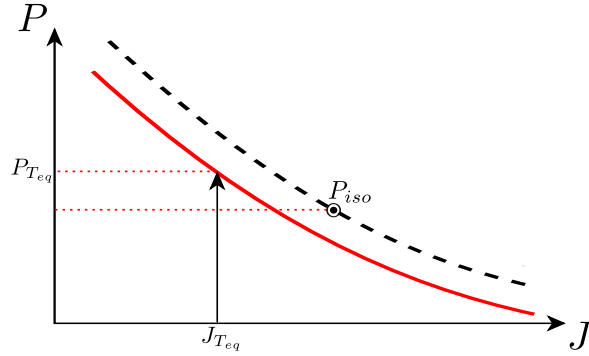


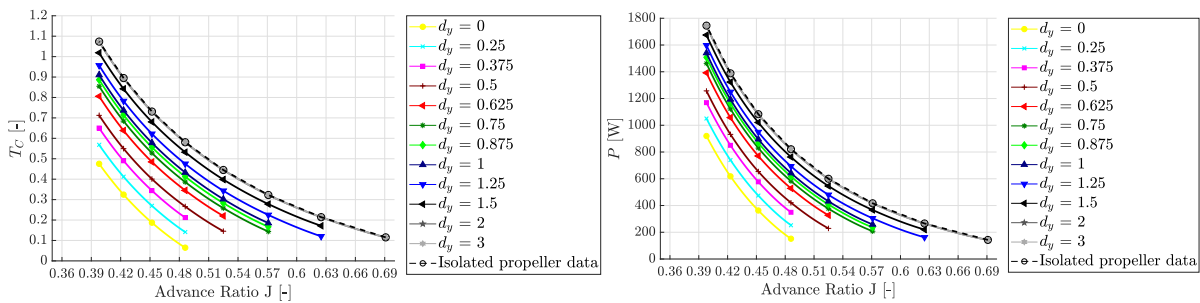
Figure 5.22: Procedure to obtain the power that in necessary to keep the same thrust after the interaction

By doing this, we have a factor that is sensitive to the specific loss due to the interaction. In Figure 5.24 the  $\Delta P$  distribution is plotted against the lateral separation  $d_y$ . The values relative to  $d_y = 0.25$  and  $0$  are not present since the intercept in the  $T_C$  plots was higher in respect to the two relative curves. It is possible to notice how dramatic are the requirements in terms of power in order to keep the same thrust already from values of  $d_y = 1.5$ . As an example, for  $n_f = 135$  rps,  $\Delta P$  for  $d_y = 0.375$  is equal to  $\approx 0.2527$ . This means that:

$$\Delta P = 0.2527 = \frac{P_{T_{eq}} - P_{iso}}{P_{iso}} \Rightarrow P_{T_{eq}} = P_{iso} \cdot (0.2527 + 1) \Rightarrow P_{T_{eq}} = P_{iso} \cdot 1.2527$$

which means that the required increased power to keep the same thrust as it was before the interaction is a  $\sim 25\%$  of the corresponding power in the isolated configuration. We can also appreciate, in the distribution of  $\Delta P$ , that the slope changes from the value of  $d_y = 0.75$  on. In fact, for lower lateral separation values the slope is much steeper, following a behaviour that was already noticed in the  $\Delta C_T$  distribution.

Referring to the case of  $n_f = 115$  rps it is possible to notice how actually the behaviour of  $\Delta P$  with  $d_y$  is not that different, even though the losses are slightly less, in fact for  $d_y = 0.375$  we find a  $\Delta P \approx 0.2018$ . Due to the fact the interaction curves are closer within each other, it was possible to intersect the whole bundle. For a total overlap, i.e.  $d_y = 0$ , it was possible to find a  $\Delta P$  slightly higher than  $0.3$ , meaning that the required power should be a  $30\%$  higher than the isolated one.



(a) Interaction effects:  $T_C - J$  curves used to obtain the require increase in power. Front rotational speed  $n_f = 135$  and  $d_x = 5.5$

(b) Interaction effects:  $P - J$  curves used to obtain the require increase in power. Front rotational speed  $n_f = 135$  and  $d_x = 5.5$

Figure 5.23: Interaction effects:  $T_C - J$  and  $P - J$  curves used to obtain the require increase in power. Front rotational speed  $n_f = 135$  and  $d_x = 5.5$  (Numerical results)

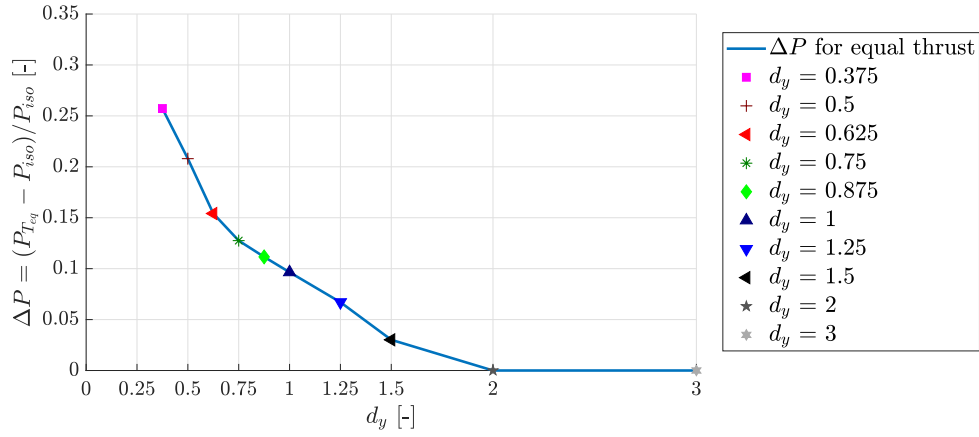


Figure 5.24: Interaction effects:  $\Delta P$  necessary to keep the same thrust between front and rear propeller. Front rotational speed  $n_f = 135$  and  $d_x = 5.5$  (Numerical results)

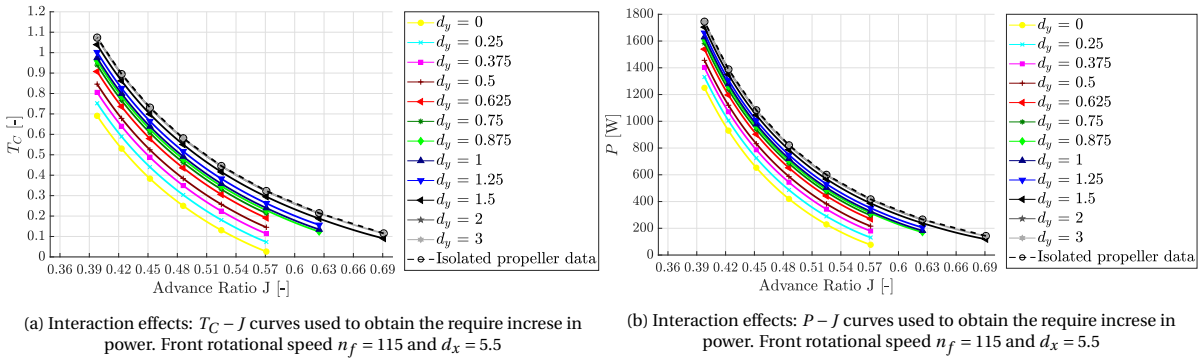


Figure 5.25: Interaction effects:  $T_C - J$  and  $P - J$  curves used to obtain the require increase in power. Front rotational speed  $n_f = 115$  and  $d_x = 5.5$  (Numerical results)

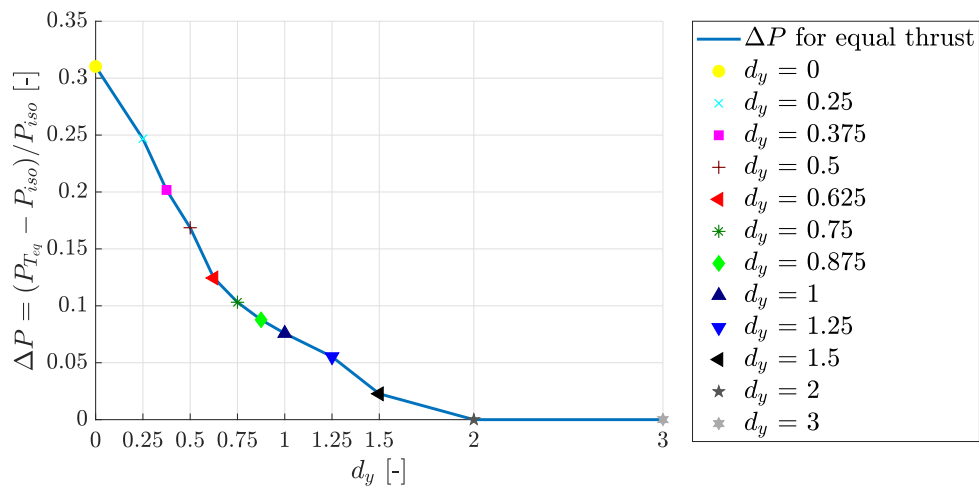


Figure 5.26: Interaction effects:  $\Delta P$  necessary to keep the same thrust between front and rear propeller. Front rotational speed  $n_f = 115$  and  $d_x = 5.5$  (Numerical results)

# 6

## EXPERIMENTAL RESULTS

In this chapter the results obtained from the experiments performed in the OJF are discussed. A brief overview of the measurements is presented in Section 6.1. In Section 6.2 the performance measurement relative to the rear propeller in isolated configuration are shown. The total pressure measurements of the front propeller slipstream and an evaluation of its thrust is discussed in Section 6.3. Finally, in Section 6.4 the effects of the interaction are shown through the performance measurements of the rear propeller.

### 6.1. MEASUREMENT OVERVIEW

A detailed description of the test parameters and condition is presented in Section 4.5. At first, the rear propeller performances were taken in isolated configuration. Secondly, the front propeller slipstream total pressure distribution were measured by using a pitot probe. Finally, with both propellers on the test platform, it was possible to measure the performance of the rear propeller with interaction. At first the axial separation factor,  $d_x$ , was equal to 5.5, and at last the close case, where  $d_x = 0.6$ , was studied. The form chosen to present experimental results proposed in this chapter is similar and comparable to the one from the numerical chapter. Therefore, the isolated propeller performance are shown in terms of  $C_T$ ,  $C_P$  and efficiency  $\eta$ . The slipstream measurement are focused on the total pressure distribution, useful to obtain the thrust of the front propeller, since it is not equipped with an internal balance sensor. The effects of the interference on the rear propeller have been obtained by balance measurements, following the procedure and the methodology presented in Chapter 4.

### 6.2. ISOLATED PROPELLER PERFORMANCE

In order to avoid errors due to each measurement set, four sweeps in rotational speed have been performed, alternating an upsweep (going from the lowest value of  $n_r$  to the highest) and a downsweep. Once that we obtain the four sets of measurements, an interpolation is performed. In Figures 6.1a and 6.1b the  $C_T$  and  $C_P$  curves for the four different sets of measurement are shown. It is possible to observe how the curves relative to the 1st and 2nd measurement sets are consistently lower if compared to the 3rd and 4th curves. Moreover, the downsweep curves are higher if compared to the respective upsweep curve. This can be explained by the fact that in the downsweep the internal temperature of the motor is quite high from the beginning of the measurements. An higher temperature cause the strain gauges inside the sensor to deform more, therefore the output signal indicates an higher value. It should also be noticed how the discrepancy between the four measurement sets is proportional with the advance ratio. The reason behind this behaviour is that we are close to the instrument sensitivity of the sensor, causing the accuracy of the measurements itself to drop. This behaviour, however, is not present in the  $C_P$  curves shown in Figures 6.1b, since they are basically on top of each other. In the same plot the fitted data and the confidence bounds of the fit, with 95% of confidence level. It is possible to notice, again, that for the  $C_P$  we obtain much more "thin" bounds if compared with  $C_T$ .

In this Chapter, the experimental results are going to be presented in terms of fitted values, in order to avoid confusion inside the graphs. The isolated propeller performance measurements in terms of  $C_T$ ,  $C_P$  and  $\eta$  are shown in Figure 6.1. It can be observed how the efficiency has a monotonous behaviour, which is something quite unusual for such a large range of advance ratios. This can be explained, again, by the fact that for the highest values of  $J$  the thrust measurements are slightly overestimated due to the lack of accuracy of the balance sensor for such small values of forces, therefore causing the efficiency to grow.

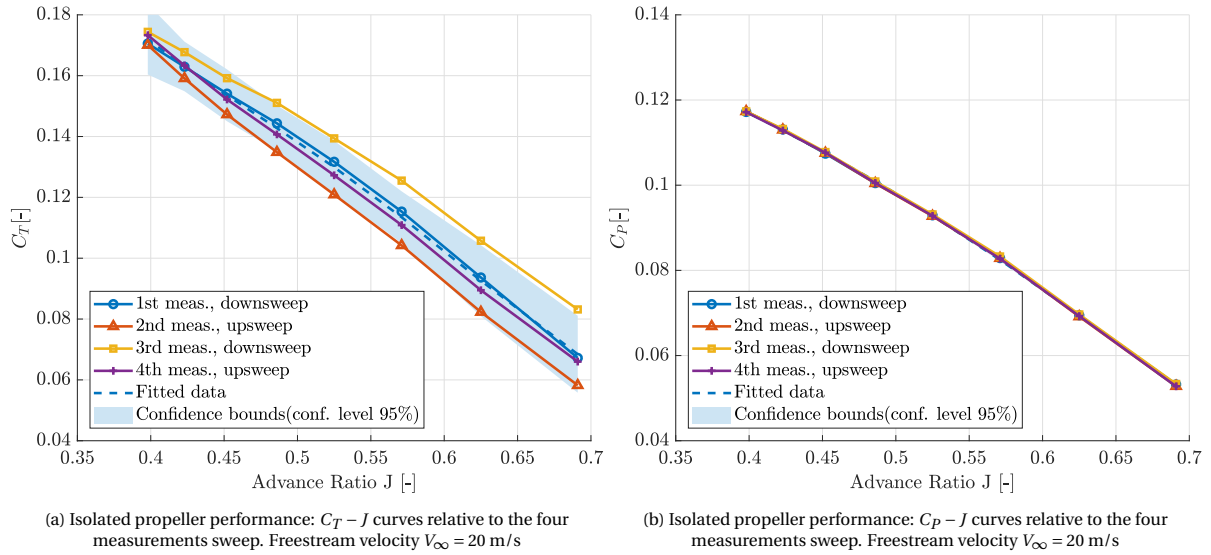


Figure 6.1: Isolated propeller performance:  $C_T - J$ ,  $C_P - J$  measurements curves and fitted data. Freestream velocity  $V_\infty = 20$  m/s

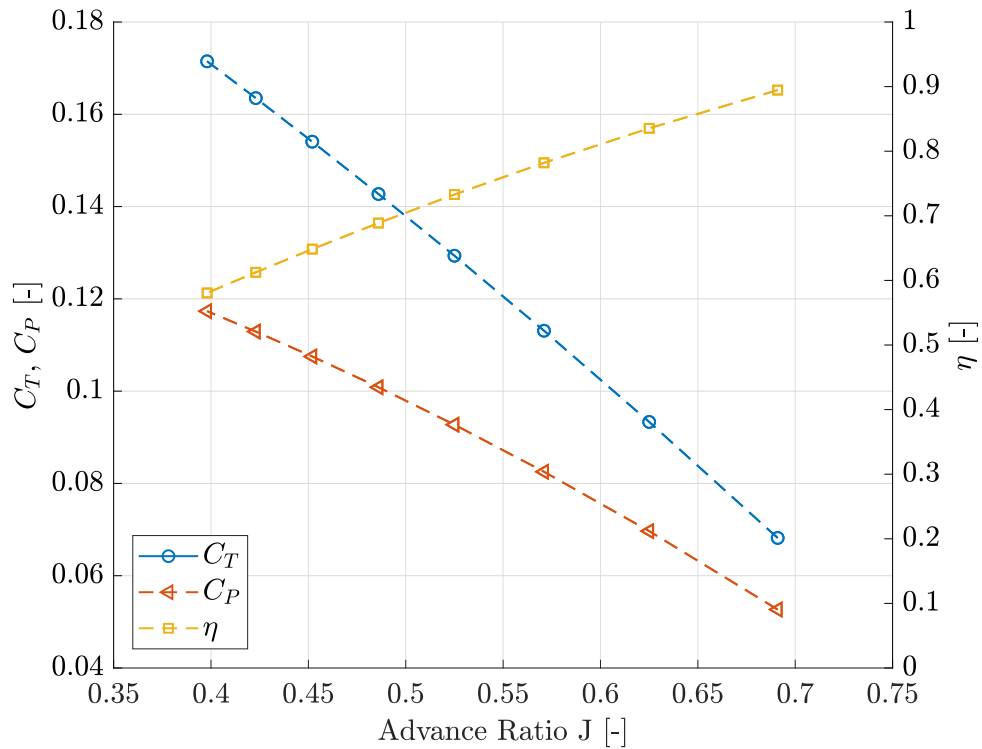


Figure 6.2: Isolated propeller performance:  $C_T$ ,  $C_P$  and efficiency  $\eta$  fitted curves from the experimental measurements. Freestream velocity  $V_\infty = 20$  m/s

### 6.3. FRONT PROPELLER SLIPSTREAM MEASUREMENTS

The propeller designed to be the front one was not equipped with an internal balance sensor. When mounting the blades on the hub, some uncertainty should be considered in the actual blade pitch angle, which is, for a given advance ratio, the main factor that determines the forces acting on the blade.

An investigation of the actual thrust level developed by the front propeller was therefore necessary, and in order to satisfy this requirement, total pressure measurements of the propeller wake have been performed. From the knowledge of the total pressure distribution behind the propeller, through an integration the thrust achieved can be evaluated:

$$T = \int_0^R 2\pi r (p_t(r) - p_\infty) dr \quad (6.1)$$

With  $p_{t,\infty}$  the average total pressure of the freestream ( $V_\infty = 20$  m/s). Therefore, the first set of measurements was performed very close to the propeller disk, with the probe swept through a range of radial positions  $\eta$  from 0.197 to 1.739, with respect to the propeller axis. In Figure 6.3 the total pressure coefficient  $C_{p,t}$  distribution over the adimensional radial distance  $r/R$  is presented.  $C_{p,t}$  is defined as such:

$$C_{p,t} = \frac{p_t - p_{t,\infty}}{q_\infty} \quad (6.2)$$

with  $q_\infty = \frac{1}{2} \rho_\infty V_\infty^2$  and  $p_{t,\infty}$  the dynamic and total pressure of the freestream velocity. It possible to see that it was possible to take measurements of the wake in radial position located at radial position smaller than the nacelle wall. The measurements taken for the propeller in pusher configuration are compared with measurements relative to the propeller in tractor configuration, i.e. with the propeller mounted in front of the motor and the nacelle. Even though not directly comparable in terms of both contraction and radial distribution of  $C_{p,t}$ , this comparison is useful since we are at least sure that the total pressure generated by the propeller in pusher configuration is the same as in the tractor configuration, for a given blade pitch and advance ratio.

However, it can be observed that even if the probe was very close to the propeller disc, contraction is already present. This can be explained by the fact that behind the rear propeller disc there is the spinner, that causes the streamlines to follow its profile and filling the gap in its center. Due to this forced contraction of the internal part of the slipstream, the whole slipstream itself contracts considerably.

By integrating the  $\Delta p$  distribution we are able to obtain the thrust values for the two levels of  $n_f$ . By comparing these values with the sensor-measured thrust of the rear propeller for the same rotational speeds, we obtain the values in Table 6.1.

$n_f$ [rps]	T [N] (from $p_t$ measurements)	T [N] (from sensor, fit)	Relative Error (%)
115	13.32	15.72	15%
135	22.45	27.22	18%

Table 6.1: Thrust computed by integrating the total pressure distribution for the two case values of  $n_f$  compared with the measured thrust from the rear propeller

It is possible to see how the error between the two types of measurements is  $\approx 15\%$  for  $n_f = 115$  rps and  $\approx 18\%$  for  $n_f = 135$ . This means that probably a correction for the contraction is necessary, in order to obtain the correct value of thrust. However, since the values of total pressure are comparable with the tractor configuration, of which we have balance measurements, we have confidence in the thrust level developed by the front propeller.

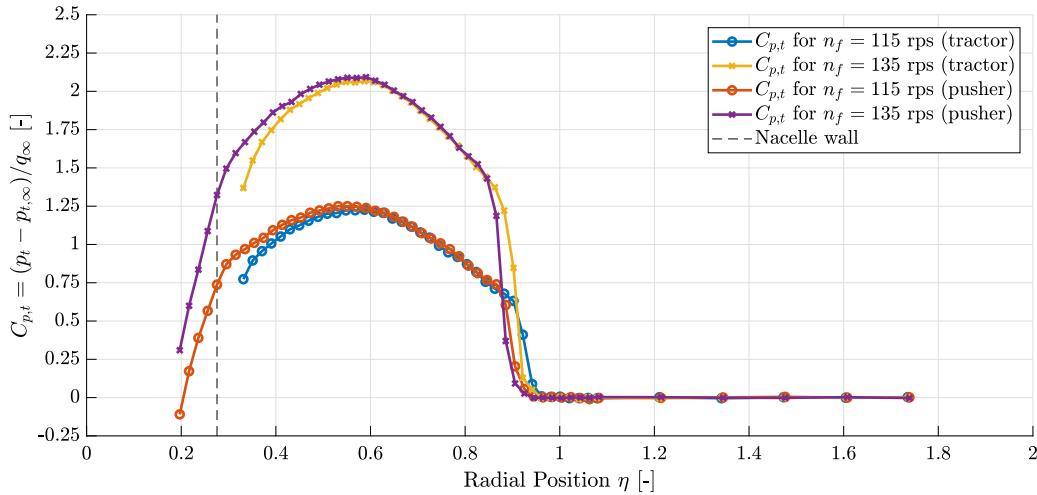


Figure 6.3: Total pressure distribution behind the propeller in pusher and tractor configuration, for  $n_f = 115$  and  $n_f = 135$  rps.

Another aspect worth investigating was the influence of the framed pylon on the front slipstream. In order to measure this effect, the total pressure probe was swept above and below the  $Y - X$  plane, for  $Z = \pm 0.084$  m, and the sweeping range was defined with  $\eta$  that goes from  $-0.918$  to  $0.918$ . The  $C_{p,t}$  distributions for the two values of  $n_f$  is presented in Figure 6.4. It can be clearly observed how the velocity deficit due to the presence of the pylon causes a small drop in the total pressure distribution. The disturbance, due to the swirl present in the slipstream, is, as expected, slightly delayed with respect to the pylon position. However, the overall distribution of total pressure is not heavily affected by the disturbance. It can also be noticed a small discrepancy from the above and below measurements for the range of  $r/R$  from 0.3 to the boundary of the slipstream. This error might be due to either misalignment of the probe while performing measurements or more probably due to an asymmetry of the whole slipstream, since every measured  $\Delta p$  goes to 0 for the same  $r/R$  value.

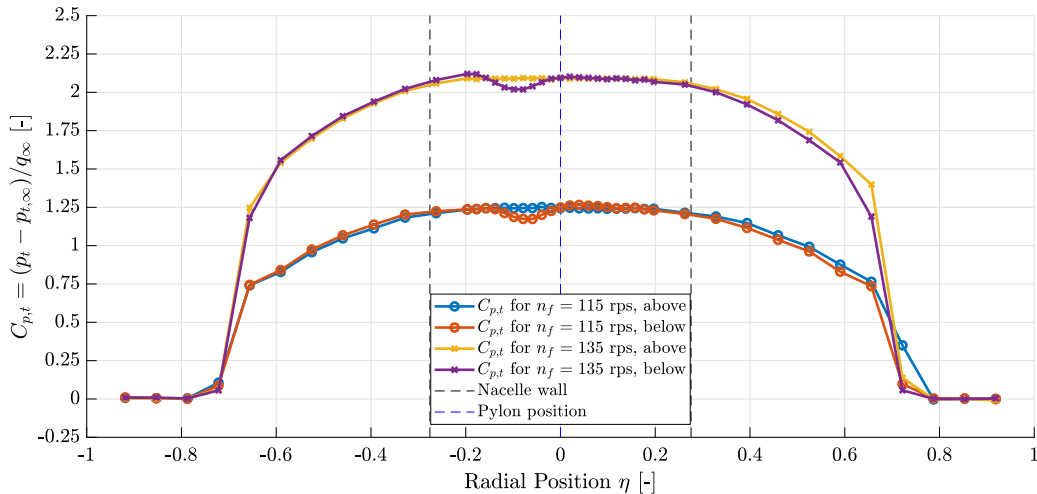


Figure 6.4: Total pressure distribution of the front propeller aimed to investigate the effects of the pylon. "Above" measurements correspond to  $Z = +0.084$  mm, while "below" measurements to  $Z = -0.084$  mm

At last, total pressure measurements of the slipstream far field were done. The probe was installed such that its tip was at  $d_x = 5.5$  radius from the propeller disc, and it was swept through a range that went from  $-159$  to  $159$  mm. Due to avoid too excessive runs of the propeller, the whole range was divided in two ranges named, by referring to Figure 6.5, negative and positive side. Negative side sees the blade going up, while the positive one sees the blade going down. The  $\Delta p$  distributions for both sides and the two values of  $n_f$  is presented in Figure 6.6.

It can be observed how, in the internal part of the slipstream, the total pressure tends to drop to very low values. This is caused by a vortex localized at the center of the slipstream, characterized by a strong swirling component, meaning that the flow in this region has a considerable angle with respect to the axial position. The total

pressure probe is not capable to measure accurately the total pressure of a flow with such angles. Moreover, due to the presence of the spinner, a separation zone is probably present in the center of the slipstream, therefore the results in this zone should not be trusted.

In order to measure properly the magnitude of this vortex, a kiel probe could have been the solution, since it can measure larger flow angles, but due to lack of wind tunnel time, it was not possible to investigate the phenomenon further. By now looking at the outer boundaries of the slipstream, we can notice how the downslope of the curves, in the positive side, looks different compared to the downslope of the distribution in the negative side. The reason behind this is not perfectly clear, but it can be due some effects of the mixing between the freestream field and the slipstream, plus some minor errors in the alignment of the probe. Compared with the closer measurement set, it can be appreciated how the edges of the slipstream itself are less defined, but the maximum of the distribution are basically the same. This should be expected, since the total pressure inside the slipstream remains constant downstream, according to the momentum theory [15].

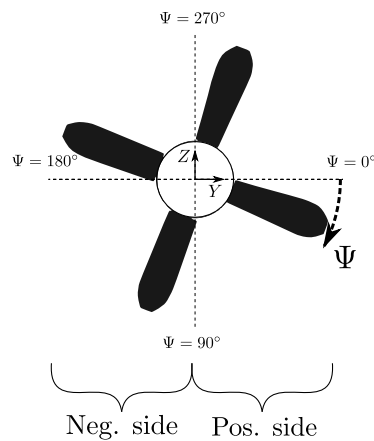


Figure 6.5: Rear view of the propeller plane: in the positive side the blade is moving downward, in the negative upward.

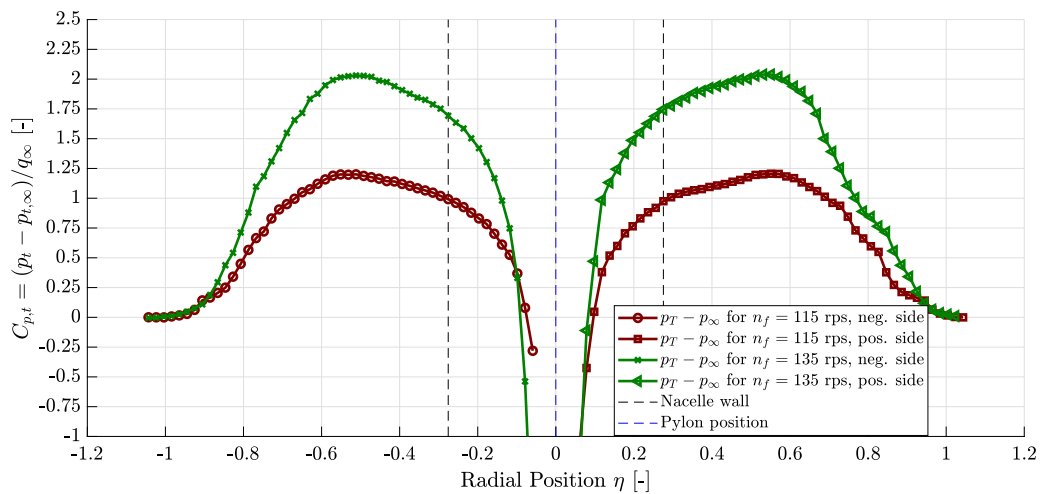


Figure 6.6: Total pressure measurements of the slipstream at  $d_x = 5.5$ , for  $n_f = 115$  rps and  $n_f = 135$  rps

## 6.4. REAR PROPELLER PERFORMANCE: INTERACTION EFFECTS

### 6.4.1. EFFECTS OF THE INTERACTION ON THE PERFORMANCE

The wind tunnel testing of the interaction was performed in two different phases. In the first one, the case where the axial separation between the propeller disc was  $d_x = 5.5$  propeller radius was done. Subsequently, the two propellers were mounted in a close proximity configuration, where  $d_x = 0.6$ . For each configuration, the front propeller rotational speed was set to two specific values,  $n_f = 115$  and  $n_f = 135$  rps. The lateral separation  $d_y$  was controlled by shifting the rear propellers over two fixed beams. For each combination of  $d_x$ ,  $n_f$  and  $d_y$ , the rear propeller was driven through an appropriate range of rps, with steps of 10 rps. The highest value of  $n_r$ , used in every configuration, was  $n_r = 165$  rps, while the lowest one depended on the  $d_y$  chosen. For every configuration four measurements were taken, in order to assure a good fit and avoid casual variation typical of a single measurement.

In Figures 6.7 to 6.10 the results are shown in terms of  $C_T - J$  and  $C_P - J$  curves, divided with respect to each  $d_x$  case and front propeller rotational speed. The measurements are presented in terms of fitted data between the four measurement sets, in order to improve the clarity of the plots. Within each plot it is possible to observe the effects of the interaction in the rear propeller behaviour, since the  $C_T$  and  $C_P$  measurements relative to the isolated configuration are plotted as well. It is possible to observe how, in the case of  $d_x = 5.5$  and  $n_f = 135$  rps (Figure 6.7a and 6.7b), the  $C_T$  becomes lower with decreasing  $d_y$ , but the rate of its decrease is different for each value of advance ratio. This is expected, since we are keeping constant the slipstream velocity field that impinges the propeller while changing the in plane component of the rear propeller. In particular, if we keep decreasing  $n_r$ , the rear propeller is more susceptible to the disturbance, therefore its performance are going to decrease more. It should be noticed how the quality of measurements can affect the accuracy of these plots. In particular, by comparing Figures 6.7a and 6.7b it is possible to appreciate how, since the balance sensor is more accurate in the torque measurements, the  $C_P - J$  curves are quite consistent, in the behaviour, within each other.

The measurements relative to the highest values of lateral separation ( $d_y = 2$  and  $d_y = 3$ ) shows some discrepancy if compared with the isolated propeller measurements. This can be due to many factors. At first, it should be mentioned that the measurements relative to the isolated case were collected with the propeller pylon mounted on turning table, due to previous testing requirements (not part of this specific work). A small play present in the turning table structure could have affected the measurements of the isolated configuration, therefore causing this discrepancy. Another reason could be that isolated and interference case have been measured in two different days, even though changes in density  $\rho_\infty$  and freestream velocity  $V_\infty$  are taken into account inside the non dimensional factors  $C_T$ ,  $C_P$  and  $J$ . However, we can confidently say that the curves are in the confidence interval of four measurement sets, therefore we can conclude that the interaction effects in this region are negligible.

A more interesting phenomenon can be observed for high loaded propellers with high values of lateral separation  $d_y$ , that can be observed in both far and close case in the thrust coefficient distributions (Figures 6.7a, 6.8a, 6.9a and 6.10a). For values of  $J \in [0.4 - 0.45]$ , the thrust coefficients data are slightly shifted towards lower values. If we look at the dashed curve this behaviour is not present. This behaviour is quite evident for  $d_y$  values up to  $d_y = 1.25$ , and not present in the  $C_P$  distribution. The cause of this local decrease in thrust is not clear, even though is not very dramatic and again, we can say that it falls in the uncertainty interval of the measurements. This effect, however, has a different nature of the increased thrust and power of the rear propeller that have been measured, in the close case, for values of overlap  $d_y = [1.75, 2]$ . In fact it can be observed how, for these aforementioned values of lateral separation, both thrust and power of the rear propeller are higher if compared both to the isolated measurement (dashed curve in the plot) and to the distribution relative to  $d_y = 3$ , that can be considered an "undisturbed" configuration of the rear propeller. This effect is more important in the  $n_f = 135$  rps case, and is totally absent in the far case, therefore we can already conclude that the close proximity between the two propellers is the cause of this increase in performance. Moreover, for the highest  $n_f$  case, the rear propeller experiences increased performances for  $d_y = 1.75$ , while in case of  $n_f = 115$  rps, the highest curve is when the lateral separation is  $d_y = 2$ .

Looking again at Figures 6.9a to 6.10b it is possible to observe that for certain values of  $d_y$ , the performance of the propeller are above the measurements relative to the isolated case. This happen especially for  $d_y = 2$  when  $n_f = 135$  rps and for  $d_y = 1.75$  when  $n_f = 115$  rps. This effect might be possibly explained as such.

When a propeller is characterized by a reasonable thrust coefficient, its slipstream has a moderate to high contraction ratio. This contraction usually takes place right behind the propeller disc, and then other effects take a lead in the phenomena such as the mixing with the freestream outside the slipstream. However, this strong contraction ratio causes the streamlines that are in proximity of the slipstream to deflect, therefore locally the

velocity vectors are characterized by an angle of attack with respect to the undisturbed velocity direction. When the two propellers are in close proximity the rear one is affected by this deflection of the freestream velocity. A certain part of its blade, therefore, is reached by a deflected vector, with an axial component which is now smaller. This "angle of attack" effect causes this part of the blade to contribute with a higher thrust and power, because a reduced axial component of the freestream shifts the local advance ratio to smaller values, therefore the local  $\alpha$  seen by the blade section is larger as well as the lift. Depending on how much the two propellers are overlapped, on the thrust level of the front propeller (that determines the intensity of the contraction), this effect allows the rear propeller not only to recover the loss of performance due to the interaction, but also to slightly outperform with respect to the isolated case.

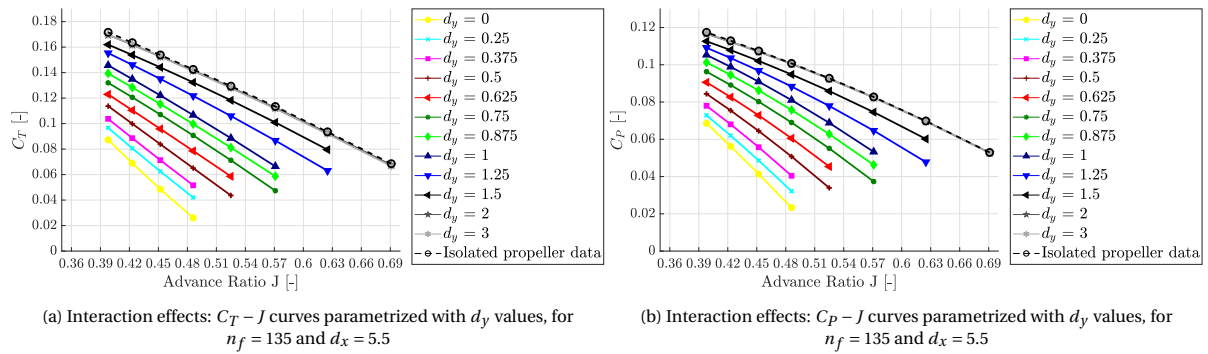


Figure 6.7: Interaction effects:  $C_T - J$  and  $C_P - J$  curves parametrized with  $d_y$  values, for  $n_f = 135$  and  $d_x = 5.5$  (Experimental results)

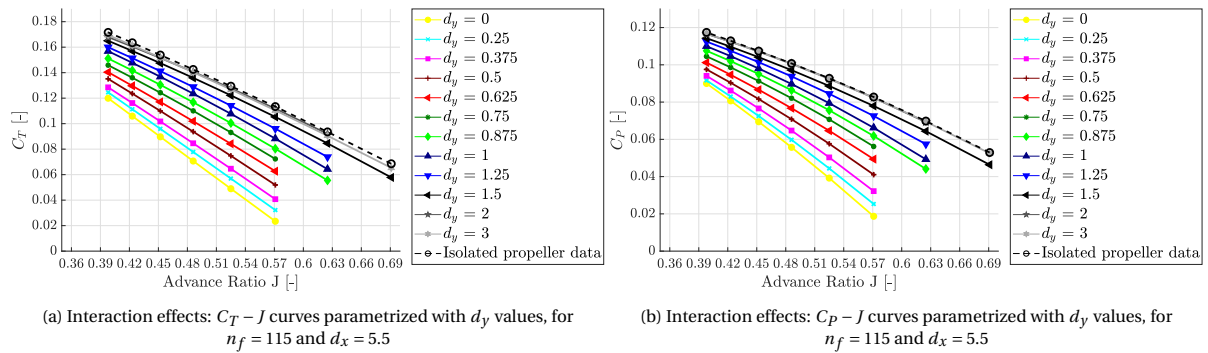


Figure 6.8: Interaction effects:  $C_T - J$  and  $C_P - J$  curves parametrized with  $d_y$  values, for  $n_f = 115$  and  $d_x = 5.5$  (Experimental results)

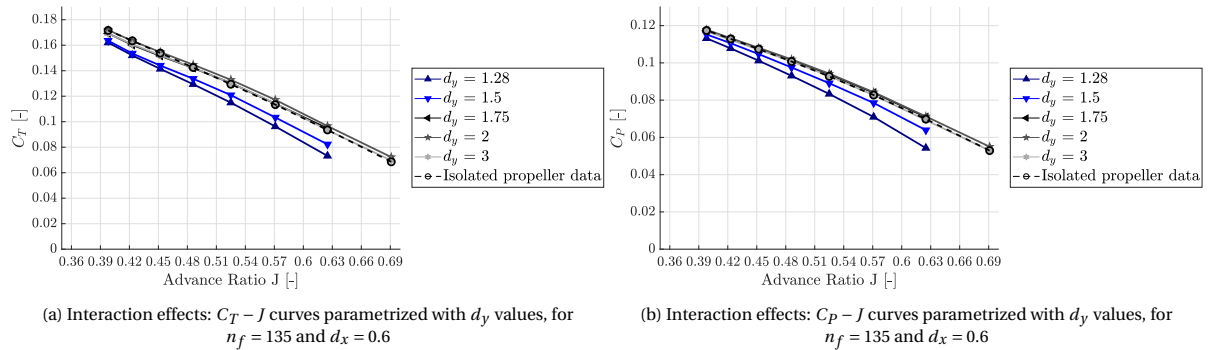


Figure 6.9: Interaction effects:  $C_T - J$  and  $C_P - J$  curves parametrized with  $d_y$  values, for  $n_f = 135$  and  $d_x = 0.6$  (Experimental results)

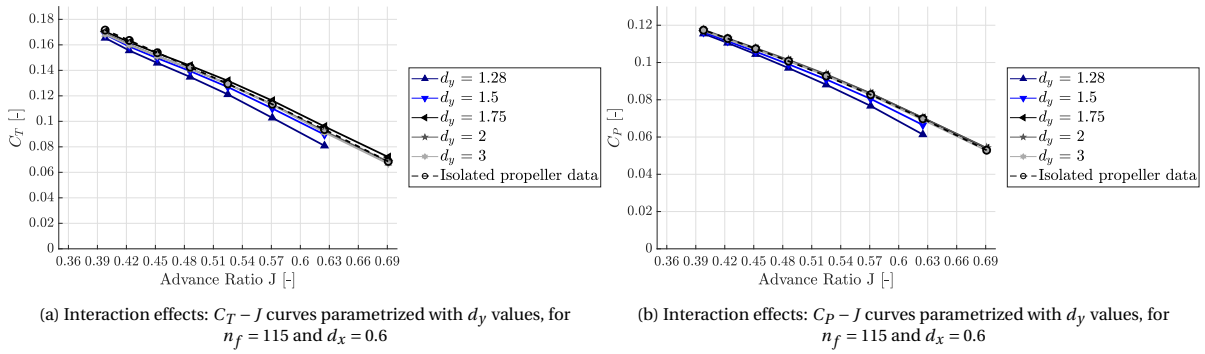


Figure 6.10: Interaction effects:  $C_T - J$  and  $C_P - J$  curves parametrized with  $d_y$  values, for  $n_f = 115$  and  $d_x = 0.6$  (Experimental results)

#### 6.4.2. EFFECT OF THE INTERACTION ON THE REAR PROPELLER THRUST

It is now important to understand the actual effects on the thrust of the front propeller slipstream ingestion. In order to do this, in the same manner as it was done in the numerical results chapter, the behaviour of the  $\Delta C_T$  factor (Equation 5.1) is studied, versus the lateral separation  $d_y$ . In Figures 6.11a and 6.12a the results relative to the  $d_x = 5.5$  case are shown, while in Figures 6.11b and 6.12b the results from the close case are presented. If we look at the curve relative to  $J_r = 0.398$ , which corresponds to the maximum rps value used for the rear propeller ( $n_r = 165$  rps) it is possible to appreciate the effects of the front propeller thrust level on the interaction. In fact, if we consider  $d_y = 0$ , the loss of thrust of the rear propeller is  $\Delta C_T \approx 0.5$  for  $n_f = 135$  rps, while for  $n_f = 115$  rps its value is  $\Delta C_T \approx 0.3$ . The increased rotational velocity of the front propeller causes an increased load distribution, that proportionally induces a velocity field on the slipstream higher in magnitude. The rear propeller sees an increased axial component of the velocity, hence its thrust is more affected. The change in slope of the  $\Delta C_T$  curve from the value of  $d_y = 1$ , already noticed in the correspondent numerical results, can be observed also in the experimental measurements. As already discussed, the reason might lay in the  $v_{t,s}$  distribution over the rear propeller disc, whose contribution to the local angle of attack can be either positive or negative, in terms of losses.

Focusing now the attention towards the close case plots, it is possible to appreciate the increased thrust, minor in the  $n_f = 135$  rps case (Figure 6.11b), much more important in the  $n_f = 115$  rps case (Figure 6.12b). Looking at the curve relative to  $J_r = 0.571$ , for  $d_y = 1.75$ , a small negative  $\Delta C_T$  is present.

Comparing the far and close case, it is possible to see how the value of  $\Delta C_T$  for  $d_y = 1.25$  (far case) and  $d_y = 1.28$  (close case) are quite different. Due to the close proximity between the two propeller discs, the axial velocity component of the slipstream is not already equal to twice its value. Therefore, the rear propeller sees, in the close configuration, a lower  $v_{t,s}$  distribution, therefore experiencing reduced thrust and power losses.

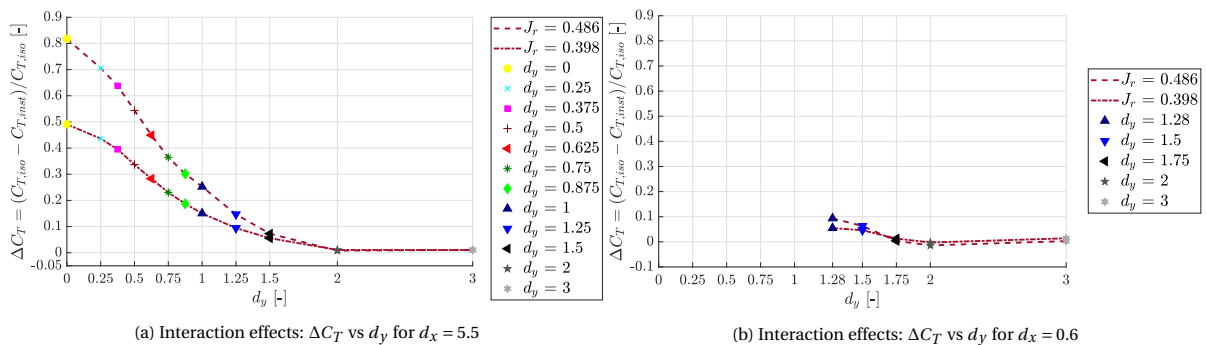


Figure 6.11: Interaction effects:  $\Delta C_T$  vs  $d_y$  for  $d_x = 5.5$  and  $d_x = 0.6$  parametrized with two values of advance ratio  $J_r$  and  $n_f = 135$  rps (Experimental results)

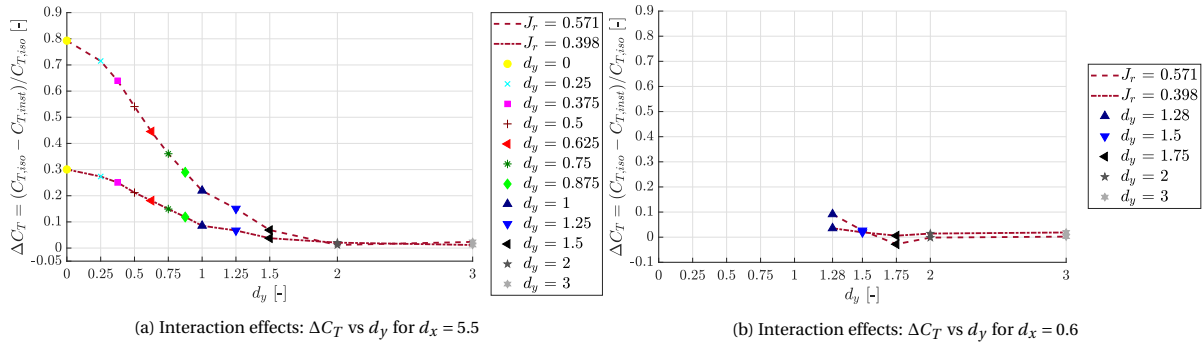


Figure 6.12: Interaction effects:  $\Delta C_T$  vs  $d_y$  for  $d_x = 5.5$  and  $d_x = 0.6$  parametrized with two values of advance ratio  $J_r$  and  $n_f = 115$  rps (Experimental results)

### 6.4.3. INCREASED POWER REQUIREMENT TO RECOVER THE LOSS OF THRUST

In this Subsection the same procedure from Subsection 5.4.5 is presented, but using the results from the experimental measurements. In order to appreciate some actual effects, the results here proposed are relative to the case where  $d_x = 5.5$ . In Figures 6.13a and 6.13b the distributions of thrust coefficient  $T_C$  versus advance ratio  $J$  and the relative plot for power developed by the propeller are presented for  $n_f = 135$  rps. The same curves relative to the other value of  $n_f$ , 115 rps, are shown in Figures 6.15a and 6.15b.

If we look at Figures 6.14 and 6.16 it is possible to appreciate the behaviour of the  $\Delta P$  versus the lateral separation factor  $d_y$  for the two values of  $n_f$ . In Figure 6.14 the value relative to  $d_y = 0$  is not present since the horizontal curve for  $T_C = 0.605$  ( $J_r = 0.486$ ) does not intercepts the relative curve.

The behaviour of the  $\Delta P$  is similar to the one evaluated through the numerical approach. It can be noticed how, comparing the two curves, how the one relative to  $n_f = 115$  rps present a more linear behaviour from  $d_y = 0$  to  $d_y = 1$ , while the other one has a small depression for  $d_y = 0.75$ . Moreover, it should be noticed the behaviour of the curve for the highest values of  $d_y$ . In fact, since the measurements of the isolated case are not exactly equal to the ones performed for those values of lateral separation, a negative  $\Delta P$  is present. However, a trend can be observed, in particular the lowest value of  $\Delta P$  can be found for  $d_y = 2$ , with a small recovery increasing the separation further.

From the previous Subsection, we saw that, when both propellers were at the same rotational speed, the  $\Delta C_T$  distributions were quite comparable. However, by looking at the curves proposed in this Subsection, it is possible to notice how the two distributions show that for an higher rps value of the front propeller, more power is required to recover from the interaction.

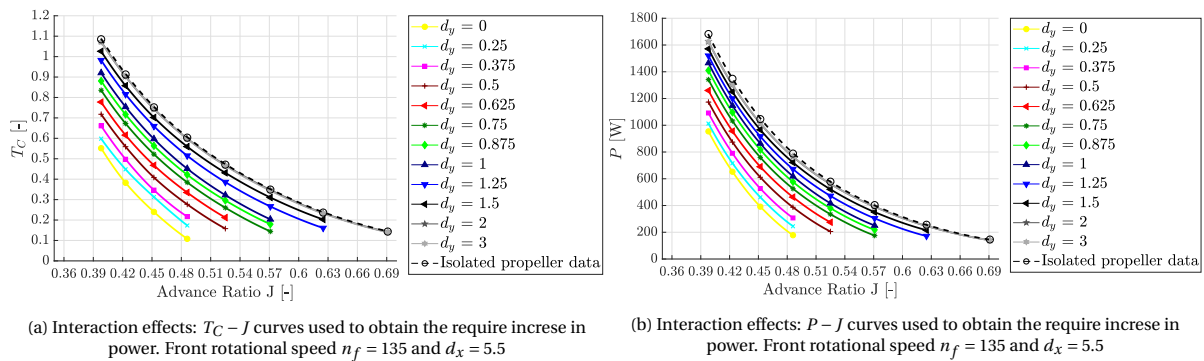


Figure 6.13: Interaction effects:  $T_C - J$  and  $P - J$  curves used to obtain the require increase in power. Front rotational speed  $n_f = 135$  and  $d_x = 5.5$  (Experimental results)

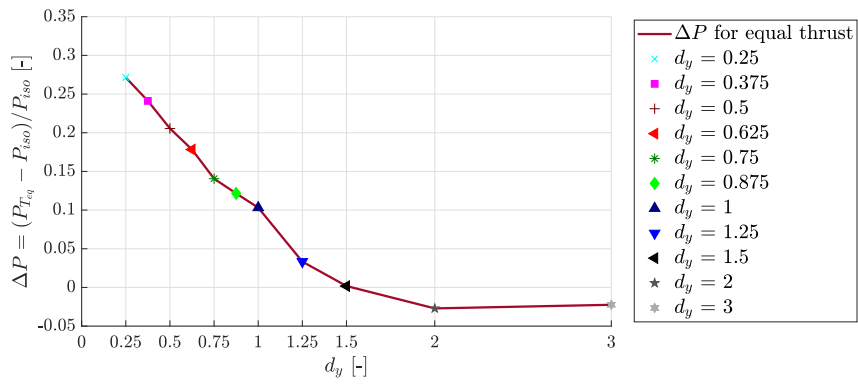
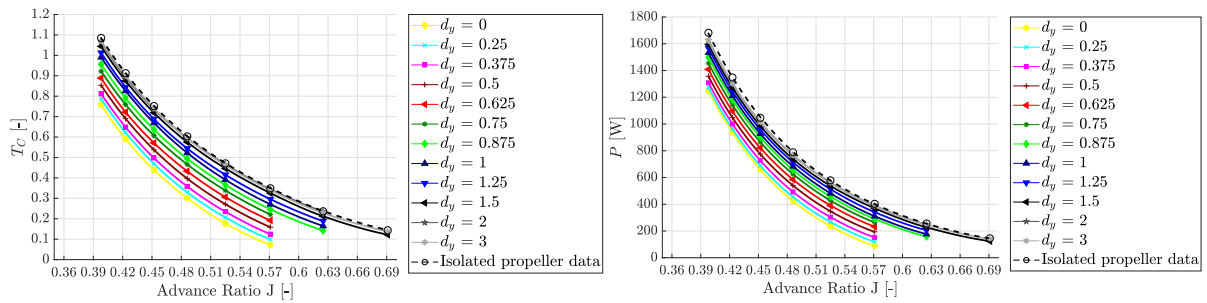


Figure 6.14: Interaction effects:  $\Delta P$  necessary to keep the same thrust between front and rear propeller. Front rotational speed  $n_f = 135$  and  $d_x = 5.5$  (Experimental results)



(a) Interaction effects:  $T_C - J$  curves used to obtain the require increase in power. Front rotational speed  $n_f = 115$  and  $d_x = 5.5$

(b) Interaction effects:  $P - J$  curves used to obtain the require increase in power. Front rotational speed  $n_f = 115$  and  $d_x = 5.5$

Figure 6.15: Interaction effects:  $T_C - J$  and  $P - J$  curves used to obtain the require increase in power. Front rotational speed  $n_f = 115$  and  $d_x = 5.5$  (Experimental results)

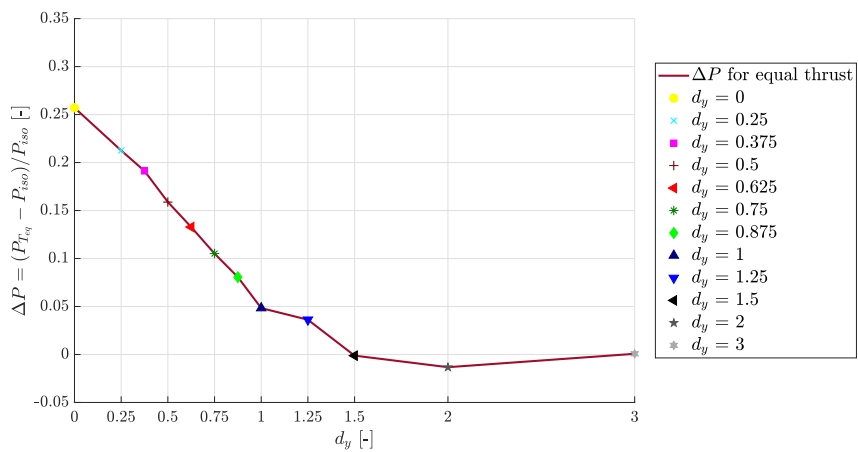


Figure 6.16: Interaction effects:  $\Delta P$  necessary to keep the same thrust between front and rear propeller. Front rotational speed  $n_f = 115$  and  $d_x = 5.5$  (Experimental results)

# 7

## COMPARISON AND DISCUSSION OF NUMERICAL AND EXPERIMENTAL RESULTS

The previous two chapters of this result part presented separately the numerical and experimental evaluations obtained, showing the effects on the rear propeller due to impingement of the front propeller slipstream. In this Chapter, the numerical and experimental results will be compared.

The structure of this chapter will be similar to the one of the previous parts, in Section 7.1 the performance measurements of the isolated propeller are going to be compared with the numerical computation of the isolated propeller performance. In Section 7.2 the measurements of the front propeller total pressure will be compared with the ones evaluated through the numerical slipstream model. Finally, in Section 7.3 the interaction effects evaluated by the numerical and experimental approach will be compared.

### 7.1. ISOLATED PROPELLER PERFORMANCE

In this Section the results relative to the propeller performance in isolated configuration are compared with the experimental measurements, as shown in Figure 7.1.

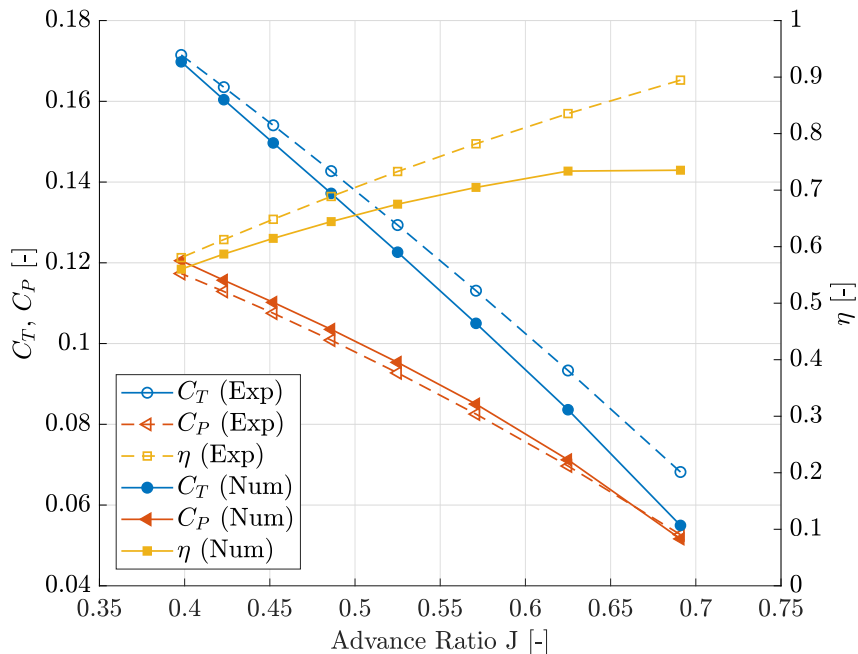


Figure 7.1: Isolated propeller performance:  $C_T$ ,  $C_P$  and efficiency  $\eta$  fitted curves from numerical and experimental measurements. Freestream velocity  $V_\infty = 20$  m/s

The results are valid for a freestream velocity of  $V_\infty = 20$  m/s and a range of  $J = [0.4 - 0.69]$ . It is possible to observe that the results are not too far from each other.

In particular, the  $C_T$  obtained with Prop1D is slightly underestimated for the whole range of  $J$ , while the  $C_P$  is overestimated through almost the entire range, but it gets closer to the experimental data for high  $J$ . The numerical  $C_T$  results agree better with the experimental data for low  $J$ , and at highest advance ratios values the maximum difference is observed. The two efficiency curves are quite different between each other, and this is due to the offsets between the  $C_T$  and  $C_P$  curves.

It should be noted that, for  $J = 0.69$ , the Reynold number of the effective velocity seen by the blade are quite low (from 200000 to 70000). For such low Reynold numbers it is expected that the 2D analysis performed by RFOIL to be inaccurate. The inaccuracy probably lies in an overall overestimation of the drag experienced by each sections, causing the  $\eta$  and  $C_T$  to drop, but increasing the  $C_P$ .

Moreover, looking at the efficiency curve obtained through the experimental measurements and is monotonous behaviour, it could also be possible that the sensor provided overestimated values of thrust when the advance ratios is pretty high. For the highest values of  $J$ , the thrust is in the range of 8 to 4 N, values that are close to the sensibility of the sensor, causing it to be inaccurate in the output signal.

Therefore, considering the first half of advance ratios range used, this offset might be decreased by applying a corrective factor to the sectional 2D drag coefficient, in order to tuning properly the sectional contributes to thrust and torque. Anyhow, since the main purpose of this work was to validate the numerical interaction method hence the  $\Delta$  between isolated and installed performances, this correction to the iso values was not applied.

## 7.2. FRONT PROPELLER SLIPSTREAM

In this Section a comparison between the numerical model of the slipstream and the experimental measurements is discussed. In Figures 7.2 and 7.3 the total pressure coefficient  $C_{p,t}$  evaluated for the close and the far case evaluated through the two different approaches are presented. The total pressure is numerically evaluated following the procedure presented from Equation 2.13 to 2.2.2. The reference freestream velocity is 20 m/s. Only the positive side measurements (reference to Figure 6.5 are shown. It is possible to appreciate the offset between measurements and evaluation, not only in maximum value but also in the radial distribution. In the close case, for  $d_x = 0.6$ , the real slipstream is already more contracted compared to the model. In fact, the numerical approach does not take into account the spinner effect and the gap in its center is not modelled, therefore its contraction ratio is way less pronounced. The discrepancy is way more evident if we look at the  $d_x = 5.5$  case, where the velocity field of the actual slipstream spans from  $\eta \approx 0.1$  to  $\approx 0.9$ , while the range of influence of the numerical model is more narrow, from  $\eta \approx 0.28$  to  $\approx 0.9$ . Moreover, in both cases (close and far), the total pressure distribution has higher values for almost the whole range of  $\eta$ . This can be expected to have an influence in the interaction effects, as measured and as numerically evaluated.

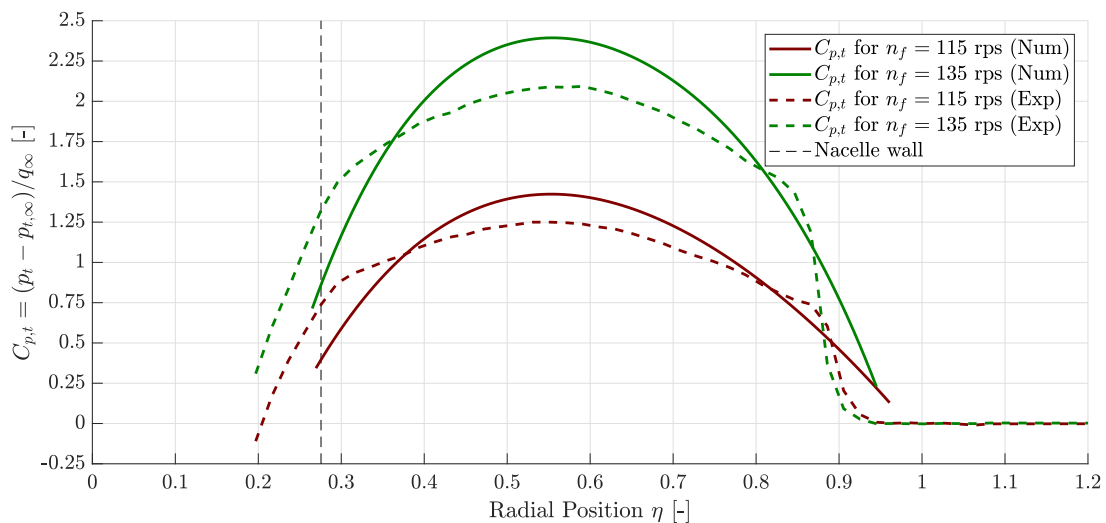


Figure 7.2: Front propeller slipstream total pressure distributions for the close case, experimental measurements compared with numerical evaluations.

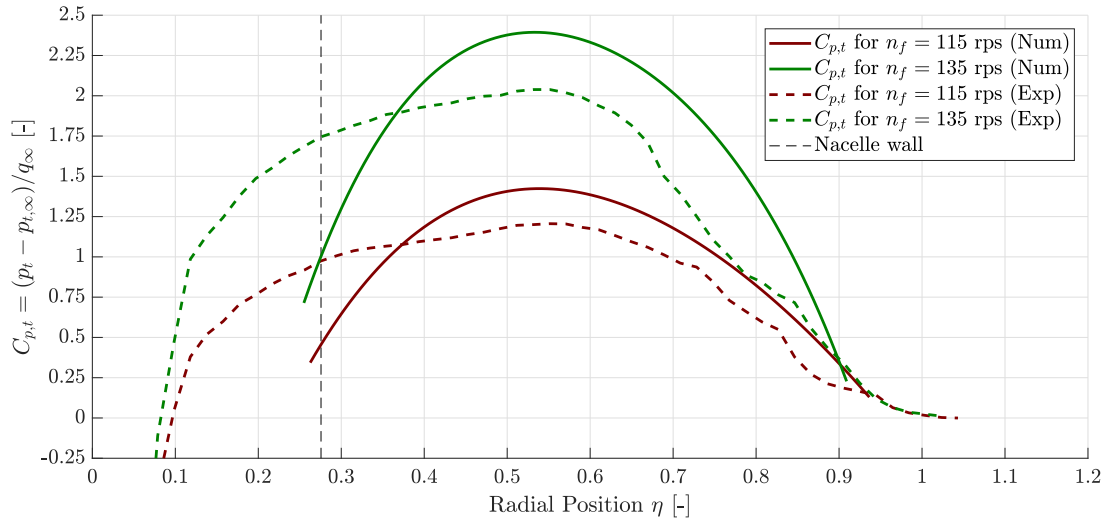


Figure 7.3: Front propeller slipstream total pressure distributions for the far case, experimental measurements compared with numerical evaluations.

### 7.3. REAR PROPELLER PERFORMANCE: INTERACTION EFFECTS

It is now possible to discuss the results relative to the rear propeller performance affected by the interaction. The comparison is done by correlating the same type of evaluations from the numerical and experimental result chapters. Therefore, in Subsection 7.3.1 the effects on thrust due to the overlap are compared, while in 7.3.2 the evaluation relative to the power requirements needed to keep constant thrust through the interaction are discussed.

#### 7.3.1. EFFECT OF THE INTERACTION ON THE REAR PROPELLER THRUST

Considering the two axial separation cases,  $d_x = 5.5$  and  $d_x = 0.6$ , and the two front propeller rotational speed values,  $n_f = 135$  and  $n_f = 115$  rps, the results from the numerical and experimental approaches regarding the variation of thrust  $\Delta C_T$  due to the overlap, are presented in Figures from 7.4 to 7.7. In these plots, the curves evaluated through the numerical approach are shown in red, while the ones obtained by experimental measurements in black. Far and close case are not shown in the same plots to avoid confusion, and the plots are divided with respect to the two front propeller advance ratios. The  $\Delta C_T$  distribution relative to a rear propeller advance ratio equal to the one of the front propeller is denoted with "equal rps", while "maximum rear rps" indicates the behaviour relative to the highest value of rear propeller rotational speed of the whole range. A quick look to every plots, shows that the offset is quite small between experimental and numerical values, which validates the numerical method. By using the  $\Delta C_T$  factor it is possible to withdraw the differences between the  $C_T$  values evaluated through the experiments and numerical method, both for the isolated and installed configuration and focus the attention towards the actual impact that the interaction has on the performance.

Looking at Figure 7.4, we can notice different regions where we can find similar behaviours between the two pair of curves. In the first of these region, for  $0 < d_y < 0.375$ , the program overestimates the losses. In this region, the biggest difference is for  $d_y = 0$ , where the numerical  $\Delta C_T$  is 8.7% bigger for equal rps and 13.5% bigger for maximum rps. The offset then decreases and for  $d_y = 0.375$  numerical and experimental values are basically on top of each other. For these low values of  $d_y$  a big part of the rear propeller is interested by the slipstream flow, and the center of the slipstream almost matches the center of the propeller. By looking at the total pressure distribution measured in the wind tunnel testing and the slipstream results obtained in the numerical model (Figure 7.3), it is possible to notice how different they are from each other. We can consider the radial position  $\eta$  as an equivalent to  $d_y$ , with  $d_y = 0$  the center of the front propeller. Even though it is not possible to directly compare the two, since in reality there are no "fixed" boundaries of the slipstream, and at  $d_x = 5.5$  mixing between internal and external flow is already happening, it is possible to notice how the real slipstream is more contracted than the numerical.

When  $d_y$  is very small, the internal part of the slipstream reaches the spinner of the rear propeller. The blade is therefore interested by the slipstream field from  $\eta \approx 0.3$  to its external edge. In this region, the numerical total pressure distribution is higher than the experimental, therefore we can assume that also the induced axial velocity is higher, causing the program to overestimate the losses in this range of  $d_y$ . Similar conclusion can be drawn for the  $n_f = 115$  rps case (Figure 7.6), where the biggest offsets are found for  $d_y = 0$ , where the numerical

$\Delta C_T$  is 16% bigger for equal rps and 19% for maximum rps. In this case the losses relative to the maximum rps case are consistently lower for both numerical and experimental results. Even though the behaviour of  $\Delta C_T$  is still comparable between the two  $n_f$  cases, it should be noticed how, for  $n_f = 115$  and  $d_y = 0$ , the numerical and experimental values are further from each other compared to the previous case. Going on with the separation, it is possible to appreciate how the numerical and experimental results for  $d_y = 0.375, 0.5$  agree quite well within each other, for each case.

As opposed to what we observed in the previous region, for  $n_f = 135$  rps, we see that for  $0.5 < d_y < 1$  the losses evaluated through the experimental data are bigger than the numerical. This region has the same extent in both equal and maximum rear rps case. Since we already established that the values of total pressure in the numerical model are higher compared to the experimental measurements, something else is causing the real losses to be higher. In this region, the central part of the front slipstream is directly impinging the propeller blade. A remarkable difference between the real and modelled slipstream, is that in the former its center is characterized by a strong root vortex, while in the latter the center has a constant distribution of axial and tangential components. Unfortunately, it was not possible to obtain more insightful results of this vortex, but it is possible to state that its effect on the propeller blade is certainly more dramatic, if compared to a constant distribution of inflow. The effects of an external vortex on a propeller have been studied by Yang in ref. [35], where it was found that a co-rotating vortex has a strong impact both in the thrust and torque of the propeller. The situation for  $n_f = 115$  rps is similar, even though the offsets are reduced, and the range of  $d_y$  spans from 0.5 to 0.875 for equal rps and from 0.5 to somewhere between 0.875 and 1 for maximum rear rps. It can also be noticed how, in this region the experimental distribution presents a quasi-linear behaviour, while a pronounced curvature is visible in the numerical values distribution.

From  $d_y = 1$  to  $d_y = 2$ , the program results are, again, higher than the experimental. For this range we can assume that the central vortex is outside the rear propeller area, therefore the  $\Delta C_T$  evaluated numerically are probably higher due to higher values of total pressure, i.e. induced velocity field, evaluated in the program. In this case, it should be observed how the results relative to the maximum rear rps case are agree quite well between each other. This might be explained by the increased accuracy of the numerical evaluation for low advance ratios, which also for isolated configuration results to be more similar with the experimental values. The two curves are more spread apart for the equal rps, because we are now at values of advance ratios where agreement between numerical and experimental evaluations is not very satisfying. Finally, we can appreciate how, for  $d_y = 2$  and 3, there is a small offset between numerical and experimental data. It is hard to tell the cause of this disagreement. Obviously, numerical  $\Delta C_T$  in this region is equal to 0, since there is no direct overlap of the two propellers. However, in the wind tunnel testing many things could have caused this discrepancy. One reason could be that measurements done for the isolated case and for those two values of  $d_y$  are different due to causes not directly related by the interaction, as for example random fluctuation of the wind tunnel speed, or vibrations of the testing table that might be different when only one or two propellers are mounted on it. A more important gap, is observed for  $n_f = 115$  rps, suggesting that probably the thrust level of the front propeller has an influence on this behaviour.

Looking now at the Figures relative to the  $d_x = 0.6$  case (Figures 7.5 and 7.7), we can already see how consistently between numerical and experimental approaches, the thrust coefficient losses are less pronounced if compared to the far case. Anyhow, it is possible to notice that for  $d_y = 1.28$  (close to  $d_y = 1.25$ ) numerical results are again above the experimental one. The effects of increased performance, seen in the experimental measurements presented in Chapter 6 is more appreciable for  $n_f = 115$  rps, in case of lateral separation  $d_y = 1.75$ .

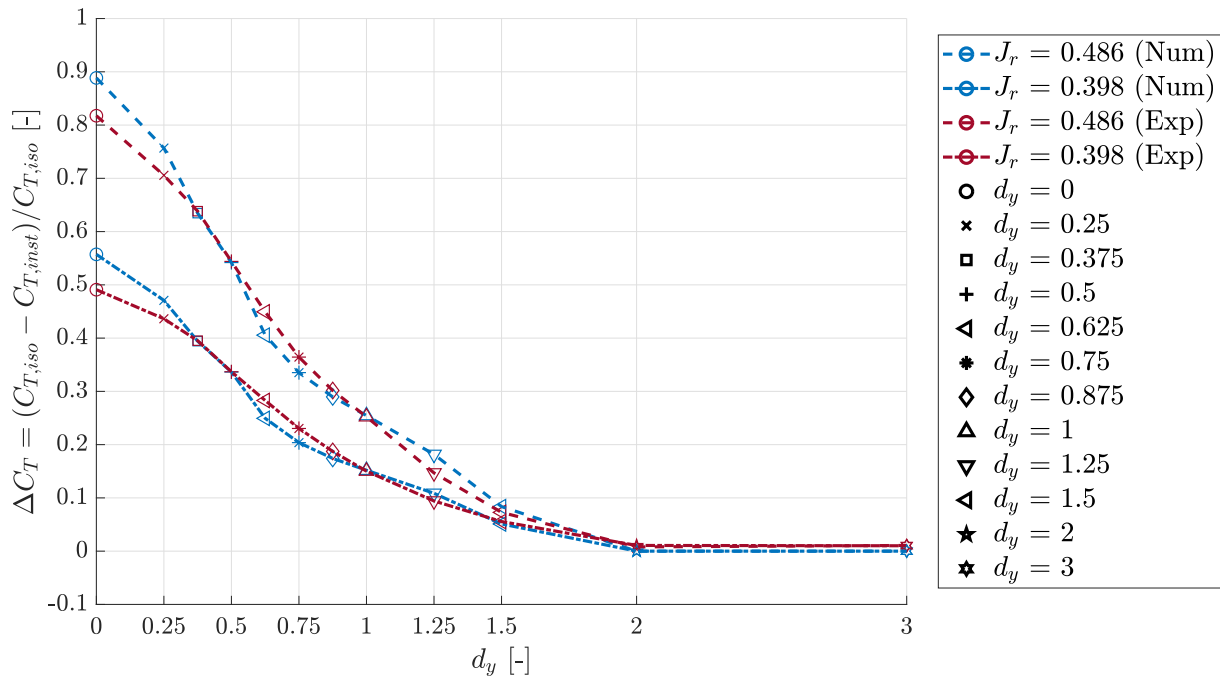


Figure 7.4: Interaction effects:  $\Delta C_T$  vs  $d_y$  for  $d_x = 5.5$  parametrized with two values of advance ratio  $J_r$  and  $n_f = 135$  rps, comparison between numerical and experimental results

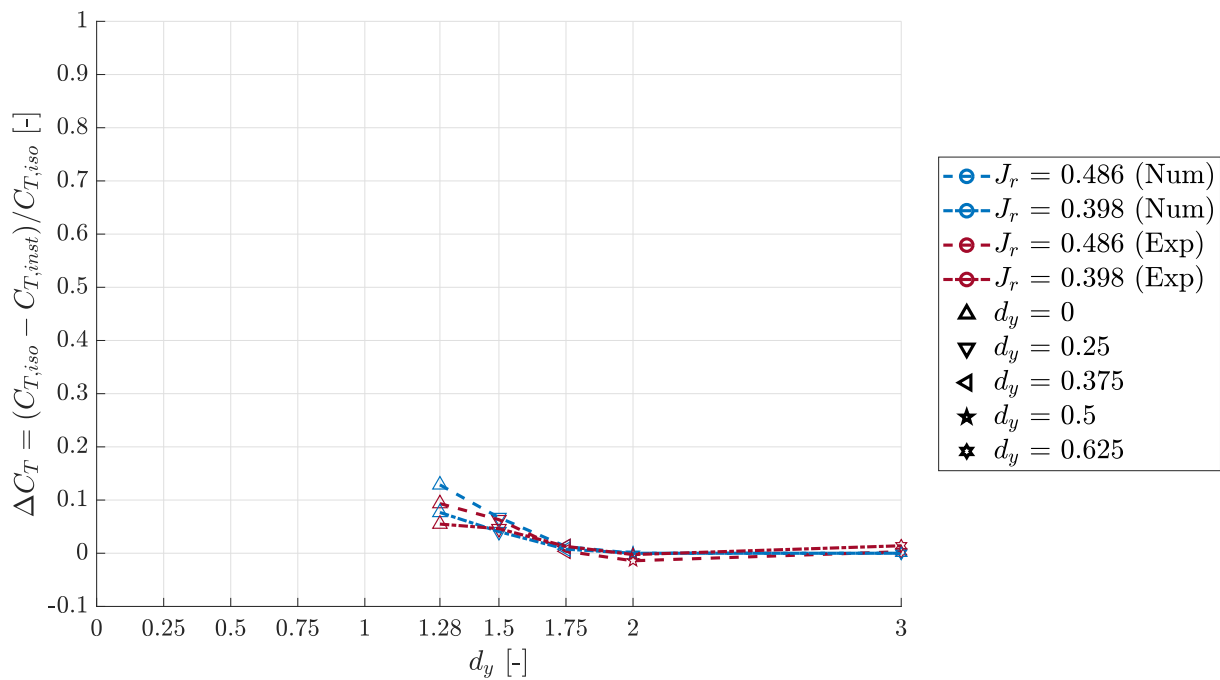


Figure 7.5: Interaction effects:  $\Delta C_T$  vs  $d_y$  for  $d_x = 0.6$  parametrized with two values of advance ratio  $J_r$  and  $n_f = 135$  rps, comparison between numerical and experimental results

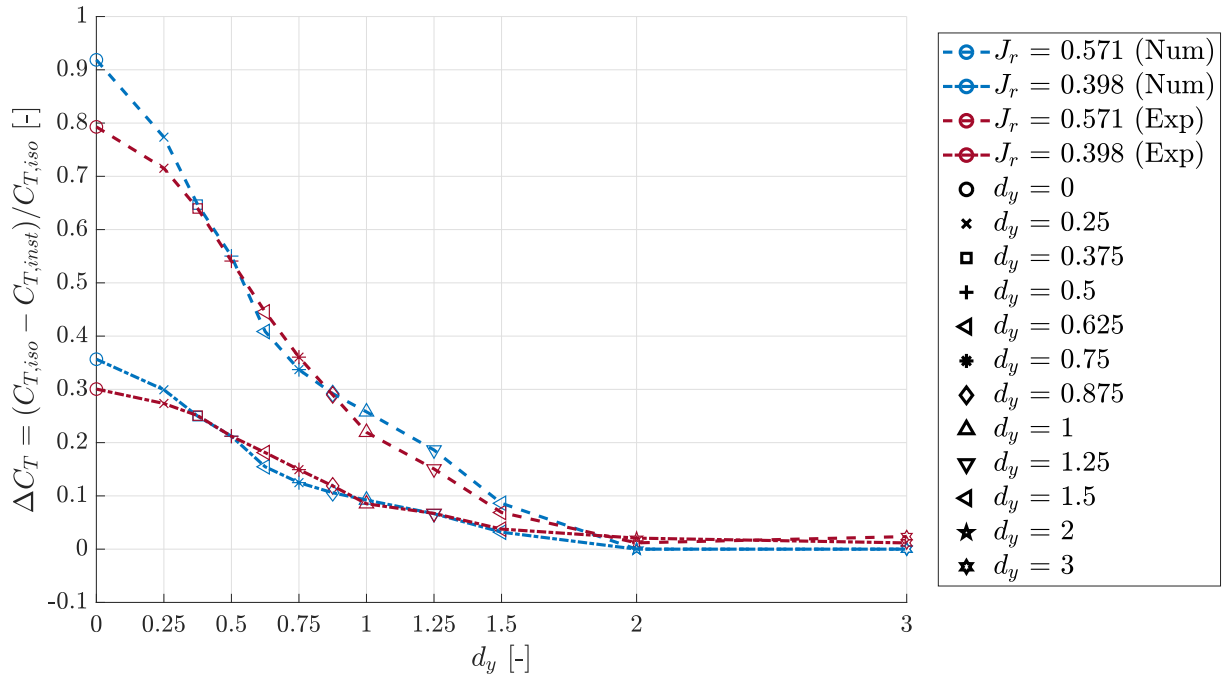


Figure 7.6: Interaction effects:  $\Delta C_T$  vs  $d_y$  for  $d_x = 5.5$  parametrized with two values of advance ratio  $J_r$  and  $n_f = 115$  rps, comparison between numerical and experimental results

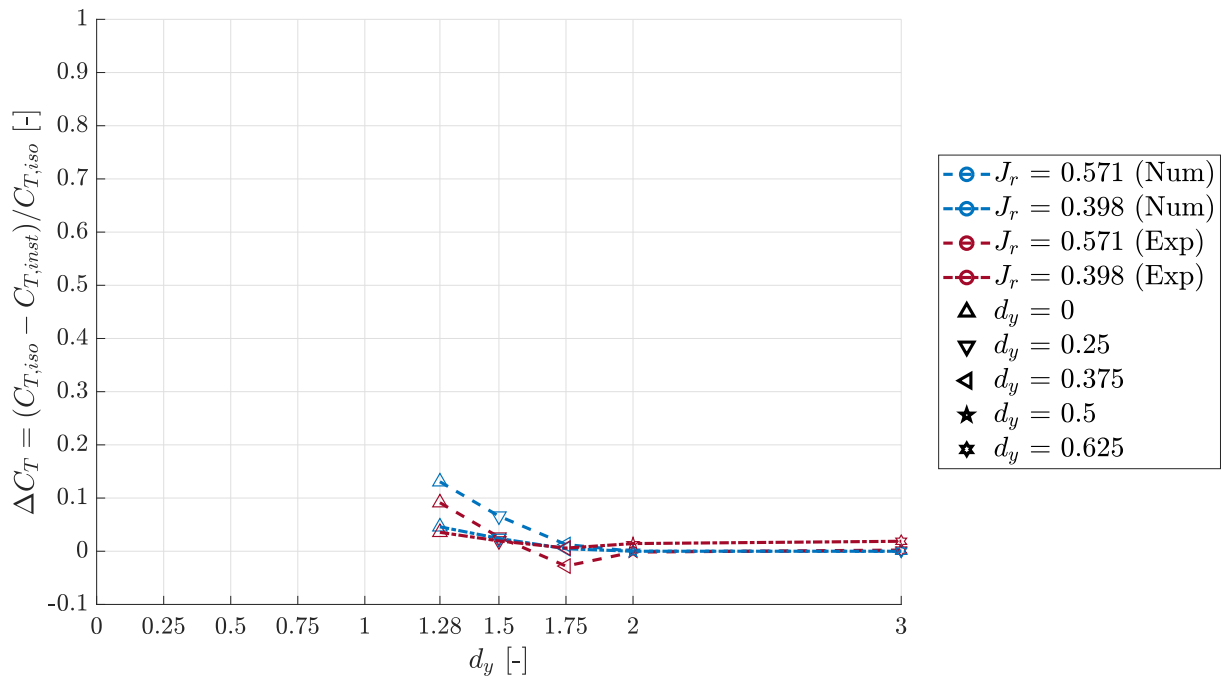


Figure 7.7: Interaction effects:  $\Delta C_T$  vs  $d_y$  for  $d_x = 0.6$  parametrized with two values of advance ratio  $J_r$  and  $n_f = 115$  rps, comparison between numerical and experimental results

### 7.3.2. INCREASED POWER REQUIREMENT TO RECOVER THE LOSS OF THRUST

In this Subsection the results relative to the power requirement  $\Delta P$  needed to keep the same thrust of the front propeller are compared between the numerical and experimental evaluations. Only the case where  $d_x = 5.5$  is considered, since the results are more evident. In Figure 7.8 the results relative to  $n_f = 135$  rps are presented, while in Figure 7.9  $n_f$  is 115 rps. In both plots, good agreement is present between experimental and numerical results.

Looking at the first plot, unfortunately, it was not possible to compare the results up to  $d_y = 0$  since the equal- $T_C$  horizontal line does not intercept the last curve in the experimental plot. Similar thing happen in the numerical plot, in fact the results relative to  $d_y = 0$  and 0.25 are not present. From  $d_y = 0.5$  to 1 the numerical results are lower than the experimental and it can be noticed how, for the same range of  $d_y$ , the numerical  $\Delta C_T$  were lower than the experimental, as shown in Subsection 7.3.1. So, it should be expected that a less dramatic prediction of performance losses leads to a slightly underestimation of how much power the rear propeller needs to develop to recover from these losses. As already said in the previous Subsection, the cause of this offset might be addressed to the presence of the central vortex in the slipstream, that causes increased losses not taken into account in the numerical model, even though if we look at Figure 7.9, in the same range of  $d_y$  the experimental and numerical evaluations are basically on top of each other. Increasing the separation, from  $d_y = 1$  to  $d_y = 1.5$ , the numerical  $\Delta P$  is higher than the experimental. Again the situation is equivalent to what happen in the  $\Delta C_T$  distribution for the same  $d_y$  range. Finally, it is possible to see how the differences in the measurements taken from the isolated case and the two highest values of lateral separation are different from each other, causing the gap between the curves.

For  $n_f = 115$  rps, it was possible to compare the whole range of  $d_y$ . It can be noticed how, for  $d_y = 0$  the power requirement is consistently higher in the numerical evaluation, but from  $d_y = 0.5$  to  $\approx 0.875$  the numerical evaluations agree quite well with the measurements. The more pronounced offset in  $d_y = 0$  can be explained by the gap present in the  $\Delta C_T$  distribution for the same value of lateral separation. As before, the overpredicted losses in the numerical model are to be addressed to explain why the power requirement is higher. Quite similar behaviour of the two curves is observed in the range from  $d_y = 1$  to 1.5, even though the numerical curve is consistently high in the range. As for the  $\Delta C_T$  distribution, the experimental evaluations for  $d_y = 2$  is not equal to zero as expected, on the other hand for the highest value of lateral separation the value of  $\Delta P$  is  $\approx 0$ .

It is quite clear how the curves, both numerical and experimental, for the two different cases proposed, are quite close to each other. This was already appreciable in the  $\Delta C_T$  curves relative to the "equal rps" case. Therefore, we can say that when both propellers have the same thrust level, the behaviour of the losses with respect to the lateral separation is the same.

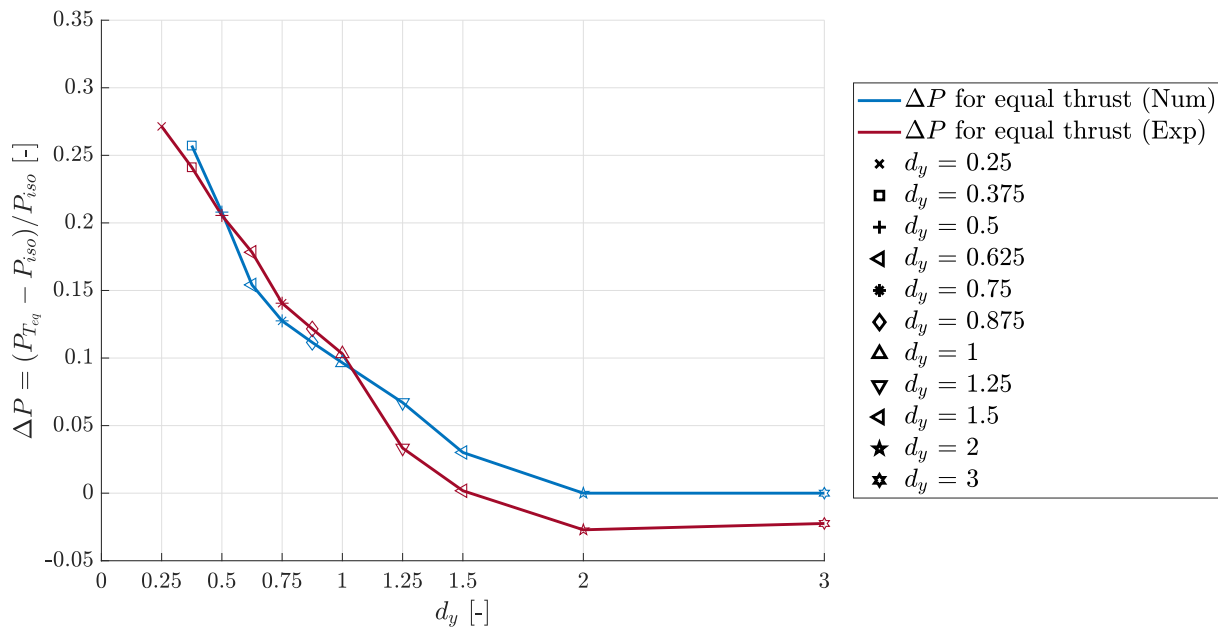


Figure 7.8: Interaction effects:  $\Delta P$  necessary to keep the same thrust between front and rear propeller. Front rotational speed  $n_f = 135$  and  $d_x = 5.5$ , comparison between numerical and experimental results

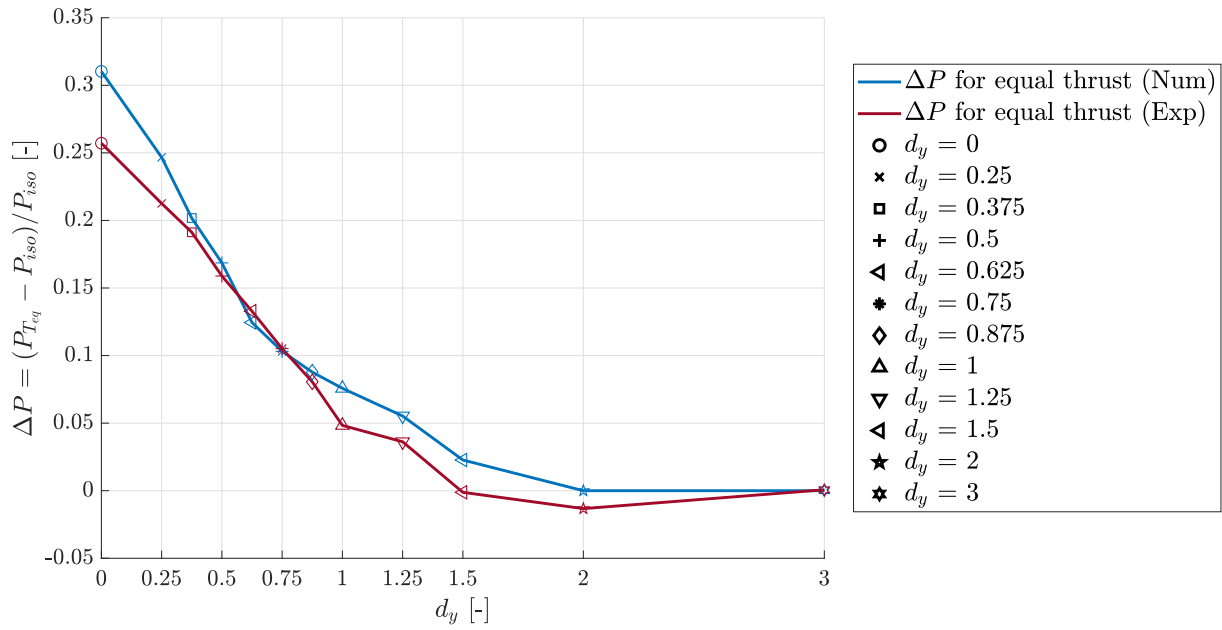


Figure 7.9: Interaction effects:  $\Delta P$  necessary to keep the same thrust between front and rear propeller. Front rotational speed  $n_f = 115$  and  $d_x = 5.5$ , comparison between numerical and experimental results

These power requirements should be taken into account when designing vehicles characterized by propellers in overlapping configurations. In fact, it is fundamental to have an autonomous system able to measure the loss of thrust and provide the correct power in order to equalize thrusts. We can conclude that for a given percentage of loss in thrust, it is usually necessary to provide the same percentage of extra power necessary to maintain the thrust at its undisturbed value.

# 8

## CONCLUSIONS AND RECOMMENDATIONS

This Chapter presents the conclusions and recommendations for future work based on the investigations carried out in this thesis. The main conclusions are discussed first in Section 8.1, followed by recommendations, given in Section 8.2.

### 8.1. CONCLUSIONS

This report was focused on the numerical and experimental study of the effects of the interaction between two propellers in overlapping configuration. In particular, the behaviour in terms of performance of the rear propeller, that was characterized by the impingement with the front propeller slipstream, was studied. Different parameters were selected, as for example the front propeller rotational speed, the axial separation between the two propellers and the lateral separation.

The isolated propeller measurements were compared with the numerical results, showing a good agreement especially for low advance ratios. The offsets present for higher advance ratios values were justified by considering the lack of accuracy of the sensor for such low values of thrust. However it should be considered that in this area the lack of accuracy in predicting the viscous effect in the numerical model introduces a considerable error in the solution.

Measurements of the front propeller slipstream were performed at different axial position. It was possible to appreciate how a strong contraction was present even when very close to the propeller disc. The comparison with the numerical model of the slipstream showed substantial differences. First of all, due to the lack of nacelle/spinner effect on the slipstream model, the contraction ratio followed is different from the relative measurements. Moreover, the distribution of total pressure along the radial direction of the slipstream, in the numerical model, does not change, since no friction or mixing effect is taken into account. Moreover, the slipstream is characterized, in its center, by a strong hub vortex that was not possible to measure properly, since the total pressure probe used was too thin, therefore it was subject to strong vibrations.

The effects of the interaction have been studied by changing different parameters. Two of them are axial and lateral separation between the propellers. The influence of these two parameters are discussed below:

- *Effect of the axial separation  $d_x$* : in terms of axial separation between the two propellers, two cases were studied, called close and far case. In the close case, the distance between the propeller discs in the axial direction was equal to 0.6 propeller radius (both propellers have the same radius). In the far case the distance was 5.5 propeller radius. By looking at the performance it was possible to conclude that when the two propellers are in close proximity, for given  $n_f$ ,  $n_r$  and lateral separation, the rear propeller was less affected by the interaction. The cause of this behaviour is not fully understood, though. One cause might be related to the fact that since we are close to the propeller disc, the slipstream induced velocity is not fully developed, therefore its value is smaller compared to the one in the far case. Moreover, it was possible to observe that for a given  $n_f$  and for certain values of  $d_y$ , by increasing the value of advance ratio of the rear propeller, its performances were higher compared to the isolated case. It was concluded that this was an effect of the strong contraction of the front propeller slipstream. Since high gradients of contraction are presents near the propeller disc, at this location the streamlines of the flow outside

the slipstream results inclined as well. This angle of the velocity vector of the slipstream causes the rear propeller blade to be interested, in proximity to the interference region, by a reduced axial velocity. This local increasing of the advance ratio permits the blade to contribute more to thrust and torque, therefore increasing the averaged performance. We can conclude that, from the results of both experimental and numerical evaluations, the closer the two propellers are within each other in terms of axial distance, the less the rear propeller sees a decrease in performance.

- *Effect of the lateral separation  $d_y$* : a broad range of  $d_y$  values was chosen in order to understand properly the influence of the overlap on the effects. In particular, the range went from  $d_y = 0$ , that correspond to an alignment of both propellers' axis, to  $d_y = 3$ , in order to be sure that no strong interactions could happen. In the close case it was necessary to have a narrow range of  $d_y$ , with the smallest value equal to 1.28. The more the two propellers were overlapped, the more the rear one suffered the effects of the front propeller slipstream impingement. In both numerical and experimental evaluation it was possible to appreciate that when both propeller had the same rotational speed, the rear one suffered, for  $d_y = 0$  a loss of his thrust (evaluated through the factor  $\Delta C_T$ ) equal to the 80% of the value relative to the isolated case. Increasing the separation, the losses decreases as well, but even for relatively high values of  $d_y$ , like 1.25,  $\Delta C_T$  is in the order of 15 - 20%. It was observed that, by changing  $n_f$  or  $n_r$ , the behaviour of the  $\Delta C_T$  was quite consistent in terms of curve slope. An increased gradient of losses could be observed by comparing the values from 1.5 to 1 and from 1 to 0.5. The gradient of  $\Delta C_T$  is higher in the second range, which correspond to a situation where the rear propeller's blade goes through the center of the slipstream. Since both propeller have the same rotational direction, some sections of the blade see the swirl component of the slipstream velocity field in the same direction of the rotation. This causes a reduction of the in-plane total velocity therefore causing a further decrease of the local angle of attack and more losses.
- *Effect of the front propeller rotational speed  $n_f$* : it was possible to observe, even by looking solely at the curves of  $C_T - J$  and  $C_P - J$  parametrized with lateral separation  $d_y$ , that an increased rotational speed of the front propeller is linked to larger losses of performance of the rear propeller. The higher load distribution of the front one caused its slipstream to be characterized by higher values of axial and tangential induced velocity components. This causes part of the rear propeller blade that goes through the slipstream to be at an increased advance ratio, therefore developing smaller values of lift and drag, contributing less to the total thrust and torque of the propeller. Comparing the  $\Delta C_T$  experienced by the rear propeller in an overlapping configurations where  $d_x = 5.5$ ,  $d_y = 0$ ,  $n_r = 165$  rps (lowest advance ratio tested), for both front propeller rotational speeds level, it can be observed what just discussed. In fact, for  $n_f = 135$  rps,  $\Delta C_T$  is in the order of  $0.5 \div 0.55$ , meanwhile for  $n_f = 115$  rps the losses reaches values of  $30 \div 35\%$ . However, an interesting finding was found when looking at how the rear propeller was affected by the interaction in the case of  $n_f = n_r$ . It was found that the  $\Delta C_T$  behaviour vs  $d_y$  was consistently equal in both cases, suggesting that a comparable level of interaction happen when both propellers have the same thrust level, i.e. the same rotational speed. A possible explanation of what is happening can be done considering that, as already said, the induced velocity field in the slipstream shed by a propeller, is proportional to its load distribution. Therefore, if the rear propeller is at the same rotational speed of the front one, the non uniform inflow distribution of the slipstream velocities causes losses that are always the same, regardless of the rotational speeds chosen for both propellers.

This study has provided an extensive insight regarding the fundamental effects on a propeller subject to an interaction with another propeller slipstream. Since it was ascertained that the lateral overlap between the propellers is the main factor that determines the impact on the rear propeller performance, it is necessary to be cautious when designing such vehicles. Another aspect worth an investigation is the requirement, in terms of supplied power, needed to keep both propellers at the same thrust despite the losses due to the interaction. An increase in power means that it is necessary to decrease the advance ratio at which the propeller is operating, by increasing its rotational speed. From the evaluation presented in the results part of this work, it was possible to conclude that the power needed to recover the loss of thrust is proportional to the loss itself. For high degrees of overlap, the power requirement can reach values up to the 25% of the corresponding power in the isolated case. Therefore, it is possible to predict, once that a certain lateral separation is chosen, not only the losses that the rear propeller would face, but also the necessary requirement to keep the propeller at the same thrust. Another solution, once established the gravity of the losses encountered by the propeller, might be to increase the blade pitch in order to develop more thrust.

## 8.2. RECOMMENDATIONS FOR FUTURE WORKS

Even if the experimental and numerical work presented led to clear conclusions regarding the interaction phenomenon of interest, several improvements could be done to the results. Both the numerical and the experimental approach could be explored more deeply, as it will be discussed below.

Several improvements could be done to the numerical approach proposed. If the actual solution of the propeller loads could be considered as sufficiently accurate, considering the short time necessary to evaluate the results, as shown in the results Part of this work some strong assumptions have been made, causing a certain degree of approximation in the results. An improved model of the slipstream would be ideal to have an increased accuracy in the evaluation of the interaction effects. A vortex lattice model could be integrated to the propeller solution provided by the BEMT code, along with a free wake model, even though the computational time would be largely increased. Another recommendation would be to consider the effect of the spinner/nacelle, not only to improve the propeller solution itself, but also to obtain a more geometrically correct model of the slipstream. The BEMT code used in this work uses a database of aerodynamic coefficients obtained through the 2D panel code RFOIL. By doing this, a satisfactory compromise between computational time and accuracy of the solution is found. However, it would be necessary to improve the results further, to perform the analysis of the blade sections through a Computational Fluid Dynamics (CFD) study. Actually, CFD would be an effective way to simulate the entire propeller and its interaction with the other propeller wake. However, it should be noticed that such computation would be very expensive, and would require an accurate meshing process, since the blade would be affected, for a large part, by an unsteady flow. Obviously, a future CFD analysis of this situation could be done in different degrees of accuracy, for example considering only the rear propeller in a rotational frame and a time-averaged slipstream that impinges it. More complex analysis could involve a full unsteady solution of both propellers.

The application of Particle Image Velocimetry (PIV) could help in understanding more the actual behaviour of the flow between the propellers. In fact, a visualization of the flow direction and magnitude in front of the rear propeller would be fundamental to draw more conclusions about how the front slipstream actually reaches and impinges the rear propeller disc. Moreover, further imaging of the back part of the front propeller, therefore a study of its slipstream, would be useful to understand how the load on the propeller is actually distributed. Along with flow visualization, noise measurements could provide fundamental informations about the pressure field around the rear propeller. These measurement would be important not only because they would guarantee an improvement in the description of the interaction, but also a useful data to understand the noise impact of such configuration. In fact, we should not forget that the main application of eVTOL configuration would be in an urban context, therefore their noise emission should be studied and taken into account during the design phase.

Finally, as far as it concerns the testing parameters, it would be interesting to see the effects of the freestream velocity on the interaction. In fact, the experiments were done for a given value of  $V_\infty$ , enough high to be representative of a cruise speed, but low enough so that the propeller would be able to develop a considerable thrust. However, it would be interesting to see how the interaction is sensitive to lower freestream velocities. Different values of the freestream velocity will cause the mixing of the external and slipstream flow to be different, therefore the velocity distribution over the rear propeller will results quite diverse. The propellers were tested without any angle of attack with respect to the freestream velocity. Propeller's behaviour is sensitive to the angularity of the flow, therefore it should be expected how the results of the interaction would be affected by testing the propellers with different angle of attacks. This configuration is relevant since in the reference eVTOL vehicles it is actually probable that such interaction would happen when the vehicle is a transition phase between hover maneuvers and horizontal flight.



# **IV**

## **APPENDICES**



# A

## INFLUENCE OF THE CRITICAL AMPLIFICATION FACTOR

In this Appendix the influence of the critical amplification factor on the propeller's performance solution performed by Prop1D is presented. In Figure A.1 the  $C_T - J$  curves are shown, while in Figure A.2 the equivalent  $C_P$  distributions are presented.

In RFOIL the transition from a laminar to a turbulent boundary layer is predicted using the  $e^N$  method by van Ingen [36]. In this method, the critical amplification factor is based on a number of flow field parameters and external excitations. In the analysis proposed in this work, a value of  $N = 4$  was chosen. However it is useful to understand how the propeller solution, in terms of thrust and power developed, is sensitive to this parameter. It can be observed how the thrust of the propeller is almost unaffected by  $N$ , as it can be seen in Figure A.1. On the other hand, increasing the value of  $N$ , the evaluated power of the propeller decreases. A reduced value of  $N$  means that the transition points on both lower and upper side of the airfoil move towards the leading edge, causing a decambering effect on the boundary layer. Therefore, higher values of  $C_P$  should be expected for the lowest values of  $N$ , however it is actually the opposite. This could be explained by the fact that due to the airfoil properties, a more turbulent flow causes the local drag to decrease.

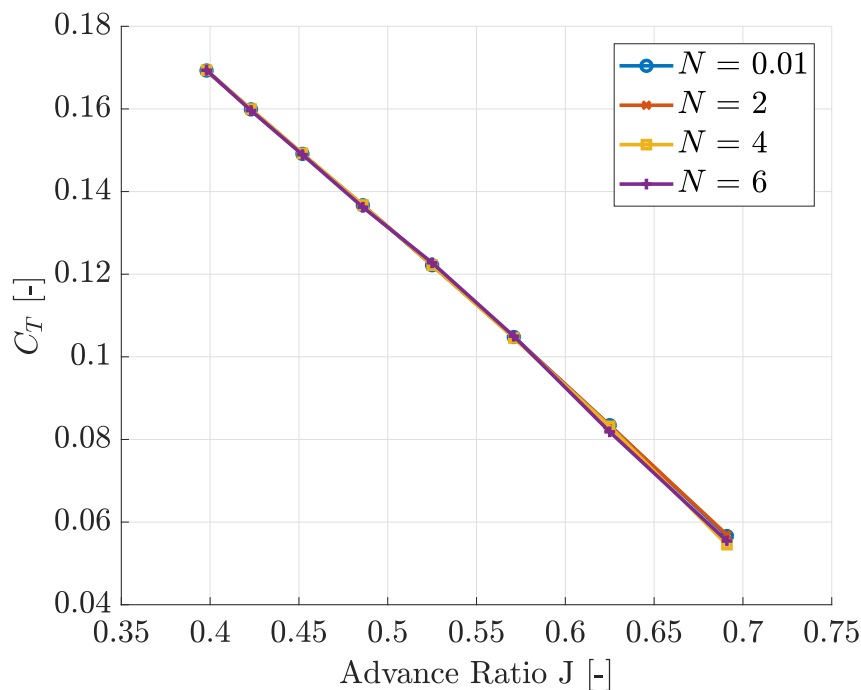


Figure A.1: Propeller distribution: local  $\alpha_r$  distribution on the rear propeller at various radial station  $\eta$  for  $n_f = n_r = 135$  and  $d_y = 1.25$

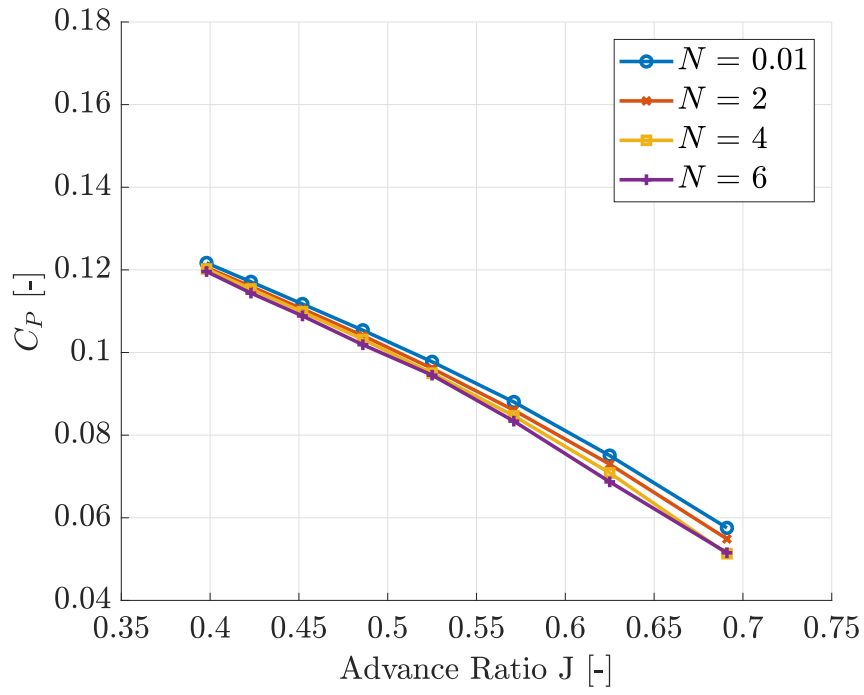


Figure A.2: Propeller distribution: local  $\alpha_r$  distribution on the rear propeller at various radial station  $\eta$  for  $n_f = n_r = 135$  and  $d_y = 1.25$

# B

## SENSOR CALIBRATION MATRIX

The measurements provided by the static balance sensor are converted into forces and moments using a calibration matrix  $AR$ , which is defined by:

$$AR = \begin{bmatrix} -9.6340 \cdot 10^{-2} & +1.7277 \cdot 10^{-1} & -2.1652 \cdot 10^{+0} & -4.4673 \cdot 10^{+1} & +1.7571 \cdot 10^{+0} & +4.5240 \cdot 10^{+1} \\ +1.1791 \cdot 10^{+0} & +5.1122 \cdot 10^{+1} & -2.3678 \cdot 10^{+0} & -2.5679 \cdot 10^{+1} & -5.9553 \cdot 10^{-1} & -2.6288 \cdot 10^{+1} \\ +5.9247 \cdot 10^{+1} & +8.6197 \cdot 10^{-1} & +6.0217 \cdot 10^{+1} & -9.1981 \cdot 10^{-1} & +5.9239 \cdot 10^{+1} & +4.6621 \cdot 10^{-1} \\ +1.0270 \cdot 10^{-2} & +4.5578 \cdot 10^{-1} & -9.7647 \cdot 10^{-1} & -2.0820 \cdot 10^{-1} & +9.5558 \cdot 10^{-1} & -2.3100 \cdot 10^{-1} \\ +1.0760 \cdot 10^{+0} & +1.8450 \cdot 10^{-2} & -5.4185 \cdot 10^{-1} & +4.0475 \cdot 10^{-1} & -5.6608 \cdot 10^{-1} & -4.0815 \cdot 10^{-1} \\ -4.6200 \cdot 10^{-3} & -6.6517 \cdot 10^{-1} & -3.7940 \cdot 10^{-2} & -6.6336 \cdot 10^{-1} & -4.5850 \cdot 10^{-2} & -6.7513 \cdot 10^{-1} \end{bmatrix}$$



# C

## ADDITIONAL NUMERICAL RESULTS

In this Appendix additional numerical results are presented. To understand better the effect of the lateral separation, in a time averaged approach, in the following Figures the lift coefficient distribution over the propeller disc is shown. The front propeller rotational speed is  $n_f = 135$  rps, and  $n_r = n_f$ . The whole range of lateral separation factors  $d_y$  is presented. In particular, from Figures C.1a to C.1d the distributions are relative to  $d_y = [0, 0.25, 0.375, 0.5]$ , while in Figures from C.2a to C.2h the range is  $d_y = [0.625, 0.75, 0.875, 1, 1.25, 1.5, 2, 3]$ . The axial separation is  $d_x = 5.5$ .

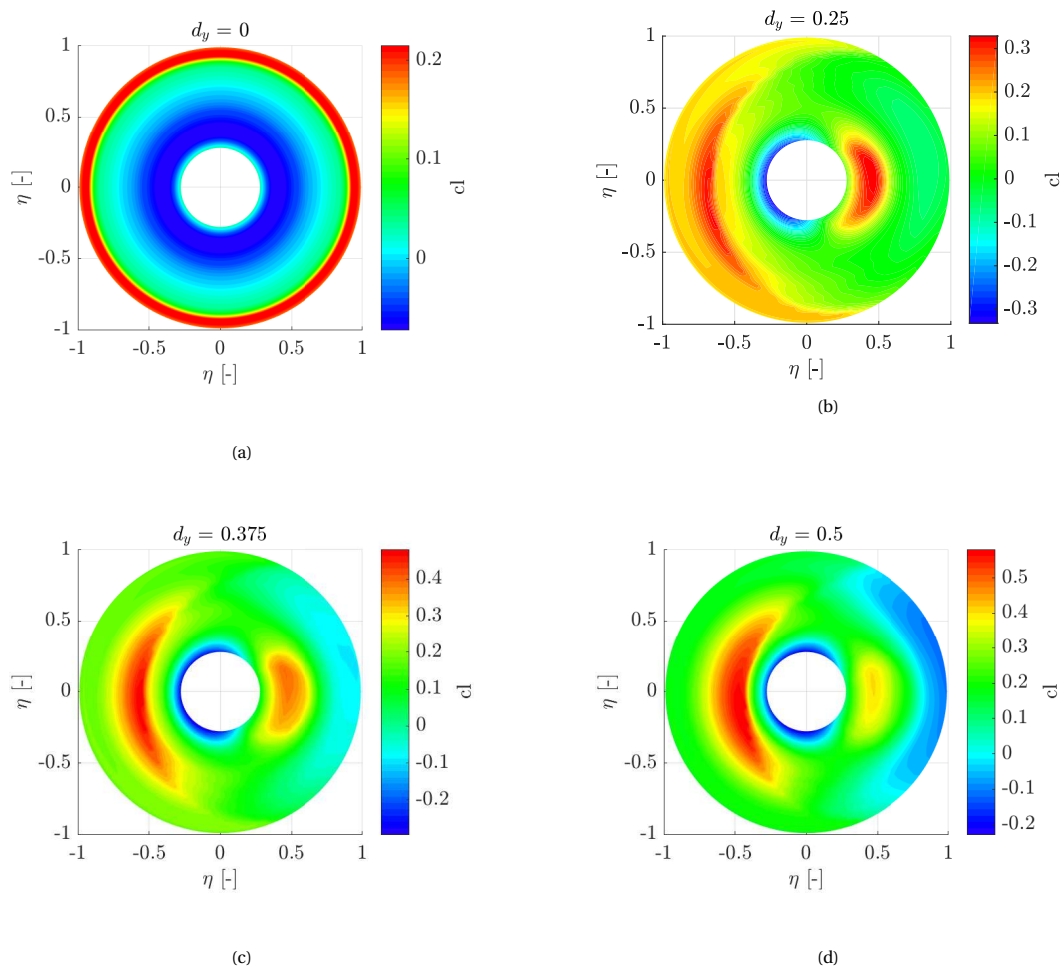


Figure C.1: Lift coefficient distribution over the propeller for  $d_y = [0, 0.25, 0.375, 0.5]$

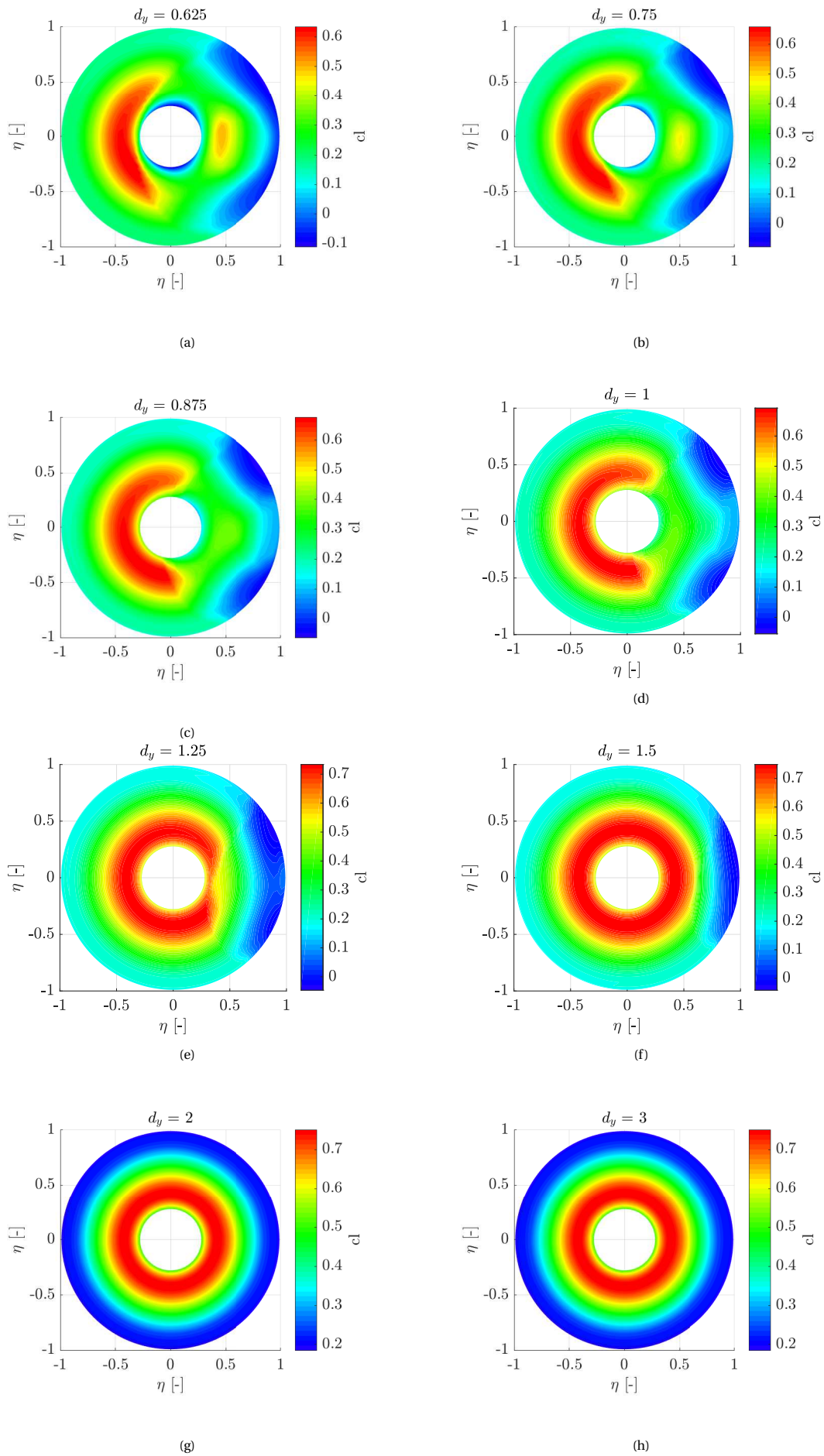


Figure C.2: Lift coefficient distribution over the propeller for  $d_y = [0.625, 0.75, 0.875, 1, 1.25, 1.5, 2, 3]$

# BIBLIOGRAPHY

- [1] Uber Elevate. Fast-forwarding to a future of on-demand urban air transportation. *Technical report, Uber Elevate Whitepaper*, 2016.
- [2] <https://vahana.aero/vahana-design-process-part-ii-preparing-for-lift-off-a75b7ef6d583>.
- [3] Demo J. Giulianetti Martin D. Maisel and Daniel C. Dugan. The History of the XV-15 Tilt Rotor Research Aircraft From Concept to Flight. 2000.
- [4] Kenneth I. Swartz. Charging Forward. New eVTOL concepts advance. *Vertiflite*, pages 24–29, August 2017.
- [5] Martin Hepperle. Electric Flight – Potential and Limitations. August 2017.
- [6] Joint Center for Energy Storage Research, <https://www.jcesr.org>.
- [7] <http://evtol.news/aircraft/bell-air-taxi>.
- [8] <https://vahana.aero/flight-test-update-50-flights-53af963e1750>.
- [9] 2019.
- [10] Jr. Richard E. Kuhn William C. Hayes and Irving R. Sherman. Effects of Propellers Position and Overlap on the Slipstream Deflection Characteristics of a Wing-Propellers Configuration Equipped with a Sliding and Fowler Flap. September 1958.
- [11] Kwanjung Yee Jaewon Lee, Sejong Oh and Deog-Kwan Kim. Numerical Investigation on Overlap Effects of Tandem Rotors in Forward Flight. *Journal of Aeronautical and Space Sciences, Vol. 10, No. 2*, pages 63–76, November 2009.
- [12] Arjun Srinivasan Ganeshram Nandakumar and Asokan Thondiyath. Theoretical and Experimental Investigation on the Effect of Overlap and Offset on the Design of a Novel Quadroto Configuration, VOOPS. 2017.
- [13] Manikandan Ramasamy. Measurements Comparing Hover Performance of Single, Coaxial, Tandem, and Tilt-Rotor Configurations. 2013.
- [14] Stephen D. Prior Mantas Brazinskas and James P. Scanlan. An Empirical Study of Overlapping Rotor Interference for a Small Unmanned Aircraft Propulsion System. 25 July 2016.
- [15] W.J.M Rankine. *On the Mechanical Principles of the Action of Propellers*. London, 1865.
- [16] H. Glauert. *Airfoil and Airscrew Theory*. 1943.
- [17] S. Drzewiecki. *Théorie Générale de l'Hélice Propulsive*. 1920.
- [18] L.L.M. Veldhuis. Propeller Wing Aerodynamic Interference. 2005.
- [19] L. Prandtl. *Tragflugel Theorie*. 1918.
- [20] A. Betz. *Introduction to the Theory of FlowMachines*. 1966.
- [21] Th. Theodorsen. *The Theory of Propellers - Part III, The Slipstream Contraction with Numerical Values for Two-Blade and Four-Blade Propellers*. 1944.
- [22] Ronan Boisard Biel Ortun and Ignacio Gonzalez-Martino. In-plane Airloads of a Propeller with Inflow Angle : Prediction vs. Experiment. *30th AIAA Applied Aerodynamics Conference*, 2012.
- [23] W. Z. Stepniewski. *Rotary-Wing Aerodynamics, Volume I - Basic Theories of Rotor Aerodynamics (With Application to Helicopters)*. 1979.

- [24] Kwanjung Yee Jaewon Lee and Sejong Oh. Aerodynamic Characteristic Analysis of Multi-Rotors Using a Modified Free-Wake Method. *Trans. Japan Soc. Aero. Space Sci. Vol. 52, No. 177*, pages 168—179, 2009.
- [25] J. Bosschers H.R. Snel, R. Houwink. Sectional Prediction of Lift Coefficients on Rotating Wind Turbine Blades in Stall. 1994.
- [26] R. P. J. O. M. van Rooij. Modification of the boundary layer calculation in RFOIL for improved airfoil stall prediction. 1996.
- [27] H. Himmelskamp. Profile Investigation on a Rotating Airscrew. 1945.
- [28] T.C.A. Stokkermans and L. L. M. Veldhuis. Propeller Performance at Large Incidence Angle for Compound Helicopters and eVTOL. (*unpublished*).
- [29] B. Chandrasekaran. Method for the Prediction of the Installation Aerodynamics of a Propfan at Subsonic Speeds. 1985.
- [30] A.S. Aljabri. The Prediction of Propeller-Wing Interaction Effects. *13th Congress of the International Council of the Aeronautical Science*, 1982.
- [31] W. R. Sears. Some Aspects of Non-Stationary Airfoil Theory and its Practical Application. *Journal of the Aeronautical Sciences*, 8(3), 1941.
- [32] W. R. Sears. Systematic Presentation of the Theory of Thin Airfoils in Non-Uniform Motion. *PhD thesis, California Institute of Technology*, 1938.
- [33] T. Sinnige. The Effects of Pylon Blowing on Pusher Propeller Performance and Noise Emissions. *Master of Science thesis, Delft University of Technology, Delft*, 2013.
- [34] Delft University of Technology. Open Jet Facility, 2008. <https://www.tudelft.nl/en/lr/organisation/departments-and-chairs/aerodynamics-and-wind-energy/wind-energy/facilities/open-jet-facility/>.
- [35] Y. Yang. Aerodynamic Interaction between Propeller and Vortex. 2017.
- [36] J. L. van Ingen. The eN Method for Transition Prediction. Historical of Work at TU Delft. 2008.